Thermoelectric Energy Harvesting in Harsh Environments and Laser Additive Manufacturing for Thermoelectric and Electromagnetic Materials

Kan Sun

Dissertation submitted to the faculty of the Virginia Polytechnic Institute and State University in partial fulfillment of the requirements for the degree of

Doctor of Philosophy

In

Mechanical Engineering

Scott T. Huxtable, PhD, Chair

Hang Yu, PhD

Danesh Tafti, PhD

Bart Raeymaekers, PhD

12/04/2024

Blacksburg, Virginia

Keywords: Thermoelectric, Energy Harvesting, Laser Additive Manufacturing.

Thermoelectric Energy Harvesting in Harsh Environments and Laser Additive Manufacturing for Thermoelectric and Electromagnetic Materials

Kan Sun

Abstract

This dissertation presents innovative research at the intersection of thermoelectric solutions, additive manufacturing, and nuclear safety technology, addressing critical challenges in sensor powering for extreme environments, energy harvesting, and materials fabrication. The research is divided into three key areas, each contributing to advancements in its respective domain.

First, a self-powered wireless through-wall data communication system was developed for monitoring nuclear facilities, specifically spent fuel storage dry casks. These facilities require continuous monitoring of internal conditions, including temperature, pressure, radiation, and humidity, under harsh environments characterized by high temperatures and intense radiation without any penetration through their walls. The constructed system integrated four modules: an energy harvester with power management circuits, an ultrasound wireless communication system using high-temperature piezoelectric transducers, electronic circuits for sensing and data transmission, and radiation shielding for electronics. Experimental validation demonstrated that the system harvests over 40 mW of power from thermal flow, withstands gamma radiation exceeding 100 Mrad, and survives temperatures up to 195°C. The system, designed to operate stably for fifty years, enables data transmission every ten minutes, ensuring reliable long-term monitoring for nuclear safety and security.

Second, the efficiency of thermoelectric generators (TEGs), unique solid-state devices for thermal-to-electrical energy conversion, was explored through a novel manufacturing approach using selective laser melting (SLM) and direct energy deposition (DED). Conventional TEG fabrication methods have limitations in achieving optimal efficiency due to design and material constraints. SLM-based additive manufacturing offers a scalable solution for creating geometry-flexible and functionally graded thermoelectric materials. This research developed a physical model to simulate the SLM and DED process for fabricating Mg_2Si thermoelectric materials with Si doping. The model incorporates conservation equations and accounts for fluid flow driven by buoyancy forces and surface tension, enabling detailed analysis of process parameters such as laser scanning speed and power input. The results provided insights into temperature distribution,

powder bed shrinkage, and molten pool dynamics, advancing the understanding and optimization of thermoelectric device fabrication using additive manufacturing. One step further, SLM and DED experiments were carried out to validate the simulation results and testify to the feasibility of applying laser powder bed fusion on semiconductor materials.

Third, the research investigates the application of laser additive manufacturing to improve performance and reduce the production costs of magnetic materials. Soft magnetic materials, critical for various industrial applications, are fabricated using DED. The research optimizes DED printing parameters and processes through quality control experiments inspired by the Taguchi method and analysis of variance models. The resulting silicon-iron samples exhibit minimal defects and cracks, demonstrating the feasibility of the approach. Detailed optical and scanning electron microscopy, coupled with magnetic characterization, reveal that the rapid cooling process inherent to laser-based AM enables unique microstructures that enhance magnetic properties.

Collectively, this work addresses pressing technological challenges in energy harvesting, materials fabrication, and extreme environment monitoring. The developed systems and methodologies have broad implications for nuclear safety, additive manufacturing, and the efficient utilization of advanced materials. By integrating interdisciplinary approaches and leveraging cutting-edge manufacturing technologies, this dissertation contributes to the advancement of sustainable and resilient solutions for modern engineering challenges.

Thermoelectric Energy Harvesting in Harsh Environments and Laser Additive Manufacturing for Thermoelectric and Electromagnetic Materials

Kan Sun

General Audience Abstract

This dissertation explores groundbreaking advancements in energy solutions, manufacturing techniques, and nuclear safety, presenting technologies that address challenges in powering sensors, creating efficient energy harvesters, and developing advanced materials. The research spans three main areas, each providing innovative contributions to these critical fields.

The first part focuses on a wireless system that powers itself and communicates data from inside sealed nuclear storage containers. These containers, used to store spent nuclear fuel, must be closely monitored for temperature, pressure, radiation, and humidity to ensure safety. However, traditional monitoring methods cannot penetrate the container walls and withstand the extreme conditions inside. This project developed a system combining four key components: a thermal energy harvester, an ultrasound-based communication method, durable electronic circuits, and radiation shielding. The system successfully harvests energy from the container's heat and uses it to power sensors and transmit data wirelessly every ten minutes. It is designed to operate reliably for fifty years, even under intense radiation and high temperatures, providing long-term solutions for nuclear safety monitoring.

The second area investigates thermoelectric generators (TEGs), devices that convert heat into electricity. While TEGs have significant potential, traditional manufacturing techniques limit their efficiency and adaptability. By using cutting-edge laser-based additive manufacturing methods—Selective Laser Melting (SLM) and Direct Energy Deposition (DED)—this research developed new ways to create flexible and efficient thermoelectric materials. Advanced simulations were performed to model the manufacturing process, analyzing how factors like laser speed and power affect the final material properties. These models provided valuable insights into optimizing the process, which were then validated through experimental testing. The findings open the door to scalable and efficient production of thermoelectric devices for various energy applications.

The third area addresses the fabrication of magnetic materials, essential for many industrial technologies. Traditional methods of creating magnetic materials can be expensive and prone to defects. This research applied laser-based additive manufacturing to produce soft magnetic materials, such as silicon iron, with fewer flaws and improved performance. By optimizing the printing parameters through experiments and statistical analysis, the team created materials with enhanced magnetic properties. Microscopic analysis revealed that the rapid cooling during manufacturing produced unique structures that contribute to the materials' superior qualities. These advancements have the potential to reduce costs and improve the efficiency of magnetic products in various industries.

In summary, this dissertation tackles some of the most pressing challenges in energy, manufacturing, and safety technology. By developing systems that can monitor nuclear storage for decades, improving methods to harvest energy from heat, and creating better magnetic materials, this work paves the way for safer and more efficient solutions to modern engineering problems. These innovations are not only critical for nuclear safety but also hold promise for broader applications in sustainable energy and advanced manufacturing, contributing to a safer and more efficient future for industries worldwide.

Acknowledgment

I sincerely thank everyone who has supported and collaborated with me throughout this journey. Completing this research and dissertation was far from a solo effort, and I am deeply grateful for all the guidance, encouragement, and assistance I have received.

First and foremost, I express my heartfelt gratitude to my advisor, Dr. Scott Huxtable, for his unwavering support, patience, understanding, and encouragement over the past two years. His timely advice and kind help guided me during moments when I felt on the brink of retreat. His words and attitude inspired me to persevere, ultimately enabling me to complete this dissertation. The confidence and encouragement he has instilled in me will serve as my foundation in both my future work and personal life.

I extend my deepest thanks to my former advisor, Dr. Lei Zuo. As my first mentor in research and academia, his enthusiasm and determination have always been a source of inspiration. His vision and philosophy regarding future planning have not only shaped my career but also provided lessons I hope to pass on to my future students and descendants.

I owe profound gratitude to my family for their unwavering support and unconditional love during these years of my overseas journey. To my parents, Professor Sun Suigen and Mrs. Wang Meihong, I am forever thankful for their unparalleled care and trust, giving me the freedom to make decisions and backing me unconditionally. To my grandparents, I offer my heartfelt thanks and deepest apologies—I could not be with them in their final moments, a regret I will always carry. To my uncles, aunts, and cousins, the joyful memories they have shared with me have been a source of strength and resilience.

I am sincerely grateful to my advisory board members, Dr. Hang Yu, Dr. Danesh Tafti, and Dr. Bart Raeymaekers, for their invaluable feedback and guidance, which were crucial to the completion of this dissertation. I also deeply appreciate the kind support of Dr. Huan Qi, Dr. Zhiwei Wu, and Dr. Chuanbing Rong, who assisted me with my experiments.

Special thanks to Dr. Yongjia Wu, who has been both a mentor and a close friend during my early years at Virginia Tech. His knowledge and perspective on life and career continue to inspire me. Without his guidance and collaboration, I might not have been able to begin this dissertation, let alone finish it.

I also wish to thank Dr. Feng Qian, Fukang Li, Dr. Hyunjun Jung, Dr. Shifeng Yu, Greg Hahn, Alexander Koelsch, Justin He, Donald Leber, and Shuvodip Bhattacharya for their invaluable assistance with my research. To my colleagues and friends at the Center for Energy Harvesting Materials and Systems, including Dr. Shifeng Yu, Hanchen Zhou, Dr. Weiche Tai, Dr. Mingyi Liu, Yingying Fan, Dr. Yu Pan, Dr. Xiaofan Li, Qiuchi Xiong, Dr. Sijing Guo, Dr. Hongjip Kim, Rui Lin, Boxi Jiang, Shuo Chen, Dr. Jia Mi, Dr. Bonan Qin, Yuzhe Chen, Lisheng Yang, Jianuo

Huang, Dr. Qiaofeng Li, Xian Wu, Haozheng Wang, and Jiajun Zhang, I sincerely appreciate the camaraderie and support. To my roommates and friends in Blacksburg and Christiansburg, including Dr. Rongxuan Wang, Dr. Qianqian Zhang, Yihuan Fang, Dr. Jue Wang, Yiran Xu, Jiarong Cui, Xiaochuan Fang, Fulan Li, Zihao Cai, Dr. Huaiyang Zhong, Qiyuan Shi, Jiajun She, and Zhiyuan Zhang, your friendship has been an unforgettable treasure. To all others whose names I may have inadvertently missed, please know that your presence in my life has been invaluable.

I would like to express my appreciation to the staff members of the Mechanical Engineering Department and the Graduate School. Special thanks to Ms. Lauren Mills and Ms. Cathy Hills for their countless acts of assistance. Their names appear most frequently in my “sent” folder for good reason.

Finally, I gratefully acknowledge the financial support from the U.S. Department of Energy NEET Program via Grant #16-10884 and the U.S. National Science Foundation via Grants #1508862, #1915946, and #1738689.

Nomenclatures

u_b	Laser scanning speed, m/s
x, y, z	Coordinates, m
w_s	Velocity caused by powder shrinkage, m/s
p	Pressure, Pa
μ^+	Effective viscosity, $kg/(m \cdot s)$
T	Temperature, K
t	Time, s
g	Gravity acceleration, m/s^2
k^+	Effective thermal conductivity, W/mK
S_h	Energy source term, W/m^3
S_C	Nano-particle concentration source term, m^{-3}
D^+	Effective diffusive coefficient, $kg/(m \cdot s)$
C^+	Effective concentration ratio
ε	Porosity
s	Shrinkage, m
T_M	Melting temperature, K
ΔT	Temperature difference, K
H, h	Enthalpy, J/kg
f_s, f_l	Solid and liquid mass faction
κ	thermal conductivity, $W/(m \cdot K)$
φ	Concentration radio
c_p	Specific heat, $J/(K \cdot kg)$
ρ	Density, kg/m^3
μ_l	Liquid viscosity, $kg/(m \cdot s)$
μ_s	Solid viscosity, $kg/(m \cdot s)$

D	Specific diffusion coefficient, $kg/(m \cdot s)$
L	Latent heat, J/kg
K_0	Permeability coefficient
β_T	Thermal expansion coefficient, K^{-1}
β_s	Solute expansion coefficient, K^{-1}
T_e	Eutectic temperature, K
T_M	Melting point temperature, K
k	Equilibrium partition ratio
T_a	Ambient temperature, K
θ	Energy absorption coefficient
ε_b	Emissivity
h_c	Convective heat transfer coefficient, $W/(m^2K)$
R	Laser diameter, m
σ_b	Boltzmann constant
$\partial\sigma/\partial T$	Change rate of surface tension, $N/(m \cdot K)$
q_0	Laser intensity, W/m^2
σ_s	Surface tension, N/m
ψ	Limiter function
$a_E, a_W, a_N, a_S, a_F, a_B, a_P$	TVD coefficients
$D_e, D_w, D_n, D_s, D_f, D_b$	Diffusion conductance, $kg/(m^2 \cdot s)$
$F_e, F_w, F_n, F_s, F_f, F_b$	Convective mass flux, $kg/(m^2 \cdot s)$
ϕ	Variable to be solved
S_u^{DC}	The deferred correction source term
r	Ratio of gradients

Publications

Peer-reviewed journal papers

1. Wu, Yongjia, **Kan Sun**, Shifeng Yu, and Lei Zuo. "Modeling the selective laser melting-based additive manufacturing of thermoelectric powders." Additive Manufacturing 37 (2021): 101666.

2. **Sun, Kan**, Yongjia Wu, Feng Qian, Hyunjun Jung, Suresh Kaluvan, He Huijin, Cheng Zhang et al. "Self-powered Through-wall communication for dry cask storage monitoring." Annals of Nuclear Energy 177 (2022): 109306.

3. **Sun, Kan**, Fukang Li, Chuanbing Rong, and Lei Zuo. "Direct energy deposition applied to soft magnetic material additive manufacturing." Journal of Manufacturing Processes 84 (2022): 162-173.

Peer-reviewed conference papers

1. Wu, Yongjia, Lei Zuo, and **Kan Sun**. "Modeling the Selective Laser Melting of Multi-Component Thermoelectric Powders." In International Design Engineering Technical Conferences and Computers and Information in Engineering Conference, vol. 51722, p. V01AT02A049. American Society of Mechanical Engineers, 2018.

2. **Sun, Kan**, Yongjia Wu, Huan Qi, Zhiwei Wu, and Lei Zuo. "Direct Energy Deposition 3D Printing of Thermoelectric Materials: Simulation and Experiments." In International Design Engineering Technical Conferences and Computers and Information in Engineering Conference, vol. 59223, p. V004T05A012. American Society of Mechanical Engineers, 2019.

Newsletter

1. Lei Zuo, **Kan Sun**, Yongjia Wu, Haifeng Zhang, Nance Ericson, Kyle Reed, Roger Kisner, "Self-powered Wireless Through-wall Data Communication for Nuclear Environments." Advanced sensor and instrument (NEET), 2019.

Table of Contents

Table of Figures

Table of Tables

1 Chapter 1. Introduction and Background

1.1 Physics in Thermoelectrics

Thermoelectric (TE) phenomena describe the interaction between thermal and electrical energy in materials, providing a framework for understanding how heat and electricity can directly influence one another. These principles are rooted in three fundamental effects: the Seebeck effect, the Peltier effect, and the Thomson effect. Together, these effects form the core of thermoelectrics and highlight the intrinsic relationship between thermodynamics and electromagnetism.

The Seebeck Effect

The Seebeck effect, discovered by Thomas Johann Seebeck in 1821 [1], occurs when a temperature gradient is established across two dissimilar conductors or semiconductors joined at two junctions. This temperature difference induces charge carriers—electrons in metals or electrons and holes in semiconductors—to diffuse from the hotter region to the colder one. This movement generates an electromotive force (EMF), or voltage, across the material.

The generated voltage, known as the Seebeck voltage VVV, is proportional to the temperature difference ΔT and is described by the equation:

$$V = \alpha \Delta T \tag{1.1}$$

Here, α is the Seebeck coefficient, which depends on the material's electronic structure and properties. Materials with high Seebeck coefficients are desirable for thermoelectric applications, as they generate larger voltages for a given temperature gradient.

The Seebeck effect is a direct result of the diffusion of charge carriers under a thermal gradient, explained by Fermi-Dirac statistics and thermodynamics. [2] The redistribution of carriers at different energy levels causes the observed voltage, linking the phenomenon to the material's electronic band structure and density of states.

The Peltier Effect

The Peltier effect, discovered by Jean Charles Athanase Peltier in 1834 [3], is the inverse of the Seebeck effect. It describes the absorption or release of heat at the junction of two different materials when an electric current flows through the junction. The direction of the current determines whether heat is absorbed or released, making the effect symmetric and reversible.

The rate of heat transfer Q at the junction is proportional to the current I and is expressed as:

$$Q = \Pi I$$

(1.2)

Here, Π is the Peltier coefficient, which is related to the material's Seebeck coefficient by the Kelvin relation:

$$\Pi = \alpha T$$

(1.3)

where T is the absolute temperature. This relationship connects the Peltier effect to the Seebeck effect through thermodynamic principles.

The Peltier effect arises due to the energy exchange associated with charge carriers crossing the junction of two materials. The carriers adjust their energy levels to align with the electronic properties of each material, resulting in heat absorption or release depending on the current direction. [4]

The Thomson Effect

The Thomson effect, discovered by William Thomson (later Lord Kelvin) in 1851 [5], describes the reversible heating or cooling that occurs within a single homogeneous conductor when an electric current flows in the presence of a temperature gradient. Unlike the Seebeck and Peltier effects, which occur at material junctions, the Thomson effect operates within the bulk of a material.

The heat generated or absorbed per unit length of the conductor q is proportional to the product of the electric current III, the temperature gradient dT/dx, and the Thomson coefficient μ:

$$q = \mu I \frac{dT}{dx}$$

(1.4)

The Thomson coefficient μ is a material-specific property and depends on the temperature. The Thomson effect complements the Seebeck and Peltier effects by explaining the internal heat flow in a conductor.

Interrelation of Thermoelectric Effects

The Seebeck, Peltier, and Thomson effects are interconnected through the thermodynamic framework established by Thomson. These relationships ensure consistency between the effects and provide a unified description of thermoelectric phenomena.

One fundamental relationship is the Kelvin relation (1.3), which links the Seebeck and Peltier coefficients. Another important connection is derived from the temperature dependence of the Seebeck coefficient, which relates to the Thomson coefficient:

$$\mu = T\frac{d\alpha}{dT}$$

(1.5)

These interrelations demonstrate that the three thermoelectric effects are not independent but arise from the same underlying principles of thermodynamics and charge carrier behavior.

1.2 Scientific Timeline of Thermoelectrics and Its Applications

The work into thermoelectrics has been a long journey since the 19th century of scientific inquiry and technological development, rooted in the foundational discoveries of the Seebeck, Peltier, and Thomson effects. These effects provided the theoretical framework for thermoelectric phenomena, but their practical applications emerged gradually as advancements in materials science and engineering allowed for their optimization and scalability. This section outlines the scientific milestones in thermoelectrics and explores their evolution into modern applications, emphasizing the interplay between fundamental research and technological progress.

Early Discoveries and Theoretical Developments

The scientific journey of thermoelectrics began with Thomas Johann Seebeck's discovery in 1821 [1] that a temperature difference across two dissimilar materials produces an electromotive force. This observation laid the groundwork for understanding thermoelectric power generation. Seebeck initially interpreted this effect in terms of magnetism, calling it "thermomagnetism," as he noted the deflection of a magnetic needle near the circuit. Later research clarified that the effect arises from the diffusion of charge carriers due to thermal gradients.

Jean Charles Athanase Peltier expanded this understanding in 1834 [3] by observing that an electric current passing through the junction of two dissimilar materials could either absorb or release heat, depending on the current's direction.his discovery of the Peltier effect introduced the possibility of using thermoelectric phenomena for active heating and cooling, forming the basis for thermoelectric refrigeration.

In 1851, William Thomson (Lord Kelvin) unified these discoveries through thermodynamic analysis, predicting and later verifying the Thomson effect, which describes reversible heating or cooling within a single material under simultaneous current flow and temperature gradients. [5] Kelvin's theoretical framework established the relationships between the Seebeck, Peltier, and Thomson effects, providing a comprehensive thermodynamic understanding of thermoelectric phenomena.

Transition to Practical Applications

Despite the early theoretical advances, practical applications of thermoelectric effects were limited for much of the 19th and early 20th centuries due to the lack of suitable materials. The discovery of semiconductors in the mid-20th century marked a turning point, as these materials possess the high Seebeck coefficients, electrical conductivity, and low thermal conductivity required for efficient thermoelectric performance.

In 1954, Abram Ioffe's pioneering work in the Soviet Union identified bismuth telluride (Bi_2Te_3) and its alloys as highly effective thermoelectric materials. [6] This breakthrough enabled the development of the first practical thermoelectric devices, including power generators and solid-state coolers. Ioffe's work also introduced the concept of the dimensionless thermoelectric figure of merit (*ZT*), defined as:

$$ZT = \frac{\alpha^2 \sigma T}{\kappa} \tag{1.6}$$

where α is the Seebeck coefficient, σ is electrical conductivity, T is absolute temperature, and κ is thermal conductivity. A high ZT value is critical for efficient thermoelectric devices, and materials research has since focused on maximizing this parameter.

Evolution of Applications

Power Generation

Thermoelectric power generation has its roots in space exploration. In the 1960s, NASA adopted thermoelectric generators (TEGs) for space missions, leveraging their reliability and ability to convert heat from radioactive decay into electricity. Radioisotope thermoelectric generators (RTGs) became integral to long-duration missions, such as Voyager, Cassini, and the Mars rovers.

On Earth, thermoelectric generators have been used for remote power supply applications, such as powering sensors and communication equipment in isolated or harsh environments. More recently, efforts to harvest waste heat from industrial processes and automotive engines have driven interest in thermoelectric power generation as a means of improving energy efficiency and reducing greenhouse gas emissions.

Thermoelectric Cooling and Heating

Thermoelectric coolers (TECs) emerged as a practical application of the Peltier effect in the mid-20th century. Their compact size, lack of moving parts, and precise temperature control made TECs ideal for applications ranging from electronics cooling to portable refrigeration. Early adoption occurred in niche markets, but modern TECs are increasingly used in medical devices, such as portable insulin coolers, and in consumer electronics.

Temperature Sensing

Thermocouples, based on the Seebeck effect, are among the oldest and most widespread thermoelectric applications. These devices provide accurate and reliable temperature measurements across a wide range of conditions, from industrial furnaces to cryogenic environments. Advances in thermocouple materials and designs have further expanded their utility in scientific research and engineering.

Modern Advances and Challenges

The late 20th and early 21st centuries have seen rapid progress in thermoelectric materials and device engineering. The advent of nanotechnology has enabled the fabrication of nanostructured thermoelectric materials, which can significantly reduce thermal conductivity without compromising electrical conductivity. Quantum wells, superlattices, and other low-dimensional structures have achieved record-high ZT values, offering new opportunities for thermoelectric applications. [7]

Despite these advances, thermoelectrics face challenges in achieving widespread adoption. High material costs and relatively low efficiency compared to conventional technologies have limited their use in large-scale power generation. Research efforts are focused on discovering abundant, low-cost materials with enhanced thermoelectric properties and on developing scalable manufacturing techniques, such as additive manufacturing, to reduce production costs.

The scientific history of thermoelectrics demonstrates the transformative power of fundamental discoveries when combined with advancements in materials and engineering. From Seebeck's initial observations to the sophisticated thermoelectric devices of today, the field has continually evolved to address the energy and cooling needs of diverse applications. The interplay between theory and application remains a driving force in thermoelectric research, promising continued innovation and new frontiers in energy technology.

1.3 Thermoelectric Fabrication Methods

The fabrication of thermoelectric materials has undergone significant evolution from traditional techniques that laid the foundation of the field to advanced methods that leverage modern manufacturing technologies. These methods are critical in controlling the material properties essential for achieving high thermoelectric performance, such as optimizing the Seebeck coefficient, electrical conductivity, and thermal conductivity. This section discusses both traditional and emerging fabrication methods, emphasizing their scientific principles and impact on the development of thermoelectric materials.

Solid-State Synthesis

Solid-state synthesis is one of the oldest and most widely used methods for fabricating thermoelectric materials. In this approach, precursor powders of individual elements or compounds are thoroughly mixed and subjected to high-temperature heating to promote diffusion and solid-state reactions. This method has been extensively applied to the fabrication of thermoelectric compounds such as bismuth telluride (Bi_2Te_3) and lead telluride (PbTe). [2, 4] While solid-state synthesis is cost-effective and scalable for bulk production, it often produces materials with limited control over microstructure and grain size. These limitations can negatively affect thermoelectric performance by increasing thermal conductivity and reducing carrier mobility.

Mechanical Alloying

Mechanical alloying, particularly high-energy ball milling, emerged as a powerful method for synthesizing thermoelectric materials with fine-grained or nanostructured features. This technique uses mechanical forces to mix and refine powders, enabling the formation of solid solutions and nanocomposites at relatively low temperatures. [8] For example, mechanical alloying has been used to fabricate skutterudites and clathrates, which are promising thermoelectric materials due to their inherently low thermal conductivity. Although mechanical alloying allows for precise control over material composition and morphology, it requires careful optimization of milling parameters to avoid contamination and ensure reproducibility.

Hot Pressing and Spark Plasma Sintering (SPS)

Consolidation techniques such as hot pressing and SPS are commonly used to densify thermoelectric powders into bulk materials. Hot pressing involves the simultaneous application of heat and pressure to compress powders, while SPS employs pulsed electric currents to achieve rapid heating and sintering. [9] These methods have been instrumental in producing dense, high-performance thermoelectric materials with well-controlled grain boundaries. However, the equipment cost and energy requirements, particularly for SPS, remain a significant consideration for large-scale production.

Zone Melting

Zone melting is a directional solidification technique used to produce single-crystal thermoelectric materials. In this process, a localized heat source melts a narrow region of the material, which recrystallizes as the heat source moves through the material. [10] This method is especially effective for materials like Bi_2Te_3, where minimizing grain boundaries is essential to reducing scattering and improving carrier mobility. While zone melting produces high-purity, defect-free single crystals, its scalability is limited due to the time-intensive nature of the process.

Thin-Film Deposition

Thin-film deposition techniques such as sputtering, evaporation, and chemical vapor deposition (CVD) are widely used for fabricating thermoelectric materials in micro- and nanoscale applications. These methods enable precise control over film thickness, composition, and crystallinity, making them ideal for creating thermoelectric layers in microscale devices. [11] However, thin-film deposition methods are expensive and challenging to scale for bulk material production.

Nanostructuring

Nanostructuring is not a specific fabrication method in itself but rather a concept or outcome involving the design and creation of materials with nanoscale features (typically below 100 nm). It has revolutionized thermoelectric materials by enhancing their performance through increased phonon scattering and reduced thermal conductivity. Techniques such as bottom-up chemical synthesis and top-down mechanical milling are used to create nanostructured thermoelectric materials. [12] These methods allow for precise control over grain size and composition, resulting in materials with significantly improved thermoelectric figures of merit (ZT). However, the complexity and cost of nanostructuring processes remain barriers to widespread adoption.

Melt Spinning

Melt spinning is a rapid solidification process where molten thermoelectric materials are cooled at extremely high rates to form thin ribbons or flakes with fine-grained microstructures. These ribbons can be further processed into bulk materials with enhanced thermoelectric properties, as demonstrated for BiSbTe alloys. [13] Melt spinning offers a fast and efficient way to produce nanostructured thermoelectric materials, though its applicability is limited to materials with appropriate melting and solidification characteristics.

Electrochemical Deposition

Electrochemical deposition involves depositing thermoelectric materials from an electrolyte solution onto a substrate under an applied electric field. This method has been used to produce thin films of bismuth telluride alloys [14] and Poly(nickel-ethylenetetrathiolate) [15], an organic thermoelectric material. Electrochemical deposition is simple, low-cost, and scalable for thin films, but it is restricted to specific material systems and substrates.

Solution-Based Synthesis

Solution-based methods, including sol-gel and hydrothermal synthesis, are employed to create nanostructured thermoelectric materials with controlled morphology and composition. These techniques have been particularly effective for fabricating oxide-based thermoelectric materials, such as BiSbTe and PbTe. [16] While solution-based synthesis is versatile and cost-effective, post-synthesis processing is often required to achieve the desired material density and mechanical properties.

High-Pressure Synthesis

High-pressure synthesis is used to stabilize thermoelectric materials with complex crystal structures, such as skutterudites and clathrates, that may be unstable under standard conditions. [17] This method enables the discovery and production of novel materials with unique thermoelectric properties, although it requires specialized equipment and incurs high costs.

Additive Manufacturing (3D Printing)

Additive manufacturing, or 3D printing, is a novel approach that has recently gained traction in thermoelectric material fabrication. Techniques such as selective laser melting (SLM) and direct energy deposition (DED) enable the layer-by-layer construction of thermoelectric devices with complex geometries and functionally graded structures. For instance, Bi_2Te_3 has been successfully fabricated using SLM, demonstrating the potential for producing geometry-flexible thermoelectric materials. [18] Additive manufacturing also allows for tailoring material properties within a single device, but it requires precise control of process parameters to avoid defects such as cracks, porosity, and segregation. Despite these challenges, the customization capabilities of additive manufacturing make it a promising tool for the next generation of thermoelectric devices.

1.4 Phonon Heat Transfer, Nanostructure, and Amorphous Materials

Achieving high thermoelectric efficiency requires not only optimizing the electrical properties but also minimizing thermal conductivity, which predominantly arises from phonon heat transfer. Advances in material engineering, particularly in nanostructured and amorphous systems, have provided unprecedented control over these properties, enabling significant enhancements in thermoelectric performance. This section introduces the critical concepts of phonon heat transfer, the role of nanostructures, and the unique contributions of amorphous materials to thermoelectrics.

Phonon Heat Transfer in Thermoelectric Materials [19]

Thermal conductivity (κ) in thermoelectric materials has two primary contributions: electronic thermal conductivity (κ_e) and lattice thermal conductivity (κ_l). While κ_e is tied to the flow of charge carriers and thus interlinked with electrical conductivity via the Wiedemann-Franz law [20], κ_l originates from the transport of vibrational energy by phonons. [21] Phonons, the quantized modes of lattice vibrations, are the primary carriers of heat in non-metallic solids.

In thermoelectric materials, suppressing κ_l is crucial for improving the figure of merit (ZT). The thermal conductivity of a material is determined by phonon scattering processes, which include:

> *Phonon-phonon scattering*: Dominated by the anharmonicity of lattice vibrations, this intrinsic mechanism limits heat transport in high-temperature regimes.
>
> *Phonon-electron scattering*: Occurs in conductive materials where interactions between phonons and charge carriers impede phonon transport.
>
> *Phonon-boundary scattering*: Prominent in materials with nanoscale features, where the boundaries serve as barriers to phonon propagation.
>
> *Phonon-impurity scattering*: Caused by mass and strain variations in the lattice, particularly in alloyed and doped systems.

The total lattice thermal conductivity can be expressed through the Boltzmann transport equation. [22] (BTE):

$$\kappa_l = \frac{1}{3} C_v v_g^2 \tau \tag{1.7}$$

where C_v is the specific heat, v_g is the group velocity of phonons, and τ is the phonon relaxation time. By reducing v_g or τ through nanostructuring or introducing impurities, the lattice thermal conductivity can be substantially decreased without severely impacting electronic properties.

Nanostructures in Thermoelectric Materials

Nanostructuring has emerged as one of the most effective strategies to enhance thermoelectric performance by decoupling electronic and thermal transport properties. At the nanoscale, quantum confinement effects and increased phonon scattering can significantly alter the transport behavior of both electrons and phonons. [12]

Quantum Confinement and Density of States

Nanostructures, such as quantum wells, quantum dots, and nanowires, exhibit quantum confinement, where the electronic density of states (DOS) becomes discrete. This modification in the DOS enhances the Seebeck coefficient (α) by increasing the thermopower associated with sharp changes in DOS near the Fermi level. Hicks and Dresselhaus [7] demonstrated that low-dimensional systems, such as two-dimensional (2D) quantum wells and one-dimensional (1D) nanowires, exhibit higher ZT values compared to their bulk counterparts.

Phonon Boundary Scattering

Nanostructured materials, with features smaller than the mean free path of phonons, increase phonon-boundary scattering, thereby reducing κ_l. Structures such as nanopores, grain boundaries, and nano-inclusions act as scattering centers, impeding heat transfer while preserving or enhancing electrical conductivity. For example, embedded nano-inclusions in bulk Bi_2Te_3 have been shown to suppress κ_l without significantly affecting carrier mobility. [12]

Nanocomposites and Interfaces

Nanocomposite materials leverage interfaces to scatter phonons effectively. [23] Interfaces between different phases introduce mismatched acoustic impedances, which reflect and scatter phonons, reducing κ_l. Additionally, nanocomposites can exhibit energy filtering effects, where low-energy charge carriers are selectively scattered, improving the Seebeck coefficient and maintaining electrical conductivity.

Despite these advantages, challenges in fabricating and characterizing nanostructured thermoelectric materials remain significant. Achieving uniformity in size, shape, and distribution of nanostructures is critical for reproducibility and scalability.

Amorphous Materials in Thermoelectrics

Amorphous materials, characterized by their disordered atomic structure, present a unique approach to thermoelectric materials design. Unlike crystalline materials, amorphous systems lack long-range periodicity, which fundamentally alters their electronic and phononic transport properties. [24]

Reduction in Lattice Thermal Conductivity

The disordered structure of amorphous materials inherently disrupts phonon propagation, leading to extremely low lattice thermal conductivity. In these systems, phonon transport transitions from a wave-like to a diffusive regime. [25] This intrinsic suppression of κ_l makes amorphous materials particularly attractive for thermoelectric applications.

Electronic Transport in Amorphous Systems

Electronic transport in amorphous materials is less efficient than in crystalline counterparts due to the lack of a well-defined band structure. However, with careful doping and band engineering, amorphous systems can achieve sufficient electrical conductivity and Seebeck coefficients. For example, amorphous Boron composites have shown promise as thermoelectric materials for thermoelectric cooling applications. [26]

Hybrid and Composite Approaches

To overcome the limitations of low electrical conductivity, amorphous materials are often used in hybrid or composite systems. These combinations can leverage the low κ_l of the amorphous phase and the high α and σ of the crystalline or nanostructured phases. For instance, composites of amorphous Boron composites with crystalline Bi_xTe_y thermoelectric inclusions have demonstrated reduced thermal conductivity while maintaining decent power factors. [26]

Synergistic Design for Thermoelectric Optimization

The combination of nanoscale engineering and amorphous systems represents a powerful strategy for optimizing thermoelectric materials. Nanostructures enable tailored scattering of phonons and enhancement of electronic transport, while amorphous phases provide an even lower baseline for minimal lattice thermal conductivity. Together, these approaches offer a pathway to decouple electrical and thermal transport properties, breaking conventional trade-offs and achieving higher ZT.

The challenges in realizing these advanced systems lie in the precise control of material properties during synthesis and the integration of experimental findings with predictive modeling. Nevertheless, the ongoing development of sophisticated fabrication techniques, as discussed earlier, and computational tools for simulating phonon and electron transport can accelerate progress in this field.

1.5 Thermoelectric Characterization

The optimization of ZT value necessitates a precise understanding of the material's electrical and thermal transport properties, which are deeply influenced by its microstructure. Consequently, comprehensive characterization methods are crucial for the development of high-performance thermoelectric materials.

Thermoelectric characterization encompasses two primary domains: the analysis of the material's microstructure and the evaluation of transport properties, including electrical conductivity, thermal conductivity, and the Seebeck coefficient.

Microstructural Characterization

The microstructure of thermoelectric materials strongly influences their macroscopic properties. Following methods offer insights into crystalline structure, grain size, compositional uniformity, and nanoscale features, which are critical for optimizing thermoelectric performance.

X-ray Diffraction (XRD):

XRD is a widely used tool for determining crystal structure and phase composition. By analyzing the diffraction patterns of X-rays interacting with the material, researchers can derive information about lattice parameters, grain orientation, and crystallinity. The fundamental relationship governing XRD is Bragg's Law:

$$2dsin\theta = n\lambda \tag{1.8}$$

where d is the lattice spacing, θ is the diffraction angle, n is an integer, and λ is the X-ray wavelength. This technique is invaluable for identifying phase transitions and understanding the structural integrity of thermoelectric materials.

Figure 1.1. Panalytic X'pert Pro Triple Axis X-ray Diffractometer located at Advanced Devices & Sustainable Energy Laboratory (ADSEL) at Virginia Tech.

Scanning Electron Microscopy (SEM):

SEM provides high-resolution images of the surface morphology, enabling the examination of grain boundaries, voids, and defects. By scanning a focused electron beam across the material's surface, SEM generates signals that reveal surface topography and compositional contrasts.

Figure 1.2. ThermoScientific Helios 5 UC located at Virginia Tech Nanoscale Characterization and Fabrication Laboratory (VT-NCFL).

Energy-Dispersive X-ray Spectroscopy (EDS):

EDS complements SEM by providing elemental composition analysis. It detects the characteristic X-rays emitted when the material is bombarded with high-energy electrons, allowing the identification of chemical elements and their distribution within the sample.

Transmission Electron Microscopy (TEM):

TEM offers atomic-scale resolution by transmitting electrons through an ultra-thin sample. This technique is crucial for observing nanoscale features, such as dislocations, precipitates, and atomic arrangements. TEM's ability to resolve individual columns of atoms makes it indispensable for studying thermoelectric nanomaterials.

Figure 1.3. JEOL JEM 2100 TEM located at VT-NCFL, equipped with TEM and EDS.

Thermal Conductivity Characterization

Thermal conductivity (κ) is a key parameter in thermoelectric performance, reflecting the material's ability to conduct heat. It can be measured using bulk and thin-film techniques.

Laser Flash Method for Bulk Materials:

The laser flash method is a standard approach for measuring the thermal conductivity of bulk thermoelectric materials. It determines thermal diffusivity (α) by analyzing the time-dependent temperature response of the sample's backside after its front side is heated with a laser pulse. The thermal diffusivity is calculated as:

$$\alpha = \frac{1.37L^2}{\pi^2 t_{\frac{1}{2}}} \tag{1.9}$$

where L is the sample thickness and $t_{1/2}$ is the time for the backside temperature to reach half of its maximum value. The thermal conductivity is then determined using:

$$\kappa = \alpha \cdot C_p \cdot \rho \tag{1.10}$$

where C_p is the specific heat capacity, and ρ is the material density. Specific heat is measured by a differential scanning calorimeter using a reference material of known properties, sapphire (Al2O3) in this case, and density is determined from the sample's dimensions and mass.

Figure 1.4. TA-Instrument Differential Scanning Calorimeter at Thermal Analysis Lab at Virginia Tech.

3ω-Method for Thin Films:

For thin films, the 3ω-method is a preferred technique. [27] It involves applying an AC current at frequency ω to a microheater deposited on the thin film. The periodic temperature oscillation (ΔT) induced by heating occurs at 2ω and modulates the heater resistance, generating a voltage signal at 3ω. Thermal conductivity is extracted by comparing temperature oscillation amplitude with a theoretical thermal model. This technique is particularly effective for minimizing radiation effects and is suitable for nanoscale materials.

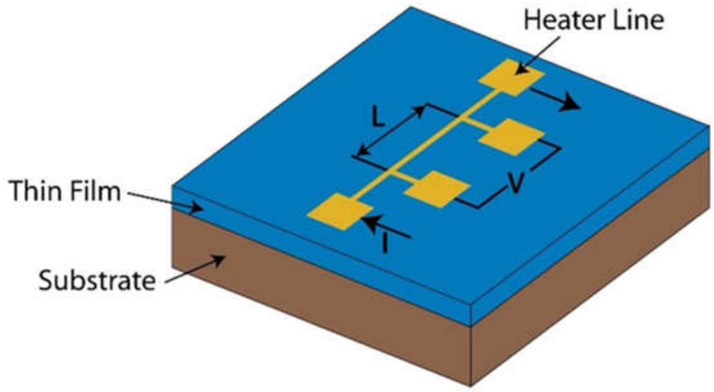

Figure 1.5. 3ω-Method diagram for thermal conductivity measurement for thin films.

Electrical Conductivity Characterization

The electrical conductivity (σ) of thermoelectric materials is determined by measuring their resistivity (ρ) using techniques like the four-probe method and the Van der Pauw method.

Four-Probe Method:

The four-probe method is a very straight-forward one. It minimizes contact resistance effects by using separate current and voltage electrodes. The resistivity is calculated as:

$$\rho = \frac{V \cdot A}{I \cdot L} \tag{1.11}$$

where V is the voltage, I is the current, A is the cross-sectional area, and L is the spacing between the voltage probes. This method is effective for bulk and single-crystal samples.

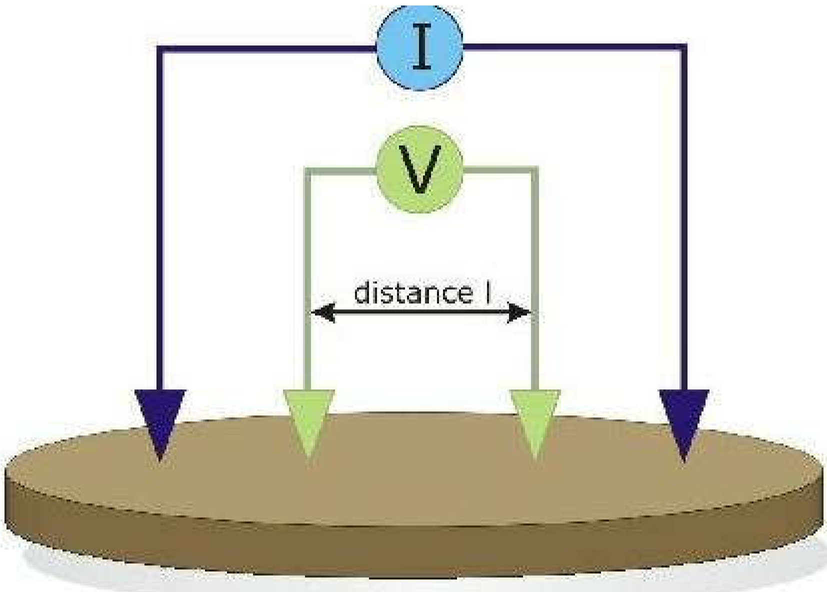

Figure 1.6. A diagram for the four-probe method.

Van der Pauw Method:

The Van der Pauw method [28] is ideal for measuring resistivity and the Hall coefficient in arbitrarily shaped samples. It requires four-point contacts on the sample's perimeter. The author used this method for electric conductivity measurement. The procedure is as follows:

Prepare a uniform, thin sample with no isolated holes.

Attach four small, ohmic contacts to the sample's perimeter, labeled sequentially as A, B, C, and D.

Apply current I_{AB} from contact A to B and measure the voltage V_{CD} across contacts C and D to calculate $R_{AB,CD} = \frac{V_{CD}}{I_{AB}}$.

Repeat for I_{BC} from B to C and measure V_{DA} across D and A to calculate $R_{BC,DA} = \frac{V_{DA}}{I_{BC}}$.

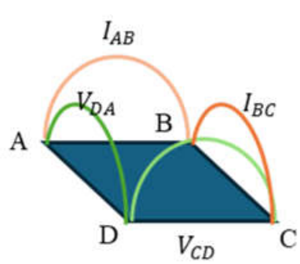

Figure 1.7. Van der Pauw method.

Solve the Van der Pauw equation numerically:

$$e^{-\frac{\pi R_{AB,CD}}{R_S}} + e^{-\frac{\pi R_{BC,DA}}{R_S}} = 1$$

(1.12)

where R_s is the sheet resistance. Multiply the sheet resistance R_s by the sample thickness t to calculate the bulk resistivity:

$$\rho = R_s \cdot t$$

(1.13)

This technique ensures high accuracy, provided the sample is homogeneous, thin, and free of isolated holes.

Seebeck Coefficient Characterization

The Seebeck coefficient (α) quantifies the thermoelectric voltage generated per unit temperature gradient. It is a critical parameter in evaluating the ZT value.

Direct Measurement (Bulk Materials):

In direct measurements, a temperature gradient (ΔT) is applied across the sample, and the resulting voltage (ΔV) is measured. The Seebeck coefficient is simply given by:

$$\alpha = -\frac{\Delta V}{\Delta T}$$

(1.14)

This method is widely used for bulk samples, with systems like ZEM-3 enabling automated temperature control and precise measurement.

Figure 1.8. Advance Riko ZEM-3 and its working principle diagram, located at CEHMS Goodwin lab. [29]

MMR Method (Thin Films):

The MMR method, developed by MMR Technologies, compares the thermoelectric response of a sample with a reference material. The Seebeck coefficient of the sample (α_1) is determined as:

$$\alpha_1 = \alpha_2 \frac{V_1}{V_2} \tag{1.15}$$

where V_1 and V_2 are the voltages generated by the sample and the reference, respectively, under the same temperature gradient. This approach accounts for noise by taking multiple measurements with varying power inputs.

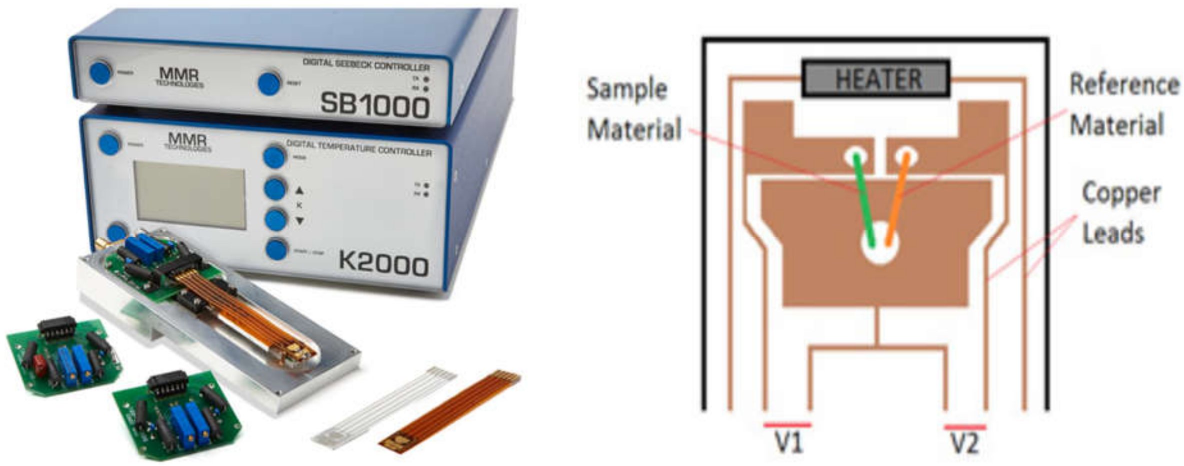

Figure 1.9. MMR Technologies K2000 & SB1000 and the diagram.

1.6 Thermoelectric Physics

This section examines several cutting-edge strategies based on solid state physics for enhancing the thermoelectric figure of merit (ZT). The thermal and electrical characteristics of thermoelectric materials, along with the governing thermodynamic equations, are derived from the Boltzmann transport equation under the single-band approximation.

The key parameter that determines the efficiency of thermoelectric materials is the ZT value, defined as:

$$ZT = \frac{\sigma \alpha^2}{\kappa_e + \kappa_l + \kappa_b} T \tag{1.16}$$

Here, σ is the electrical conductivity, α is the Seebeck coefficient κ_e represents the electronic thermal conductivity, κ_l denotes the lattice thermal conductivity, and κ_b accounts for bipolar heat transfer. Achieving a high ZT requires maximizing both the electrical conductivity and the Seebeck coefficient while minimizing thermal conductivity. However, modifying one property often impacts the others, making the optimization of ZT a complex and multifaceted challenge.

The relationship between ZT and the various transport properties can be explored by Boltzmann transport equation. The N-type carriers in a material can be described by Liouville's equation [30], expressed as:

$$\frac{\partial f^{(N)}}{\partial t} + \sum_{i=1}^{n} \dot{r}^{(i)} \cdot \frac{\partial f^{(N)}}{\partial r^{(i)}} + \sum_{i=1}^{n} \dot{p}^{(i)} \cdot \frac{\partial f^{(N)}}{\partial p^{(i)}} = 0 \tag{1.17}$$

The dynamics of N-type particles can be simplified using the molecular chaos assumption, resulting in the well-known Boltzmann transport equation:

$$\frac{\partial f}{\partial t} + \frac{d\boldsymbol{r}}{dt} \cdot \nabla_r f + \frac{d\boldsymbol{p}}{dt} \cdot \nabla_{\boldsymbol{p}} f = \left(\frac{\partial f}{\partial t}\right)_c \tag{1.18}$$

To make the equation more practical, the relaxation time approximation is introduced:

$$f = f_0 - \tau \left(\boldsymbol{v} \cdot \nabla_{\boldsymbol{r}} f_0 + \frac{\boldsymbol{F}}{m} \cdot \nabla_{\boldsymbol{v}} f_0 \right) \tag{1.19}$$

Here, f_0 represents the equilibrium distribution function, given by the Fermi-Dirac distribution

$$f_0 = f(E) = \frac{1}{e^{\left(\frac{E-E_f}{k_B T}\right)} + 1} \tag{1.20}$$

for electrons or the Bose-Einstein distribution

$$f_0 = f(v) = \frac{1}{e^{\left(\frac{hv}{k_B T}\right)} - 1} \tag{1.21}$$

for phonons and photons.

Electrical Conductivity and Seebeck Coefficient

Considering the first dimension x, the electron distribution function can be described as:

$$f = f_0 - \tau\left(\boldsymbol{v_x} \cdot \nabla_{\boldsymbol{x}} f_0 + \frac{eE_x}{m} \cdot \nabla_{v_x} f_0\right) \tag{1.22}$$

where f is the Fermi-Dirac distribution.

The total current density is determined through adding up the contributions of all electrons traveling in this direction in k-space:

$$J_{ex} = \frac{1}{V}\left[\sum_{k_x=-\infty}^{\infty} \sum_{k_y=-\infty}^{\infty} \sum_{k_z=-\infty}^{\infty} v_x(-e)f\right]$$

Expressing this as an integral:

$$J_{ex} = -\frac{2}{(2\pi)^3} \int_{-\infty}^{\infty} \int_{-\infty}^{\infty} \int_{-\infty}^{\infty} (ev_x f) dk_x dk_y dk_z$$

Substituting the definitions and simplifying, the expression becomes:

$$J_{ex} = -\frac{e}{3}\left(\frac{dE_f}{dx} + eE_x\right)\int_0^{\infty} \tau v^2 \cdot D(E)\frac{\partial f_0}{\partial x} dE = \sigma E_x \tag{1.23}$$

By substituting $\frac{\partial f_0}{\partial x} = -\frac{\partial f_0}{\partial E} \cdot \frac{dE_f}{dx} - \frac{E-E_f}{T}\frac{\partial f_0}{\partial E}\frac{dT}{dx}$ into the equation above, the density becomes:

$$J_{ex} = -\frac{e}{3}\int_0^{\infty} \tau v^2 \cdot \left(\frac{dE_f}{dx} + \frac{E-E_f}{T}\frac{dT}{dx} + eE_x\right) \cdot D(E)\frac{\partial f_0}{\partial E} dE$$

Rewriting these yields:

$$J_{ex} = -\frac{e^2}{3}\int \tau v^2\, D(E)\frac{\partial f_0}{\partial E} dE \cdot \left(-\frac{d\Phi}{dx}\right) + \frac{e}{3T}\int \tau v^2\,(E - E_f)D(E)\frac{\partial f_0}{\partial E} dE \cdot \left(-\frac{dT}{dx}\right)$$

which can be expressed as:

$$J_{ex} = L_{11}\left(-\frac{d\Phi}{dx}\right) + L_{12}\left(-\frac{dT}{dx}\right) \tag{1.24}$$

From this, the electrical conductivity and Seebeck coefficient are derived as:

$$\sigma = L_{11} = -\frac{e^2}{3}\int \tau v^2\, D(E)\frac{\partial f_0}{\partial E}dE = en\mu_e$$

(1.25)

The Seebeck coefficient is then given by:

$$\alpha = -\frac{(d\Phi/dx)}{(dT/dx)} = \frac{L_{12}}{L_{11}} = -\frac{1}{eT}\frac{\int \tau v^2\, D(E)\frac{\partial f_0}{\partial E}\cdot\left(E - E_f\right)dE}{\int \tau v^2\, D(E)\frac{\partial f_0}{\partial E}dE}$$

(1.26)

This formulation highlights that the Seebeck coefficient measures the energy of electrons above the Fermi level. Understanding this, one can interpret why energy filtering techniques are essential in improving ZT value.

Thermal Conductivity

Electronic Thermal Conductivity

The electronic heat flux is derived:

$$J_q = \int \left(E - E_f\right)v_x\, f dv_x dv_y dv_z = L_{21}\left(E_x + \frac{1}{e}\frac{dE_f}{dx}\right) + L_{22}\left(-\frac{dT}{dx}\right)$$

(1.27)

where

$$L_{21} = \frac{e}{3}\int \tau v^2\left(E - E_f\right)D(E)\frac{\partial f_0}{\partial E}dE = TL_{12}$$

$$L_{21} = \frac{e}{3}\int \tau v^2\left(E - E_f\right)D(E)\frac{\partial f_0}{\partial E}dE = TL_{12}$$

Thus:

$$J_q = \frac{L_{21}}{L_{11}}J_e + \left(L_{22} - \frac{L_{12}L_{21}}{L_{11}}\right)\left(-\frac{dT}{dx}\right) = \Pi J_e - \kappa_e\frac{dT}{dx}$$

(1.28)

Where $\Pi = \frac{L_{21}}{L_{11}} = T\alpha$, is the Peltier coefficient, and the electronic thermal conductivity is given by:

$$\kappa_e = L_{22} - \frac{L_{12}L_{21}}{L_{11}}$$

(1.29)

The energy deposited in a differential volume includes heat flux changes and electrochemical potential drop (Joule heat):

$$\dot{Q} = -\frac{dJ_q}{dx} + J_e\left(-\frac{d\Phi}{dx}\right) = -\left(T\frac{dS}{dT}\right)J_e\frac{dT}{dx} + \frac{d}{dx}\left(\kappa\frac{dT}{dx}\right) + \frac{J_e^2}{\sigma}$$

(1.30)

This thermodynamic equation is widely applied in multi-physics simulations of thermoelectric systems.

Lattice Thermal Conductivity

The heat flux can be determined as:

$$J_{qx} = \sum_s \frac{1}{V}\left[\sum_{k_x=-\infty}^{\infty}\sum_{k_y=-\infty}^{\infty}\sum_{k_z=-\infty}^{\infty} v_x\hbar\omega f\right]$$

(1.31)

where s accounts for summation over all polarizations in the k-space, and f follows the Bose-Einstein distribution. This expression can be reformulated first as an integral over wave vectors:

$$J_{qx} = \int_0^{\omega_{max}} d\omega\left\{\int_0^{2\pi}\left[\int_0^{\pi} v\cdot cos\theta\cdot h\omega\left(f_0 - \tau\frac{df_0}{dT}\frac{dT}{dx}v\cdot cos\theta\right)\frac{D(\omega)}{4\pi}\cdot sin\theta\cdot d\,\theta\right]d\varphi\right\}$$

Then write as an integral over energy and solid angle:

$$J_{qx} = -\frac{1}{2}\frac{dT}{dx}\int_0^{\omega_{max}} d\omega\left\{\int_0^{\pi}\tau v^2\cdot sin\theta\cdot cos^2\theta\cdot\hbar\omega D(\omega)\frac{df_0}{dT}d\theta\right\} = -\kappa_l\frac{dT}{dx}$$

(1.32)

The lattice thermal conductivity can then be expressed as:

$$\kappa_l = \frac{1}{3}\int_0^{\omega_{max}}\tau v^2 C_\omega d\omega = \frac{Cv\Lambda}{3}$$

(1.33)

where $\Lambda = \tau v$, $C_\omega = \hbar\omega D(\omega)\, df_0/dT$, and τ relies on frequency.

In the low-temperature regime (below the Debye temperature), the phonon heat capacity is approximated with the Debye model:

$$C(T) = \int_0^{\omega_{max}} C_\omega d\omega = \frac{36\pi^4 k_B}{15}\left(\frac{N}{V}\right)\left(\frac{T}{\theta_D}\right)^3 \propto T^3$$

(1.34)

For high temperatures, the Einstein model gives the phonon specific heat as:

$$C(T) = N_p k_B \left(\frac{N'}{V}\right) \frac{\left(\frac{\hbar\omega_E}{k_B T}\right)^2 \exp\left(\frac{\hbar\omega_E}{k_B T}\right)}{\left[\exp\left(\frac{\hbar\omega_E}{k_B T}\right) - 1\right]^2} = constant$$

(1.35)

The electron contribution to the thermal capacity is calculated as:

$$C_e(T) = \int_0^\infty \left(E - E_f\right)\frac{df}{dT} D(E) dE \approx \frac{1}{2}\pi^2 n_e k_B T / T_f \propto T$$

(1.36)

Bipolar Thermal Conductivity

Electrons and holes both have to be considered in semi-conductors. The currents for each carrier type are:

$$i_1 = \sigma_1\left(E - \alpha_1 \frac{\partial T}{\partial x}\right)$$

$$i_2 = \sigma_2\left(E - \alpha_2 \frac{\partial T}{\partial x}\right)$$

(1.37)

Their respective heat flux densities are:

$$q_1 = \alpha_1 T i_1 - \kappa_{e,1} \frac{\partial T}{\partial x}$$

$$q_2 = \alpha_2 T i_2 - \kappa_{e,2} \frac{\partial T}{\partial x}$$

(1.38)

When the total electrical current is set to zero:

$$i_1 = -i_2 = \frac{\sigma_1 \sigma_2}{\sigma_1 + \sigma_2}(\alpha_1 - \alpha_2)\frac{\partial T}{\partial x}$$

(1.39)

The combined heat flux is:

$$q = q_1 + q_2 = -\left(\kappa_{e,1} + \kappa_{e,2} + \frac{\sigma_1 \sigma_2}{\sigma_1 + \sigma_2}(\alpha_1 - \alpha_2)^2 T\right)\frac{dT}{dx}$$

(1.40)

The bipolar thermal conductivity is:

$$\kappa_b = \frac{\sigma_1 \sigma_2}{\sigma_1 + \sigma_2}(\alpha_1 - \alpha_2)^2 T$$

(1.41)

To reduce κ_b, the density of minor carriers must be reduced. Thus, thermoelectric materials should be heavily doped.

ZT Value

To gain a deeper understanding of the relationships between thermal and electrical properties, as well as strategies to improve the energy efficiency of TE materials, this section focuses on calculating ZT for metals and semiconductors using the classical single-band theory.

Based on the earlier derivations, the coupling coefficients can be succinctly expressed as:

$$L_{11} = -e^2 K_0$$

$$L_{12} = -eK_1$$

$$L_{21} = -\frac{e}{T}K_1$$

$$L_{22} = -\frac{1}{T}K_2$$

Here, K_s is given by:

$$K_s = -\frac{1}{3}\int \tau v^2 D(E)\frac{\partial f_0}{\partial E}E^s dE, \qquad s = 1, 2, 3.$$

(1.42)

Assuming that $\tau = \tau_0 E^r$, and the Fermi surface is spherical ($v^2 = \frac{2E}{3m^*}$), the expression for K_s becomes:

$$K_s = -\frac{8}{3}\left(\frac{2}{h^2}\right)^{\frac{3}{2}}(m^*)^{\frac{1}{2}}T\tau_0 \int \frac{\partial f_0}{\partial E} E^{r+\frac{3}{2}+s}\, dE$$

(1.43)

In this context, the integral:

$$F_n(E) = \int \frac{\partial f_0}{\partial E} E^{r+\frac{3}{2}+s}\, dE$$

is referred to as the Fermi-Dirac integral.

The scattering factor, r, varies depending on the dominant scattering mechanism. Typical values of r for different mechanisms are outlined in the following table:

Table 1.1. Phonon scattering factors

Scattering mechanism	Scattering factor (r)
Acoustic	-1/2
Alloy	-1/2
Neutral impurity	0
Optical	1/2
Ironic	3/2

These values for r allow for specific calculations of K_s under different conditions. This provides insights into the thermoelectric properties of materials, as well as avenues for optimizing performance metrics such as ZT value.

Non-Degenerate Case

In the non-degenerate limit ($\eta = \frac{E-E_f}{k_B T} \ll 0$), the Fermi-Dirac integral becomes:

$$F_n(\eta) = \exp(\eta) \int \xi^n exp(-\xi)\, d\xi = exp(\eta)\Gamma(n+1)$$

(1.44)

Using this, Equation (1.43) becomes:

$$K_s = -\frac{8\pi}{3}\left(\frac{2}{h^2}\right)^{\frac{3}{2}}(m^*)^{\frac{1}{2}}T\tau_0 (k_B T)^{r+\frac{3}{2}+s} exp(\eta)\Gamma\left(r+\frac{5}{2}+s\right)$$

Substituting K_s into Seebeck coefficient equation:

$$\alpha = \pm\frac{1}{T}\frac{L_{21}}{L_{11}} = \pm\frac{k_B}{e}\left[\eta - \left(r + \frac{5}{2}\right)\right]$$

(1.45)

The electrical conductivity is expressed as:

$$\sigma = -e^2 K_0 = -\frac{8\pi e^2}{3}\left(\frac{2}{h^2}\right)^{\frac{3}{2}}(m^*)^{\frac{1}{2}}T\tau_0(k_B T)^{r+\frac{3}{2}}exp(\eta)\Gamma\left(r + \frac{5}{2}\right)$$

(1.46)

The Lorenz number, which relates thermal conductivity to electrical conductivity, is given by:

$$L = \frac{\lambda T}{\sigma} = \frac{1}{e^2 T^2}\left(\frac{K_2}{K_0} - \frac{K_1^2}{K_0^2}\right) = \left(\frac{k_B}{e}\right)^2\left(r + \frac{5}{2}\right)$$

(1.47)

The electron density:

$$n = \int f(E)g(E)dE = 2\left(\frac{2\pi m^* k_B T}{h^2}\right)^{3/2} exp(\eta)$$

(1.48)

Then ZT value becomes:

$$ZT = \frac{\alpha^2\sigma T}{\kappa_l + \kappa_e} = \frac{\alpha^2}{\frac{\kappa_l}{\sigma T} + L} = \frac{\left[\left(r + \frac{5}{2}\right) - \eta_f\right]^2}{\left[\beta exp(\eta_f)\right]^{-1} + L}$$

(1.49)

where $\beta = \left(\frac{k_B}{e}\right)^2 \frac{\sigma_0}{k_l}T$, and $\sigma_0 = 2e\mu\left(\frac{2\pi m^* k_B T}{h^2}\right)^{3/2}$. Here, ZT only depends on $\beta$and η_f.

To optimize doping levels, solve $\frac{\partial(ZT)}{\partial\eta_f} = 0$:

$$\eta_{opt} + 2\left(r + \frac{5}{2}\right)\beta \cdot exp(\eta_{opt}) = r + \frac{1}{2}$$

(1.50)

For materials with 0<β<0.5, the optimal doping level depends on the scattering factor r:

When $0 < \beta < 0.5$, $\eta_{opt} > -1.3$.

When $\beta \ll 1$, $\eta_{opt} < 2$.

Thus, the optimal dimensionless Fermi level falls within $-1.3 < \eta_{opt} < 2$. The corresponding doping concentration is:

$$n = \frac{(m^*)^{1/2}}{2\pi^2}\frac{(2k_BT)^{3/2}}{\hbar^3}F_{r+\frac{1}{2}}(\eta_{opt})$$

(1.51)

Despite the non-degenerate condition $\eta \ll 0$, these results remain applicable in most cases. The optimal doping level is typically $n = 10^{25\sim 26}\ m^{-3}$.

To determine the optimal Seebeck coefficient, solve $\frac{\partial(ZT)}{\partial\alpha} = 0$:

$$\alpha\left(\frac{d}{d\alpha}\log\alpha\right) = -2\left[1 + \frac{\kappa_e}{\kappa_l}\left(1 - \frac{1}{2}\cdot\frac{d(\log L)}{d(\log\alpha)}\right)\right]$$

(1.52)

The solution is:

$$\alpha_{opt} = -172\left(1 + \frac{\kappa_e}{\kappa_l}\right)$$

(1.53)

For most thermoelectric materials, where $\frac{\kappa_e}{\kappa_l} = 0.15\sim 0.5$, the optimal Seebeck coefficient lies in the range $\alpha_{opt} = 200\sim 250\ \mu V/K$. While this estimate might slightly deviate from exact values due to the violated non-degenerate assumption, the variation is negligible in practice.

Assuming $\beta = 0.5$ and dominant ionic scattering, an optimum ZT of 3.0 is achievable at $\eta_{opt} \approx 0.8$. Thus, a ZT value of approximately 4.0 is considered a realistic upper limit for bulk semiconductor-based thermoelectric materials.

Degenerate Case

In the degenerate regime ($\eta = \frac{E-E_f}{k_BT} \gg 0$), which are metals, typical of metals, the Fermi-Dirac integral approximately becomes:

$$F_n(\eta) = \exp(\eta)\int \xi^n exp(-\xi)\,d\xi = \frac{\eta^{n+1}}{n+1} + \frac{\pi^2}{6}n\eta^{n-1} + \cdots$$

(1.54)

Using this approximation, the Seebeck coefficient simplifies to:

$$\alpha = \pm \frac{\pi^2}{3} \frac{k_B}{e} \frac{r + \frac{3}{2}}{\eta}$$

(1.55)

The electrical conductivity is expressed as:

$$\sigma = -\frac{8\pi e^2}{3} \left(\frac{2}{h^2}\right)^{\frac{3}{2}} (m^*)^{\frac{1}{2}} \tau_0 (k_B T)^{r+\frac{3}{2}} \eta^{3/2}$$

(1.56)

In this regime, the Lorenz number becomes:

$$L = \frac{\lambda T}{\sigma} = \frac{1}{e^2 T^2} \left(\frac{K_2}{K_0} - \frac{K_1^2}{K_0^2}\right) = \frac{\pi^2}{3} \left(\frac{k_B}{e}\right)^2 = constant$$

(1.57)

This constant value of L is a key result of the Wiedemann-Franz law.

For metals, the dimensionless figure of merit ZT is bounded by:

$$ZT \leq \frac{3\pi^2}{64} = 0.46, \qquad \text{if } \xi > 4$$

(1.58)

This upper limit applies universally to metallic materials.

Limitations and Extensions of the Single-Band Model

The single-band model, as applied here, estimates the maximum expectation of ZT value. When the Fermi level is too apart from the conduction band, the Seebeck coefficient diverges, implying an unrealistic ZT value. In reality, this divergence does not occur. To address this issue, a two-band model was introduced. [31]

Using the two-band approach, ZT predictions include:

- ZT<4.0 at room temperature for acoustic phonon scattering as the dominant mechanism.
- ZT<4.0 at T=1200K and ZT<2 at room temperature when both acoustic and optical phonons contribute significantly.

These conclusions, based on the best material properties available at the time, remain valid today, even when applied to nanomaterials.

1.7 ZT Value Enhancement

Based on the calculation above, enhancing ZT requires maximizing σ and α, while minimizing k_l and k_e. This interplay introduces complex challenges as these parameters are often interdependent.

Increasing $\boldsymbol{\beta}$

As shown in Equation (1.49), $ZT \propto \beta$, making β a critical parameter for improving thermoelectric performance. Defined as:

$$\beta = \left(\frac{k_B}{e}\right)^2 \frac{\sigma_0}{\kappa_l} T \propto \frac{\mu m^{*3/2}}{\kappa_l}$$

(1.59)

β depends on the carrier mobility (μ), effective mass (m^*), and lattice thermal conductivity (κ_l).

Materials with multiple conduction or valence band valleys, such as Bi_2Te_3, PbTe, and half-Heusler alloys, inherently support higher m^*. Converging bands in the Brillouin zone, observed in n-type $Mg_2Si_{1-x}Sn_x$ and $PbTe_{1-x}Se_x$, increases band extrema (N_V), boosting β. [32, 33]

Altering band curvature through doping enhances m^*. For instance, Tl-doped PbTe increases $\boldsymbol{\beta}$ by introducing resonant states, while Sb-doped Bi_2Te_3 improves thermoelectric performance. [7, 17]

Band Engineering to Optimize α and σ

The Seebeck coefficient is expressed as:

$$\alpha = \frac{\pi^2}{3}\frac{k_B^2 T}{e}\left\{\frac{1}{n}\frac{dn}{dE} + \frac{1}{\mu}\frac{d\mu}{dE}\right\}\bigg|_{E=E_F}$$

(1.60)

where n is the carrier density, μ is the carrier mobility, k_B is the Boltzmann constant, e is the electronic charge, and E_F is the Fermi level. Band convergence involves aligning multiple conduction or valence bands to enhance the density of states ($g(E)$) near the Fermi level. This increases the effective mass (m^*) of carriers without significantly decreasing mobility (μ).

The density of states for a parabolic band is:

$$g(E) \propto N_V m^* \sqrt{E - E_c}$$

(1.61)

where N_V is the number of band extrema, and E_c is the conduction band minimum. Aligning multiple bands increases N_V, thereby enhancing α. Examples include n-type $Mg_2Si_{1-x}Sn_x$ and $PbTe_{1-x}Se_x$ [4, 17].

Doping can introduce localized energy levels near E_F, creating a sharp increase in $g(E)$, which boosts α (Mahan-Sofo theory). [34] Tl-doped PbTe is a prominent example, where resonant states significantly enhance thermoelectric performance.

Carrier Concentration Optimization

Carrier concentration directly influences both σ and α. [19] The Wiedemann-Franz law relates electronic thermal conductivity (κ_e) to σ:

$$\kappa_e = L\sigma T \tag{1.62}$$

where L is the Lorenz number. High σ increases κ_e, reducing ZT value. Optimal carrier concentration balances these effects, typically in the range $10^{25\sim26}m^{-3}$, depending on the material. [6]

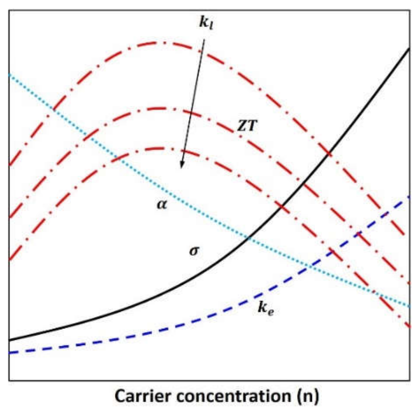

Figure 1.10. Carrier concentration balance.

Reducing Lattice Thermal Conductivity

Alloying and Phonon Scattering

The lattice thermal conductivity can be reduced using alloying, which introduces mass and strain disorder to scatter phonons. This approach is effective in systems like SiGe alloys. [34]

As mentioned above (Equation 1.29), the lattice thermal conductivity is expressed as:

$$\kappa_l = \frac{Cv\Lambda}{3}$$

Reducing the phonon mean free path Λ through alloying effectively lowers κ_l.

Nanostructuring

Nanostructures, such as superlattices and nanoinclusions, scatter phonons across different wavelengths:

- Superlattices create acoustic mismatch at interfaces.
- Nanoinclusions introduce localized strain fields.

This hierarchical scattering reduces κ_l to the amorphous limit without significantly affecting σ. [35]

Enhancing Density of States with Low-Dimensional Structures

In low-dimensional materials, quantum confinement modifies $g(E)$. The density of states for different dimensions is as follows:

Table 1.2. Density of states for different dimensions.

Dimension	Density of States
Bulk Materials (3D)	$g(E) \propto \sqrt{E - E_c}$
Quantum Wells (2D)	$g(E) \propto constant$
Quantum Wires (1D)	$g(E) \propto \frac{1}{\sqrt{E - E_c}}$
Quantum Dots (0D)	$g(E) \propto E - E_c$

This confinement enhances α. Hicks and Dresselhaus predicted ZT>6 in Bi_2Te_3 quantum wells. [7]

1.8 Additive Manufacturing for Thermoelectric Materials

Additive manufacturing (AM), commonly known as 3D printing, has emerged as a transformative technology in materials science, offering unprecedented design flexibility and the ability to fabricate complex geometries with high precision. In the realm of thermoelectric (TE) materials—substances that convert heat into electricity and vice versa—AM presents unique opportunities to enhance performance and expand application possibilities.

Thermoelectric Materials and Their Challenges

Thermoelectric materials are characterized by their ability to directly convert thermal gradients into electrical voltage, a property quantified by the dimensionless figure of merit, ZT, as specified above in Equation 1.6.

$$ZT = \frac{\alpha^2 \sigma T}{\kappa}$$

Achieving a high ZT requires a delicate balance: maximizing Seebeck coefficient α and electrical conductivity σ while minimizing total thermal conductivity κ.

Traditional manufacturing methods, such as hot pressing and spark plasma sintering, impose limitations on the achievable microstructure and geometry, hindering the exploration of novel designs and materials. AM addresses these limitations by enabling the fabrication of intricate architectures and controlled microstructures, thus unlocking new possibilities for thermoelectric material development.

Advantages of Additive Manufacturing in Thermoelectrics

AM techniques, such as selective laser melting (SLM) and direct ink writing (DIW), enable layer-by-layer construction of materials, allowing for precise control over composition and microstructure. This capability offers several advantages for thermoelectric materials:

1. **Complex Geometries**: AM allows the fabrication of porous and hierarchical structures that enhance phonon scattering and reduce lattice thermal conductivity (κ_l) without significantly affecting electrical properties. Tailored architectures, such as interconnected pores and graded structures, have been shown to improve ZT in materials like bismuth telluride (Bi_2Te_3) [18] and silicon-germanium alloys [36].
2. **Material Efficiency**: Unlike subtractive manufacturing, which generates significant waste, AM builds components additively, minimizing material waste and reducing costs. This advantage is particularly critical for expensive thermoelectric materials like tellurides and skutterudites.
3. **Composition and Microstructure Control**: The layer-by-layer deposition inherent in AM enables precise control over material composition and microstructure. This control facilitates the introduction of dopants, compositional gradients, and nanoscale features that enhance the Seebeck coefficient (α) and electrical conductivity (σ). [37]
4. **Multi-Material Integration**: AM supports the fabrication of multi-material structures, allowing the seamless integration of materials with complementary properties. For instance, materials with high α\alphaα can be combined with those offering low thermal conductivity, creating devices optimized for specific applications. [38]

Some of the ZT enhancement methods mentioned in section 1.7 are possible via the additive manufacturing methods:

1. **Tailored Phonon Scattering**

   AM enables the design of architectures that scatter phonons effectively across multiple length scales. Hierarchical structures, combining nanostructures for high-frequency phonon scattering with microscale features for low-frequency scattering, can significantly reduce κ_l. For example, studies on nanostructured Bi_2Te_3 fabricated via direct ink writing [37] have demonstrated enhanced phonon scattering and improved ZT.

2. **Optimizing Carrier Concentration**

Precise doping through AM processes, such as binder jetting with dopant inks, allows fine-tuning of carrier concentration. This capability enables optimization of the power factor ($\alpha^2\sigma$) by balancing the Seebeck coefficient and electrical conductivity. [39]

3. **Band Structure Engineering**

   The controlled introduction of compositional gradients and alloying through AM facilitates band structure engineering, which can increase the effective mass (m^*) of carriers and enhance α. For instance, PbTe alloys processed using selective laser melting (SLM) have shown improved thermoelectric performance due to optimized band convergence. [40]

4. **Quantum Confinement Effects**

   AM's ability to fabricate low-dimensional structures, such as nanowires and thin films, allows the exploitation of quantum confinement effects. These effects alter the density of states near the Fermi level, enhancing the Seebeck coefficient. Hicks and Dresselhaus predicted a significant increase in ZT for 2D and 1D thermoelectric materials, and AM provides a pathway to realize these structures. [7]

Currently, there are several AM methods that have been researched to be applicable to TE materials:

Selective Laser Melting (SLM)

SLM has been used to fabricate dense Bi_2Te_3 components with tailored microstructures, achieving ZT values comparable to those obtained via traditional sintering methods. [41] That is also the technique that the dissertation researched about.

Direct Ink Writing (DIW)

DIW enables the creation of complex architectures with controlled porosity, improving phonon scattering. Studies on DIW-processed Bi_2Te_3-based materials have demonstrated reduced thermal conductivity and enhanced performance. [42]

Despite its potential, additive manufacturing (AM) faces several challenges that must be addressed to fully realize its application in thermoelectric materials. One significant issue is material compatibility, as not all thermoelectric materials can be easily adapted to AM processes due to concerns such as thermal stability and powder flowability. Additionally, achieving the desired microstructure and properties requires meticulous process optimization, including precise control over parameters such as laser power, scan speed, and layer thickness.

Another critical challenge lies in scaling up the technology. While laboratory-scale demonstrations have shown promise, transitioning to industrial-scale production remains a substantial hurdle. Furthermore, the high cost of materials and AM equipment presents a barrier to widespread adoption, particularly for thermoelectric applications that often rely on expensive components.

This dissertation prioritizes the development of AM techniques tailored specifically for thermoelectric materials. This includes exploring materials that are compatible with AM technologies and integrating computational physical modeling to predict and optimize performance. Addressing these challenges will be key to unlocking the full potential of AM in advancing thermoelectric materials and devices.

1.9 Selective Laser Melting and Direct Energy Deposition

Among the diverse AM techniques, Selective Laser Melting (SLM) and Directed Energy Deposition (DED) have emerged as prominent methods for fabricating weldable materials.

Selective Laser Melting (SLM)

SLM is a powder bed fusion (PBF) technique that fabricates parts by selectively melting successive layers of metal powder using a high-energy laser beam. The process begins with the deposition of a thin layer of powder onto a build platform. A laser beam, guided by computer-aided design (CAD) data, scans the powder bed, melting the powder particles in specified areas to form a solid cross-section of the part. Once a layer is completed, the build platform lowers, and a new layer of powder is spread over the previous one. This cycle repeats until the entire part is constructed.

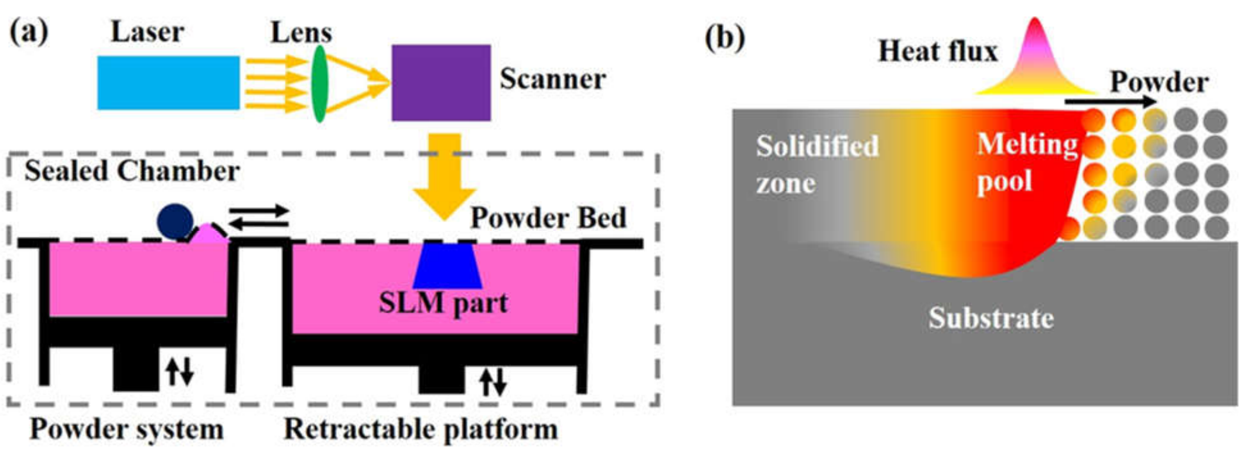

Figure 1.11. (a) The SLM equipment diagram and (b) the molten pool mechanism.

SLM is utilized in industries requiring high precision and complex geometries, such as aerospace, automotive, medical, and dental sectors [43]. It is particularly advantageous for producing lightweight structures, intricate lattice designs, and components with internal channels that are challenging to achieve through traditional manufacturing methods.

Advantages

- **Design Flexibility:** SLM enables the creation of complex and customized geometries without the need for specialized tooling.
- **Material Efficiency:** The process minimizes waste, as unused powder can often be recycled.
- **High Precision:** SLM produces parts with fine details and high dimensional accuracy.

Challenges

- **Residual Stresses:** Rapid heating and cooling cycles can induce residual stresses, leading to part distortion or cracking.
- **Surface Finish:** Parts may require post-processing to achieve the desired surface quality.
- **Material Limitations:** Not all metals are suitable for SLM due to issues like oxidation or poor flowability of powders.

Directed Energy Deposition (DED)

DED is an additive manufacturing process that utilizes focused thermal energy—such as a laser, electron beam, or plasma arc—to fuse materials by melting them as they are deposited. Unlike SLM, which uses a powder bed, DED feeds material in the form of powder or wire directly into the energy source. The material is melted upon deposition, allowing for the construction of parts layer by layer. DED systems often employ multi-axis robotic arms or gantry systems to manipulate the deposition head, enabling the fabrication of complex geometries and the repair of existing components.

Directed Energy Deposition (DED) is extensively utilized in industries such as aerospace [44], defense, and energy for a variety of applications [45]. One of its key uses is in repair and maintenance [46], where it restores worn or damaged components, including turbine blades and molds, to their original functionality. DED is also employed for feature addition [47], allowing the precise addition of material to existing parts to modify or enhance their performance. Furthermore, it is a valuable tool for prototyping and low-volume production, enabling the fabrication of large-scale components or prototypes with intricate geometries that would be challenging to produce using conventional manufacturing methods.

Advantages

- **Versatility:** DED can process a wide range of materials and is suitable for both manufacturing new parts and repairing existing ones.
- **High Deposition Rates:** The process allows for the rapid building of large components.
- **Material Efficiency:** DED enables the addition of material only where needed, reducing waste.

Challenges

- **Dimensional Accuracy:** Achieving high precision can be challenging due to factors like thermal distortion.
- **Surface Finish:** Parts often require post-processing to meet surface quality standards.
- **Process Complexity:** Controlling process parameters to achieve desired material properties requires expertise.

Selective Laser Melting and Directed Energy Deposition represent significant advancements in additive manufacturing, each offering unique capabilities and advantages. This dissertation researches about their principles, processes, materials, applications, and challenges, which essential for selecting the appropriate technique for specific manufacturing needs.

This chapter is adapted from a published paper of the author, "Self-powered Through-wall communication for dry cask storage monitoring", listed in the Publications section.

2 Chapter 2. Self-powered Through-wall Communication for Dry Cask Storage Monitoring

2.1 Chapter Introduction

Since 1990, nuclear power plants have generated about 20% of U.S. electricity. [48] As a result, a large amount of spent nuclear fuel needs to be stored carefully to prevent environmental pollution and protect human beings from potential radiation hazards. Typically, one-third of the fuel elements in nuclear reactors are replaced every 18 months, and the United States Nuclear Regulatory Commission (NRC) estimates that 70,000 metric tons of uranium (MTU) are contained as spent fuel [49]. Currently, there are two available storage methods for spent fuel after it is removed from the reactor core, e.g., spent fuel pools and dry cask storage. Spent fuel pools are built with almost every nuclear power plant for the convenience and the necessity to preliminarily cool down the spent fuel under at least 20 feet of water, though they are huge and need frequent maintenance. [50] The security study of the spent fuel pool is still one of the weakest points when the plant is hit by natural disasters, such as earthquakes and tsunamis. For example, during the Fukushima Daiichi nuclear disaster, the spent fuel pool in Unit 4, hit by the hydrogen explosion from Unit 3, overheated and created two large holes in the wall of the outer building. [51]

Dry cask storage is designed to contain and seal the spent nuclear fuel already cooled down in the spent fuel pools for five years, with an inert gas environment and a steel cask [52]. Besides the steel cask, there are additional nuclear shielding layers made of steel, concrete, and other radiation resistance or absorbing materials to protect workers and the public. Though the cask is strictly sealed and protected, the situation inside the cask is very harsh and complex, which needs to be monitored timely for safe storage up to 50 years. Different methods have been developed to monitor the health of the cask [53]. However, no effective sensing and instrumentation system can provide direct measurements of the inner conditions because of (1) unavailable long-lasting electricity power supply for sensors and electronics inside the enclosed canisters, (2) unable to transferring the data out of the enclosed steel cask, and (3) unsustainable electronics and sensors in the harsh environment of high temperature (150–175°C on the wall surface) and high radiation.

Batteries are still the mostly used power source for sensors in most monitoring systems. However, limited energy capacity of batteries requires periodical replacement or recharging, which is also unfeasible in the strictly sealed environment of a canister. Research showed that radiation dose less than 10 Mrads could result in 56% higher failure rate and a significant battery capacity fade for a lithium-ion battery. [54] In contrast, the energy inside the canister is abundant due to the remaining decay of the spent nuclear fuel [55], which brings a lot of heat and radiation. The

Westinghouse Electric Company has developed a method that could generate electricity from gamma radiation. [56] Metal layers with a relatively high atomic number (Z) were used to form a high-temperature emitter, and an electrical conductor with a relatively low Z value forms a collector. The Compton and photoelectric electrons produced by gamma radiation have sufficient energy to penetrate the metal resistor layer and will be stopped in the collector. This effect creates a voltage difference between the emitter and the collector. The gamma radiation and the thermal energy can be harvested to generate electricity in the given environment. Thermoelectric energy generators can be also used to convert the temperature difference inside the canister into electricity because of its solid-state nature, which is highly appreciated in a high-energy and harsh environment [57] with good radiation tolerance. [58] The efficiency of a bismuth telluride based thermoelectric materials with ZT value close to 1 [59] can be around 8% at a temperature of over 150 ℃. [60] Considering the decay heat rate of the spent fuel and the high temperature [61], a thermoelectric energy harvester can be integrated into the monitoring system for a sustainable power supply for sensors and data transmission, which yields a self-powered wireless through-wall communication system.

The thick metal sealing structure of the nuclear spent fuel canister also raises another challenge to wireless communication. Conventional electromagnetic wireless data transfer techniques are impractical and highly inefficient for enclosed canisters due to the Faraday shield presented by the thick metal barrier. [62] Carstens et. al. built a system of thermoelectric powered wireless sensors outside the canister for dry-cask storage [63]. However, the electromagnetic wireless communication is hard to extend inside the canister due to the metal shielding effect. Acoustic waves generated by piezoelectric devices have proven to be a reliable method to penetrate through the thick protection layers and efficiently transmit information at a high rate. Ultrasonics provide a viable solution to transmit signal from inside a container to the outside world without wiring and holes, as two perfectly aligned piezoelectric transducers attached on both sides of a metal wall could communicate through the coupled vibrations. Binary data from the sensor could be mixed with the carrier wave and "penetrate" through thick metal barriers. Multiple papers have been reported for the "through-wall data transmission." [64-69]

In addition, electronics also need to survive in the high temperature and radiation environment of the enclosed spent fuel canister for effective power management, sensing, data coding, and transmission. Ionizing radiation inside the dry cask is a significant threat to the circuits because of the corruption in memory bits, glitches in digital and analog circuits, increase in power consumption, speed reduction, and even complete loss of functionality [70](and Gerardin, 2018). The electronics for self-powered monitoring and ultrasound communication system of the spent nuclear canister should include, 1) power electronics to manage and store the harvested energy in a high-temperature super capacitor; 2) sensing electronics to power the sensors, collect data, and encode data for transmission; 3) signal transceiver electronics to generate the ultrasonic signal at the carrier frequency, drive the inside piezoelectric transducer to transmit the data through the metal wall, and demodulate the received signal. These circuits must tolerate a radiation dose rate of 33 kRad/hr and a temperature of 150°C for the planned lifetime of the dry cask. [71]

To the best of the authors' knowledge, there is no self-powered condition monitoring and wireless through-wall data communication technology in literature for spent nuclear fuel canisters that have been experimentally demonstrated. This study aims to address the above-mentioned challenges in spent nuclear canister monitoring and wireless data communication by developing energy harvesting, thorough-wall ultrasound wireless communication, and harsh environment electronics. The specific objectives of this work include: (1) Directly harvest electrical energy from the gamma rays and temperature gradient inside the spent fuel canister. (2) Transmit a large amount of sensing data through the metal wall and thick shielding layers via ultrasound. (3) Design, develop, and deploy electronics for a functional demonstration of the complete system. (4) Provide a design, fabrication, and shielding strategy for future realization of high-temperature and radiation-hardened electronics circuits and communication systems. (5) In-lab test and demonstration of the proposed self-powered monitoring and wireless through-wall data transmission system.

2.2 The Harsh Environment in the Dry Cask Storage

The knowledge and detailed investigation of the environment inside the dry cask, such as temperature, radiation intensity, and flow field [72], is necessary to guide the design and analysis of the proposed thermoelectric energy harvesting, electronics, and transducers for wireless data transmission. The temperature and flow velocity within the canister should be well analyzed over the lifetime of the cask. The strong convective heat transfer process inside and outside the canister creates a large temperature drop near the canister wall, making it an ideal place for thermoelectric energy harvesting. In this section, a vertical HI-STORM-100 dry storage cask with a Multi-Purpose MPC-32 canister containing 32 high-burnup (45 GWd/MTU) PWR spent fuel assemblies (Westinghouse PWR 17x17) for storage of 50 years was briefly introduced and numerically simulated, which have been reported in our previous research. [73] The input decay heat value was predicted for the fuel assembly using the existed program ORIGAMI integrated into SCALE. [74] The simulation results provided comprehensive thermal-fluid dynamic data to guide the dry cask inner structure design and thermoelectric energy harvesting powered device placement.

The simulation utilized a Westinghouse 17x17 fuel assembly design, with a total of 15 MTU within the cask distributed across 32 assemblies. Each assembly had a U235 enrichment of 4% by weight, a burnup level of 45 GWd/MTU, and underwent three operational cycles per assembly, with an average power output of 40 MW/MTU. This configuration was representative of a typical assembly being discharged from a reactor, as modern fuel generally features a U235 enrichment between 3% and 5% and achieves burnup levels of approximately 45 GWd/MTU. The use of this average fuel provided a standard reference for analyzing decay heat trends and magnitudes. It was assumed the reactor core contained 90 MTU, distributed uniformly among 193 assemblies. From this assumption, the power output per assembly was calculated. The total power of the MPC-32 cask, along with associated gamma and neutron emission rates, was analyzed over time, starting from five years post-reactor discharge (commencement of dry cask storage) and extending to 55 years, representing 50 years of dry storage duration.. Along with the life span, the decay heat falls from 38.44 kW to 10.67 kW, the gamma radiation intensity falls from 3.64*10^17/s to 4.6*10^16/s, and the neutron radiation intensity falls from 1.02*10^10/s to 1.7*10^9/s. [75]

The k-ε and transitional SST k-ω model were both included because of the turbulence predicted by a Reynolds number of 3000. The temperature profiles of both the 5-year situation and 55-year ones are presented in Figure 2.1 (I) and (II), respectively. Year 5 means the spent fuel was just loaded to the canister after 5 years of cooling in the water pools. Year 55 is at the end of 50 years of service life of the canister. The result in Figure 2.1 (I) showed a peak temperature of 613 K. The simulation outcomes delivered extensive thermal-fluid dynamics information, serving as a valuable reference for the future design of dry cask internal structures and optimal placement of devices utilizing thermoelectric energy harvesting.

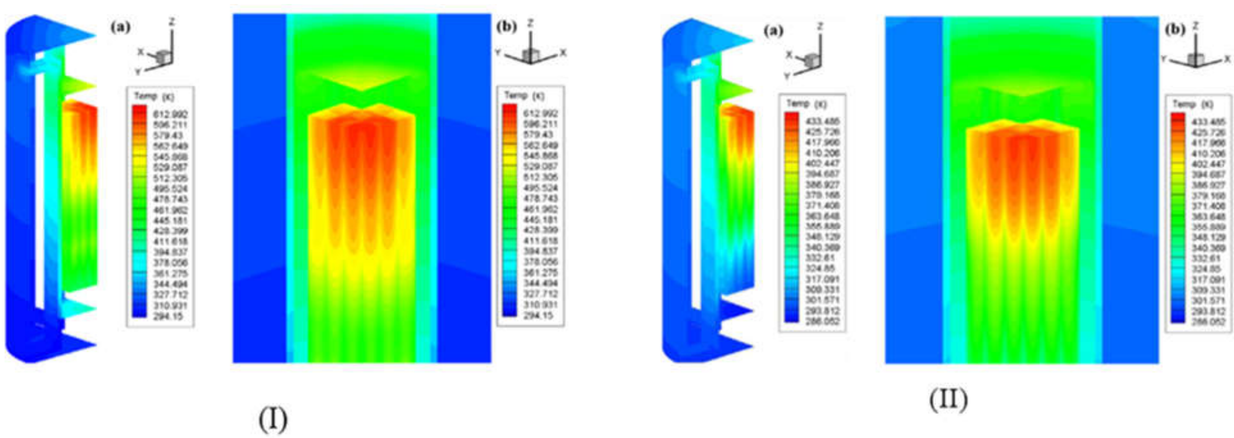

Figure 2.1. The temperature profiles in the canister at (I) year 5 and (II) year 55. (a) Temperature profiles of the entire dry casks and (b) local temperature profiles of the spent fuel assemblies. [73]

According to the simulation results, the strong convective heat transfer process inside and outside the MPC creates a large temperature drop near the canister wall, making it an ideal place for thermoelectric energy harvesting. Figure 2.1 shows the temperature profiles for years 5 and 55 (50-years dry cask storage) superimposed on each other. As can be seen, there is an enduring temperature gradient present between the fuel, helium gap, and MPC wall, and an enduring helium circulation flow along both the wall of the fuel basket, and the wall of the MPC canister generated from convection in the helium. Using these results as a guideline, a thermoelectric energy harvester can be designed to take advantage of the existing temperature gradient. Considering there are strong gamma radiation sources within the canister, gamma radiation could be utilized by converting its energy into material heating in tungsten. The tungsten plate can create a localized hot spot. [76] This should help to increase the temperature drop at the local site. A detailed design of the thermoelectric energy harvester for the wireless sensing and monitoring network for the canister or closed vessels is elaborated in the following.

The decay heat, gamma intensity, and neutron intensity from the 15 MTUs of spent fuel for 50 years of service life of canisters (Year 5-55) are shown in table below.

Table 2.1. Heat and radiation vs service year.

Year (Since removal)	Decay Heat (kW)	Gamma Intensity (#/s)	Neutron Intensity (#/s)
5	38.44	2.64×10^{17}	1.02×10^{10}
10	24.52	1.47×10^{17}	8.4×10^{9}
15	21.07	1.20×10^{17}	7.0×10^{9}
20	19.00	1.04×10^{17}	5.9×10^{9}
25	17.31	9.2×10^{16}	4.9×10^{9}
30	15.85	8.2×10^{16}	4.1×10^{9}
35	14.56	7.3×10^{16}	3.4×10^{9}
40	13.42	6.5×10^{16}	2.9×10^{9}
45	12.40	5.8×10^{16}	2.4×10^{9}
50	11.49	5.1×10^{16}	2.0×10^{9}
55	10.67	4.6×10^{16}	1.7×10^{9}

2.3 Energy Harvesting and Power Management

Powering the sensors and electronics in the harsh high-temperature and radiation environment inside the canister is quite challenging since traditional batteries will not work. Wiring through holes in the vessel walls for grid power is undesirable and largely unfeasible in nuclear environments. Therefore, the development of an independent energy harvesting system to power the system is of critical importance. To take advantage of the gamma radiation and thermal convection inside the canister, two energy harvesters were designed, examined, and evaluated. Energy harvesting circuits are designed to manage the harvested energy and power the sensing and data communication. In-lab tests are conducted to validate the targeted performance of the power electronics.

2.3.1 Energy harvesting from radiation and thermal flow inside the canister

Energy harvesting from the gamma radiation

Gamma radiation induces a temperature difference that could be harvested and converted into electricity using a thermoelectric energy generator. Specifically, the gamma rays are absorbed by a target tungsten plate, which will be heated up and create a local high-temperature hot spot. A tungsten layer was applied to the fuel basket wall and isolated from the helium gas by high-temperature thermal-insulation plastic. The overall design is illustrated in Figure 2.2 (a), where two HZ-2 TEG modules made of Bi_2Te_3 were used. The 2nd TEG connected to the canister wall with its cold end. The gross size of the gamma heating device was 30 × 30 × 18 cm^3. Simulation results using MCNP6 [77, 78] showed that the heat source in a tungsten plate of 20×20×2 cm^3, exposed to radiation, could receive 2.0 W of gamma heating at the beginning of the device lifespan (year 5) and 300 mW after 55 years, respectively. From gamma radiation heating, the harvested energy can be up to 18 mW or less than 1 mW [79], which is far less than needed. Since the simulation results indicated that the energy harvested from the gamma heating is not enough to power the integrated system, the prototype and test attempts are not further conducted in this design.

Energy harvesting from thermal flow

In addition to the gamma radiation heating, the strong convective heat transfer process inside and outside the MPC creates a large temperature drop near the canister wall, making it ideal for thermoelectric energy harvesting. As shown in Figure 2.1, a large temperature drop between the helium and the canister inner wall can be ~70 K at year 5 and ~13 K at year 55. The thermoelectric generator is based on the concept of the Seebeck effect which can directly convert the temperature difference to electric voltage via thermocouples. In this project, a thermoelectric energy harvester, as shown in Figure 2.2 (b), is developed and planted near the dry cask wall to convert the temperature gradient inside the canister into electricity. A copper heat sink was design, built and attached at the hot side of the Bi2Te3 TEGs to improve the convection performance. Four TEG1-1263-4.3 modules of size 3 × 3 × 0.4 cm^3 were attached to the back of the heat sink. A copper adaptor was mounted to the back of the TEGs to thermally attach them to the cooler canister wall. The dimensions are: the 8 × 8 cm fin array base was attached to the four TEGs, with fins of 2.5 cm height and 5 mm thickness, based on the fin optimization result. [71] The overall size of the TEG energy harvester was about 8 × 8 × 6 cm^3.

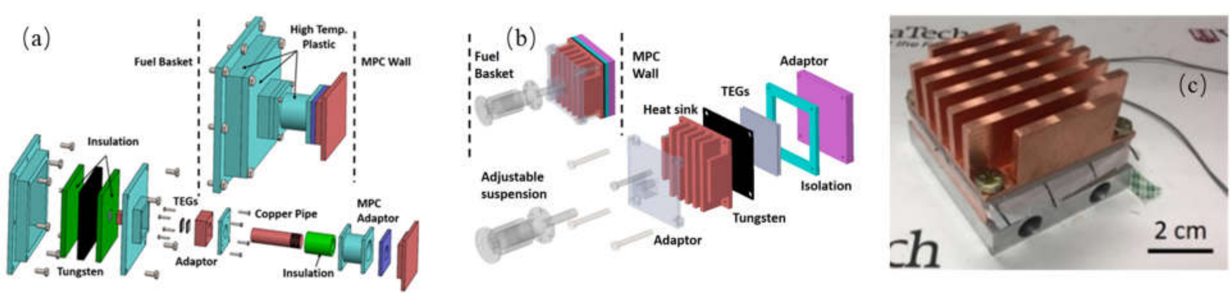

Figure 2.2. Design of the (a) gamma heating generator and (b) temperature gradient generator (TEG) and (c) the prototype of the temperature gradient energy harvester.

Based on the thermal and flow conditions obtained in our previous research [73], the fin array and the TEG placement were optimized to achieve the maximum power. [71] The voltage outputs of the harvester in the simulated year 5, 45, 50, and 55 cases were 2.8 V, 2.4 V, 2.2 V, and 2 V, and the corresponding maximum power outputs of the TEG energy harvester were around 94 mW, 67 mW, 56 mW, and 46 mW. The prototype of the harvester was developed as shown in Figure 2.2 (c) and tested in the lab by using a hydraulic oil circulation loop to simulate the real helium environment in the canister. [75] The results show that the maximum power output of the harvester was up to 60 mW, which is more than the needed power of 10 mW. [71] Though the hydraulic oil was used instead of helium, their heat transfer property differences, thermal contact resistances in the canister assembly, the temperature dependency of thermal properties of all the materials, and the temperature difference changes due to temperature fluctuation during the experiment were considered to make the lab test appropriate to represent the real-world situation.

2.3.2 Energy harvesting circuits

Energy management circuits are designed to regulate the harvested energy for sensing and communication at large instant power in an intermediate manner. The management circuits are developed at three stages, i.e. the impedance matching stage for maximum power transfer, first boost stage for stepping up the voltage from low output voltage (>0.5V) to rated capacitor voltage (5V) for energy storage, and a second stage boost converter for stepping up the capacitor storage voltage to 12V, which is operation voltage of the piezoelectric ultrasonic transmitter and the JFET electronics (Figure 2.3). Microcontroller (MSP432, Texas Instrument) is programmed to control the entire circuit. Impedance matching circuit with maximum power point tracking [80] is to transfer the maximum power to the storage device. The best impedance for TEG is $R_{TEG} = \sqrt{1+ZT}$. In the target application, the data communication operates for 3 seconds every 10 minutes and then goes to sleep mode to save power. In order to efficiently boost the voltage, the topology of a two-stage boost converter is adapted. First stage of converter (LTC3429, Analog Devices) charges the super capacitor with low voltage up to 5V, and second stage (LM1615, Texas Instruments) enable the boost regulator (12V) for 3 seconds when it is needed (10 mins sleep and 3 seconds active).

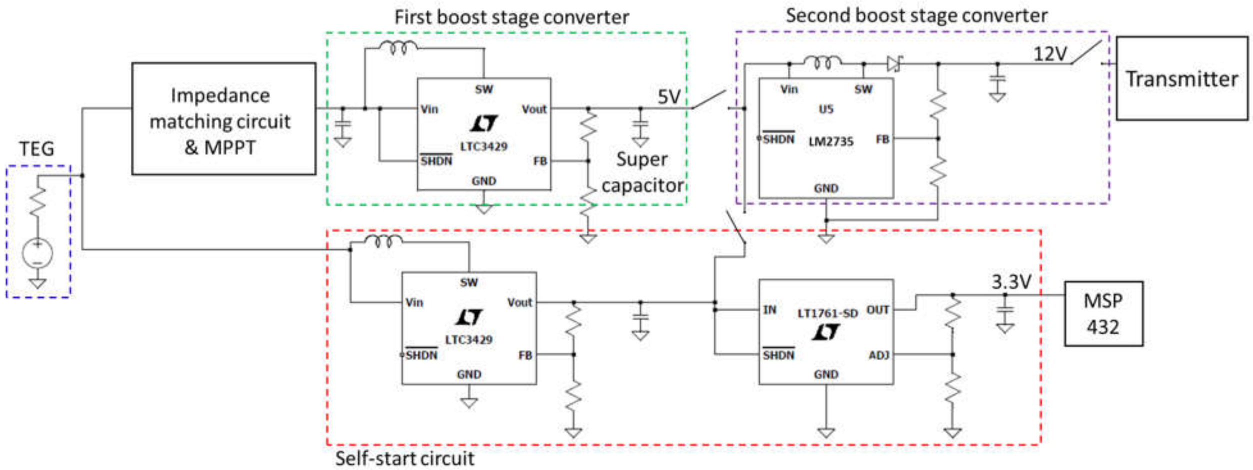

Figure 2.3. The schematic of the proposed power management circuit

It requires 3.3V power supply, which is higher than the output voltage of the TEG. To supply voltage for MSP432 using the TEG output voltage, a self-start circuit with a boost stage (LTC3429, Analog devices) that increases the voltage from (>0.5V) to 3.3 V is used. After the voltage of the super capacitor exceeds 3.3V, MSP432 sends a low signal to the self-start circuit to shut down the self-start circuit, and then the super capacitor directly supplies the power to the MSP432. A low dropout regulator (LT1761) is used for stable voltage supply to MSP432.

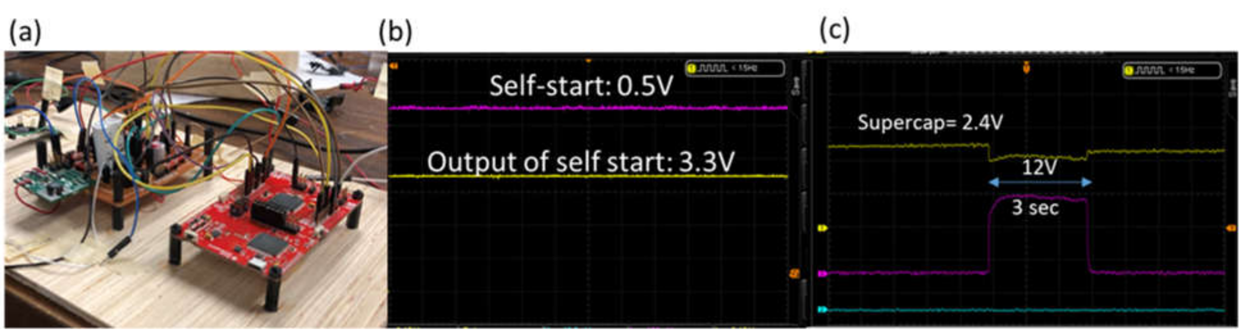

Figure 2.4. (a) The picture of the built circuit, and the experimental results of (b) the self-start circuit and (c) first and second stage power converter.

The circuit was implemented (Figure 2.4(a)), in the test, as TEG generates 0.5V, the self-start circuit increases the voltage to 3.3V for powering the MSP432 (Figure 2.4(b)). The top graph in purple is the output of the first stage boost converter, and the bottom one in yellow is the output voltage of the second stage of the boost converter (Figure 2.4(c)). After sleep mode for 10 mins, MSP432 sends the signal to the second stage converter for activating the second stage, and then it powers the piezoelectric transmitter for 3 seconds. Experimental results show that the proposed power management circuit successfully supplies 12 V voltage for the data transmission using low output voltage of the TEG.

2.4 Ultrasound Through-wall Data Communications

(credited to Prof Haifeng Zhang's group at University of South Texas)

2.4.1 Modelling of the ultrasonic data communication system

As a first step of the design of the ultrasonic data communication system, theoretical modelling of a transducer-steel plate-transducer structure has been performed. Figure 2.5 shows the simplified model including one driving piezoelectric transducer and one output piezoelectric transducer attached on the other side of the plate. 2h0, h1, h2 denote the thickness of the elastic plate, top (driving) transducer, and bottom (output) transducer, respectively, while P and ZL are the poling direction and load impedance of the piezoelectric transducer, respectively.

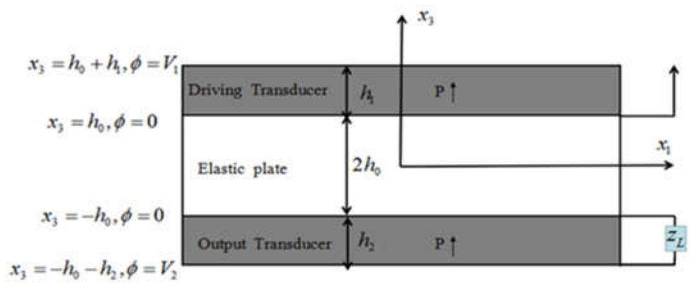

Figure 2.5. Schematic diagram of the ultrasonic through-wall communication system

For the piezoelectric transducers, it was assumed that the poling direction was along the plate thickness direction, and the transducers were operated in thickness-extensional modes (3-3 mode). For one-dimensional motion, the relevant stress component T_{33} and the electric displacement component D_{33} are given by the constitutive equations of piezoelectric materials as follows,

$$T_{33} = c_{33}u_{33} + e_{33}\varphi_{,3}$$

$$D_{33} = e_{33}u_{33} - \varepsilon_{33}\varphi_{,3}$$

(2.1)

where c_{33}, e_{33}, and ε_{33} are elastic constant, piezoelectric constant, and dielectric constant of the piezoelectric material in x_3x_3 direction, respectively, while u_3 and ϕ are mechanical displacement and electrical potential of the piezoelectric material, which could be derived via free and forced vibration analysis by applying appropriate boundary conditions and continuity conditions to Eq. (2.1).

The traction-free boundary conditions at the top surface of the driving transducer and the bottom surface of the output transducer are:

$$T_{33} = 0 \text{ at } x = h_0 + h_1 \tag{2.2}$$

$$T_{33} = 0 \text{ at } x = -h_0 - h_2 \tag{2.3}$$

while the electric boundary conditions at the top and bottom surfaces are:

$$\varphi = V_1 \text{ at } x = h_0 + h_1 \tag{2.4}$$

$$\varphi = V_2 \text{ at } x = -h_0 - h_2 \tag{2.5}$$

where V_1 is the applied voltage, V_2 is the output voltage.

On the two transducer-elastic shell interfaces, it requires a continuity of the mechanical displacement u_3 and the mechanical traction T_{33}, therefore the continuity conditions are given as follow,

$$\begin{gathered} u_3(h_0^+) = u_3(h_0^-) \\ u_3(-h_0^+) = u_3(-h_0^-) \\ T_{33}(h_0^+) = T_{33}(h_0^-) \\ T_{33}(-h_0^+) = T_{33}(-h_0^-) \end{gathered} \tag{2.6}$$

Similarly, the interfaces are considered as grounded, therefore, the electric potential at the interfaces are given as:

$$\varphi(h_0) = 0, \varphi(-h_0) = 0 \tag{2.7}$$

Free and forced vibration analysis results in the expression of the mechanical displacement u_3 and electrical potential φ, which are given as follows,

$$u_3(x_3) = A_1 \cos \eta x_3 + B_1 \sin \eta x_3,$$

$$\varphi(x_3) = \frac{e_{33}}{\varepsilon_{33}} u_3 + F_1 x_3 + G_1,$$

$$h_0 \le x_3 \le h_0 + h_1 \text{(Top layer: driving transducer)},$$

(2.8)

$$u_3(x_3) = A_2 \cos \eta' x_3 + B_2 \sin \eta' x_3,$$

$$-h_0 \le x_3 \le h_0 \text{ (Middle layer: elastic shell)},$$

(2.9)

$$u_3(x_3) = A_3 \cos \eta x_3 + B_3 \sin \eta x_3,$$

$$\varphi(x_3) = \frac{e_{33}}{\varepsilon_{33}} u_3 + F_3 x_3 + G_3,$$

$$-h_0 - h_2 \le x_3 \le -h_0 \text{ (Bottom layer: output transducer)},$$

(2.10)

where $\eta = (\rho\omega^2/\bar{c}_{33})^{1/2}, \eta' = (\rho'\omega^2/c'_{33})^{1/2}$ and $\bar{c}_{33} = c_{33} + \frac{e_{33}^2}{\varepsilon_{33}}$are the wave number of the piezoelectric material, wave number of the steel plate, and effective elastic constant of piezoelectric material, respectively.

It should be noted that the output power strongly depends on the frequency of the driving voltage. Fig. 6 shows the calculated efficiency of a through-wall data communication system that is composed of PZ46 piezoelectric transducers and steel plate, where P_1, P_2, ω, and ω_0 denotes the input power, output power, driving frequency, and fundamental frequency, respectively, while Table 2 shows the material constants accordingly. From Fig.6, it can be seen that resonances can be found at the fundamental and the third overtone of the transducer, which indicates an distinctive signal-noise-ratio that is ideal for carrier wave propagation for through-wall data communication purpose.

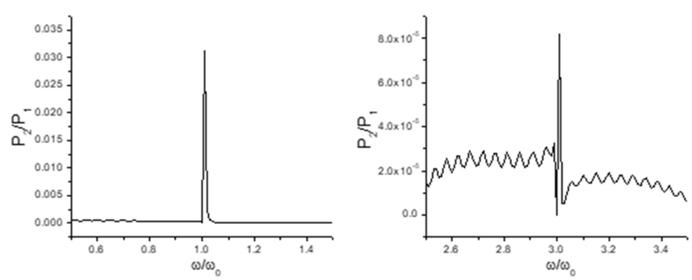

Figure 2.6. The efficiency of the communication system as a function of the driving frequency.

Table 2.2. Material constants for the through-wall data communication system.

Material	c_{33} / GPa	e_{33} / 2.65C/m^2	ε_{33} / C/(V·m)	ρ / kg/m^3	*Thickness* / mm
PZ46	103	2.65	1.098	6530	2
Steel	109.2	-	-	7860	10

The fundamental frequency of the transducer (standalone) is given by $\omega_0 = \frac{\pi V_L}{h_1} = 3.0616 \times 10^6$ rad/s, or $f_0 = \frac{\omega_0}{2\pi} = 0.487$ MHz, where $V_L = \sqrt{\frac{\bar{c}_{33}}{\rho}} = 4093$ m/s. Consequently, the third overtone f_1 is determined as f_1=3f_0=1.461MHz.

2.4.2 Data transmission at room temperature

Ultrasonic data transmission has been widely studied in literature. [64, 65, 68] However, the research demonstrated is for simple binary data transmission. In this work, for the first time, both text and image data were transmitted through the wall with distinctive qualities. Fig. 7 shows the schematic of the ultrasonic data transmission system. The text/images data will be first converted to data file (*.dat), which will be further converted to binary data and transmitted through the wall via modulation and demodulation process. The transmitted data will then be recovered to the text/images and finally displayed in a computer. Fig. 8 shows the experiment setup, which includes two piezoelectric transducers that are bonded coaxially on each side of a metal wall. The text data generated from the computer is converted into serial binary data by utilizing Arduino Uno board. The baud rate used for this data communication is 1200 bits per second with a possibility to be maximized up to 9600. The serial binary data from the Arduino is then supplied as modulating signal to an Amplitude Modulator (AM) circuit with a fixed carrier frequency of 126.08 kHz. Afterwards, the modulated signal with binary data is fed to the transmitter piezo ceramic. The transmitter piezo transmits binary signal from one end to the other end of the metal wall, which is received by the receiver piezo ceramic. The received signal is supplied to demodulator circuit and then fed to the Arduino receiver, which helps display the received text in a computer. The experimental output of signals at each phase are shown in Fig. 9, including the digital data, received data with amplitude modulation, demodulated signal and the decoded signal.

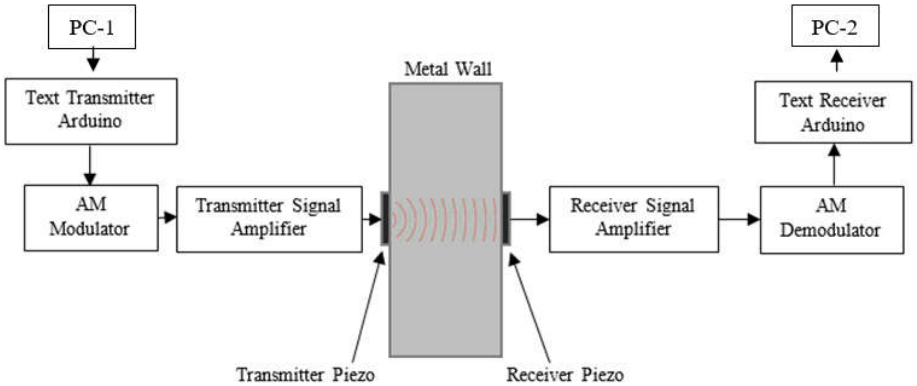

Figure 2.7. Schematic diagram of the ultrasonic data transmission system

E

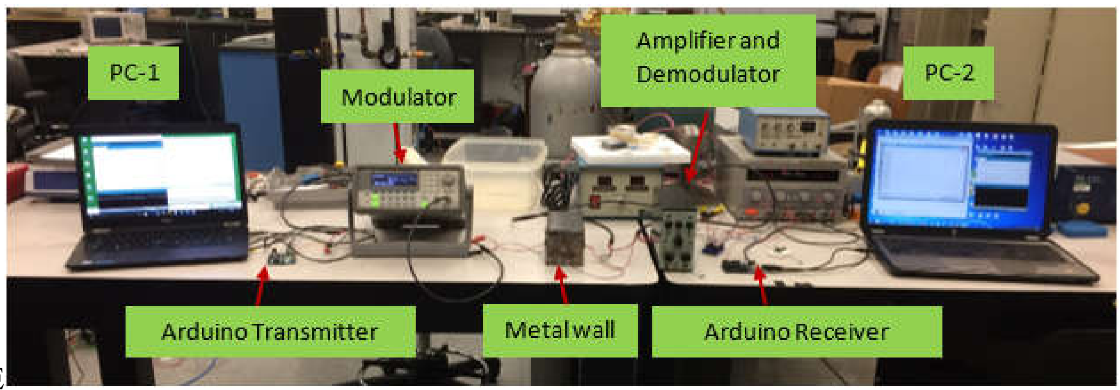

Figure 2.8. Photograph of experimental setup

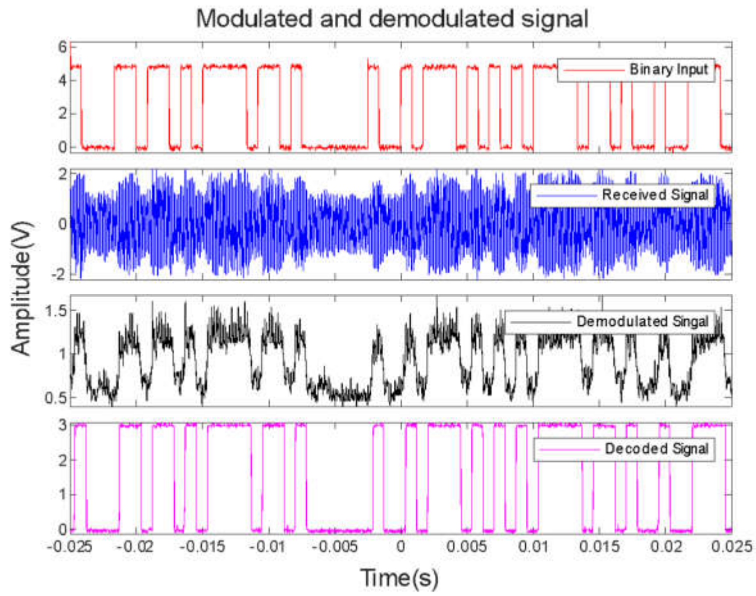

Figure 2.9. Modulated and demodulated signal

2.4.3 Data transmission at elevated temperature

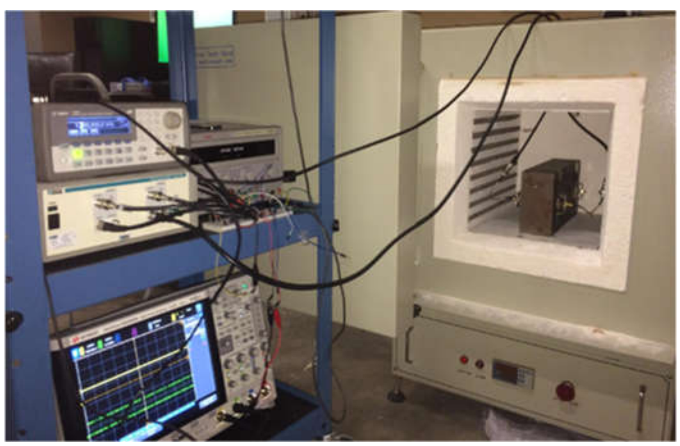

Figure 2.10. Ultrasonic data communication system inside a high temperature furnace.

To ensure that the ultrasonic data communication system will survive in the high temperature canister environment, the piezoelectric transducer TRS BT200 is selected in this study, which could operate in a temperature up to 350° C. The transducers are attached onto both sides of a half inch stainless steel plate using high temperature ceramic adhesive. The stainless steel plate with the transducers are then placed inside a high temperature furnace (Fig. 10). The associated electronics including modulator and demodulator are placed outside of the furnace. Experiments are performed at different temperatures from room temperature to 250° C. By increasing the operating temperature, the received signals experienced a significant attenuation, leading to an underrepresented data communication cycle.

2.5 Temperature and Radiation Hardened Electronics for In-Cask Sensor Interfacing and Communications

(credited to Dr. Nance Ericson's group at Oak Ridge National Lab)

To withstand the harsh environmental conditions associated with in-cask monitoring, an analog-based electronics approach was chosen with primary emphasis on simplicity (i.e., fewer active devices), minimizing energy consumption, and maximizing signal to noise ratio (SNR). The electronics topology chosen is shown in Fig. 11 for sensor frequency modulation. Two independent frequency modulated sensors, each for a different measurement of interest (temperature or pressure), are summed then mixed with a reference carrier frequency. This resultant signal is then filtered, amplified, and used to drive the piezo transducer for data communication to the outside of the cask. Straightforward detection can be performed on the exterior to isolate the two sensor signals of interest. This topology requires few active devices and operates entirely in the analog domain.

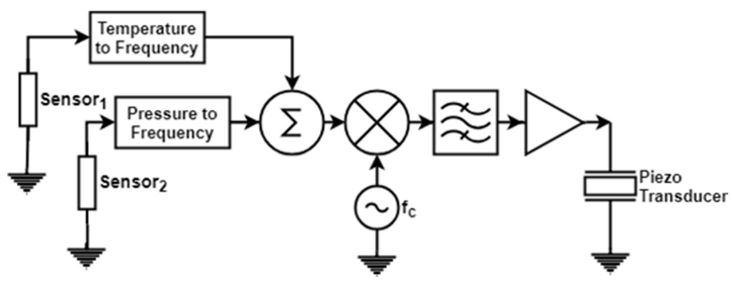

Figure 2.11. Simplified electronics system for in-cask monitoring of temperature and pressure.

The principal building blocks of this topology include three oscillator circuits (two sensors and a local oscillator), a summing circuit, a mixer, and an acoustic transducer driver. One oscillator, referred to as the local oscillator (LO), generates the carrier frequency while the other two oscillators output a frequency which is proportional to the associated sensor resistance or capacitance. The mixer modulates the summed sensor outputs to the resonant frequency of the acoustic transducer for more efficient transmission. An acoustic driver is used to amplify the signal from the mixer stage for transmission. The LO was implemented as a Colpitts oscillator for its high efficiency, while the sensor oscillators are RC phase oscillators, discussed later. A single-ended Gilbert Cell was chosen as the mixer. Finally, the acoustic transducer driver for the BT200 piezoelectric transducer is a common emitter topology amplifier.

2.5.1 Sensor-based Oscillator Circuits

To increase signal fidelity, the sensor data was chosen to be proportional to a frequency shift by using an RC oscillator (Fig 12a). The frequency output, f_{sensor}, of the oscillator is determined by Equation 14. This equation assumes that the feedback resistors R_1, R_2, and R_3 are equal ($R_1 = R_2 = R_3$) and denoted as R. Similarly, the feedback capacitors C_1, C_2, and C_3 are assumed to be equivalent

($C_1 = C_2 = C_3$) and denoted as C. To perform a temperature measurement, R_1, R_2, and R_3 would each be replaced by an identically valued thermistor. As the temperature changes the frequency would vary. Similarly, appropriate pressure sensors would replace capacitors C_1, C_2, and C_3 such that the change of capacitance would create a variation in frequency.

$$f_{sensor} = \frac{1}{2\pi RC\sqrt{6}} \tag{2.11}$$

The sensors were simulated using LTSPICE using BJTs where values of the feedback resistors R_1, R_2, and R_3 changed from 10 kΩ to 12 kΩ while the capacitors C_1, C_2, and C_3 remained constant with a value of 1 nF (Fig 12b). The other circuit parameters are $R_4 = 400 k\Omega$, $R_5 = 700\ k\Omega$, $R_6 = 2\ k\Omega$, $R_7 = 600\ k\Omega$, $C_4 = 1\ \mu F$, and $C_5 = 100\ \mu F$. The voltage sourced was 12 VDC, and the transistor Q1 was simulated as a 2N2222. The frequency governed by the resistors was shown to be about 6.66 kHz for the 10 kΩ resistor and 5.82 kHz for the 12 kΩ resistor. Both frequencies are within 10% of the theoretical estimate.

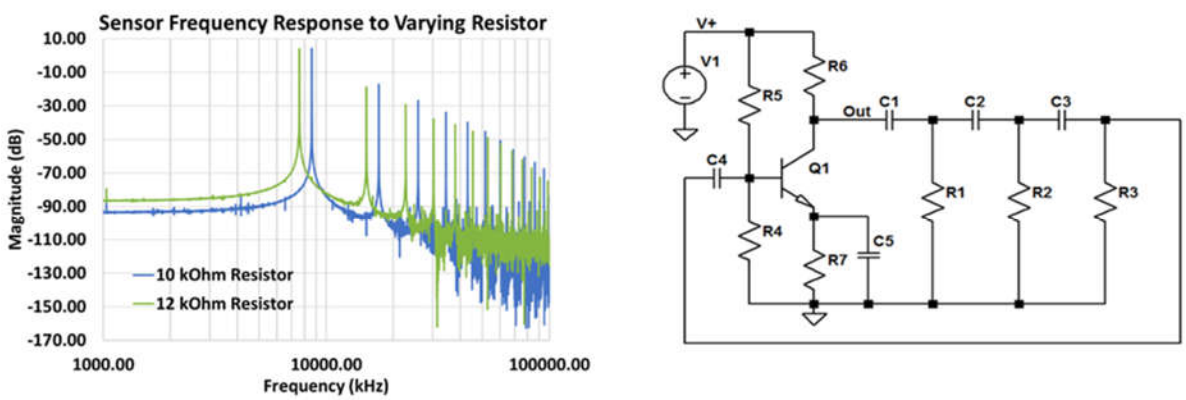

(a) (b)

Figure 2.12. (a) The SPICE simulation of the output FFT using 10 kΩ (blue) and 12 kΩ (green) sense resistors from (b) the corresponding sensor oscillator circuit based on an RC phase oscillator.

2.5.2 Modulation Circuit

To ensure a suitable implementation with few active devices, double-side band amplitude modulation (AM) was chosen. Although, large carrier AM topology would feature fewer components, the inefficiency of the power consumed by the carrier would be difficult to maintain towards the end-of-life power budget of the system. Thus, a suppressed carrier AM was designed using a single-ended Gilbert cell featuring bipolar junction transistors (BJTs). This cell modulated the LO with the summed sensor signals. Verification of this mixer cell was performed in LTSPICE.

From this simulation it was observed that the open load spectrum had 25 dB of carrier attenuation, and the harmonic content was attenuated by at least 20 dB.

2.5.3 Piezoelectric Modeling

The TRS BT200 high temperature piezoelectric transducer was identified to be the most viable candidate for through-wall transmission. To verify the circuit an appropriate circuit model of the transducer was first established by the easy model (Kim et al 2008). The impedance characteristics were measured from a Keysight E4990A impedance analyzer. Then, the transducer was modeled to the fifth harmonic for accuracy (Fig. 13). Here R0 and C0 represent the high frequency and low frequency impedance characteristics, while a parallel combination of a resistor, capacitor, and inductor form the resonant nature of the transducer. Since the piezoelectric transducer features only odd harmonics, only three resonances were incorporated. Figure 14 shows the comparison of the modeled and measured fundamental resonance. Both the magnitude and phase of the simulations match, but a few other thickness resonant modes are found below 700 kHz.

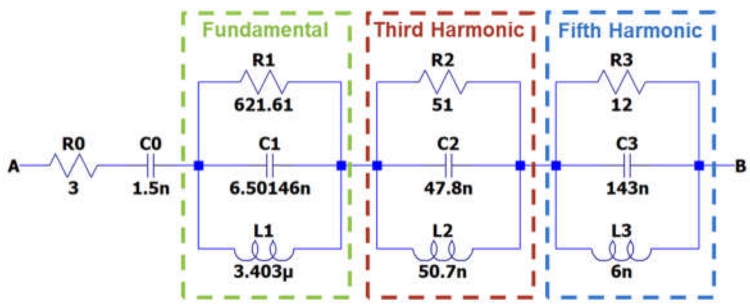

Figure 2.13. Circuit model of a piezoelectric transducer. The transducer is modeled to the fifth harmonic and has a fundamental resonance at about 1.07 MHz.

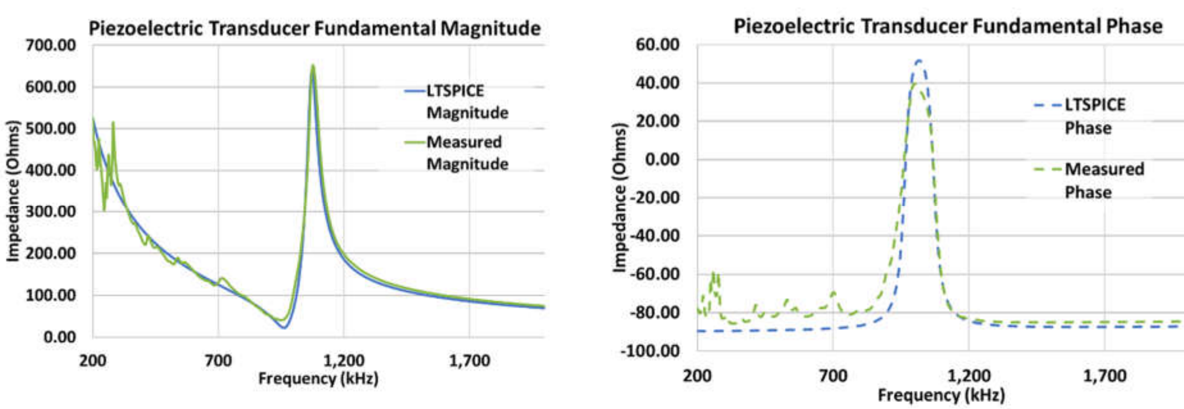

Figure 2.14. Comparison of the measured (green) and simulated (blue) BT200 impedance magnitude and phase.

2.5.4 Transitioning to JFET

JFET-based electronics are inherently more resistant to ionizing radiation due to the absence of the gate oxide and up to 55 Mrad of ionizing radiation has been demonstrated in literature. [81] However, the JFET fabrication process yields large transconductance variance between similar devices. These mismatches lead to increased carrier leakage and power loss. To decrease prototype design time, BJT circuits were first constructed to study the circuit topology. Once the circuit topology was simulated and tested successfully, the electronic design was transitioned into a JFET-based approach.

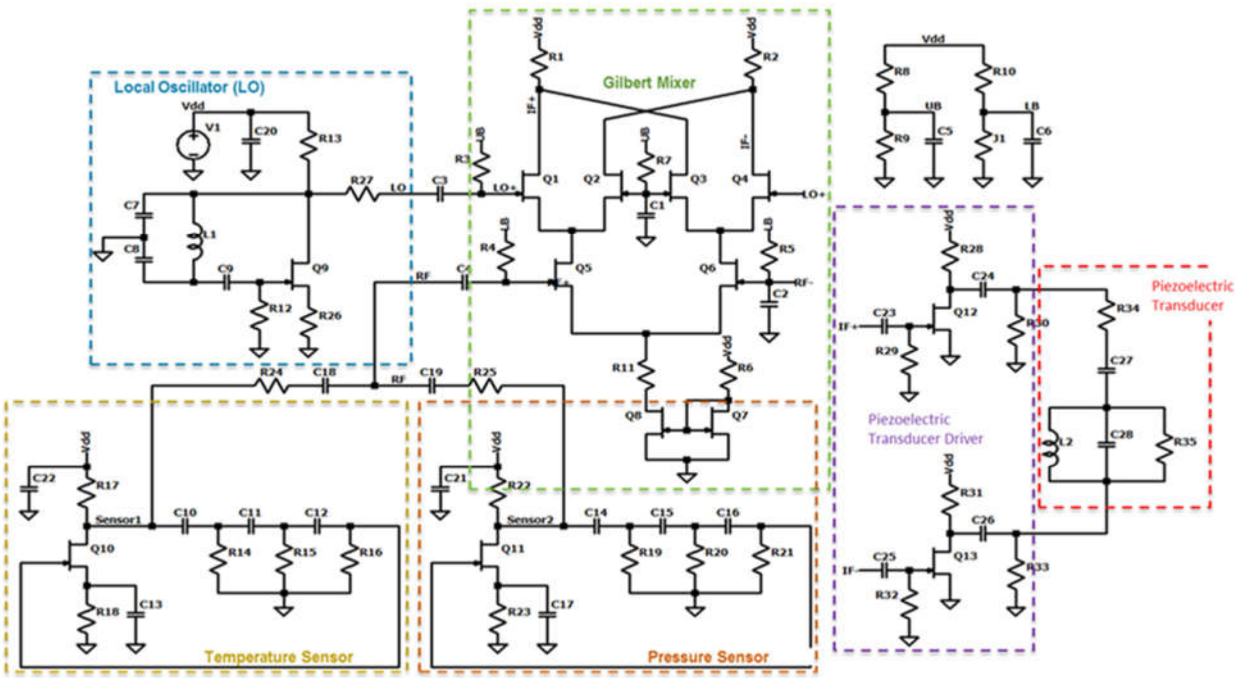

Figure 2.15. The JFET-Based Electronics system schematic.

After simulation and fabrication, the JFET prototype was tested in a laboratory environment using a pair of piezoelectric transducers coupled across a 1-inch thick steel plate (see Fig. 16). Powered by a commercial DC power supply at 12 VDC, the circuit was connected to one piezoelectric serving as the transmitter while the piezoelectric receiver attached to the opposite side of the steel plate was connected to an oscilloscope. The transmitted and received waveforms were captured by the oscilloscope and the fast Fourier transform (FFT) of both signals were computed and displayed (see Fig. 17). The received signal suffered a 16 dB attenuation loss, due to losses associated with transmission through the steel plate. The power consumption of the transmitting electronics circuits was 540 mW. Power consumption could be decreased by better matching the piezoelectric transducers to the on-board amplifiers, and by more effectively tuning the oscillators and their respective gains which were optimized to drive 50 ft of coaxial cable, as needed for the radiation experiments.

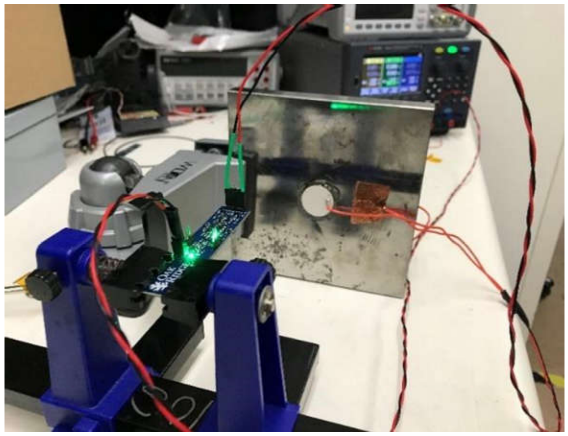

Figure 2.16. Two views of the JFET board transmitting a signal through a 1-inch steel block using piezoelectric s as the signal transmission and receiving transducers.

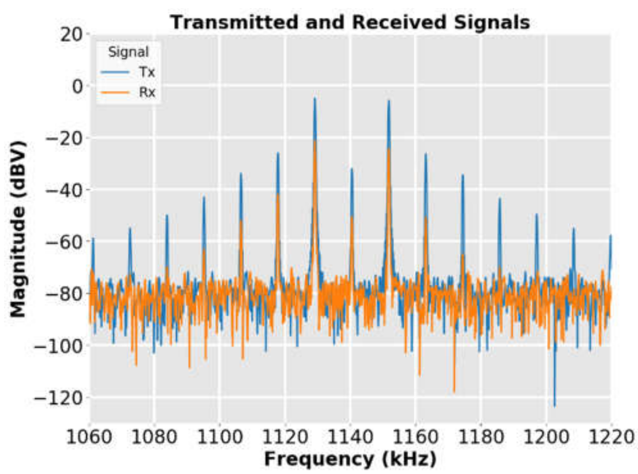

Figure 2.17. Measured spectrum of the piezoelectric signals generated by the revised JFET prototype PCB (transmitted) and the piezoelectric received signal.

2.6 Radiation Testing and Shielding

Spent nuclear fuel is still a strong radiation source, though not strong enough to power the plant. The electronics and ultrasound wireless modules need adequate radiation shielding to expand the device lifetime and reduce signal interference. The major radiation types of the it are gamma radiation and neutron radiation. With the shortest wavelength as an electromagnetic wave and its penetrating nature, gamma radiation requires a large amount of shielding mass to reduce to a safe level. Materials with high atomic numbers and high density are found to perform best against gamma rays. Quantitatively, the shielding performance is positively related to the total area density. Lead is well used as the shielding material for gamma radiation shielding as a result of its high density, high atomic number, and, obviously, low expense. Compared to the conventional ionizing radiation based on photons or charged particles, neutrons are repeatedly bounced and slowed (absorbed) by light nuclei. With a large number of water molecules chemically attached, the concrete provides a cheap solution due to its combined shielding ability of both neutron and gamma rays.

2.6.1 Radiation test setup

The built devices were sent to the Westinghouse Company for a gamma radiation exposure test to guide the radiation shielding design and the feasibility of the modules in the nuclear environment, as illustrated in Fig. 18.

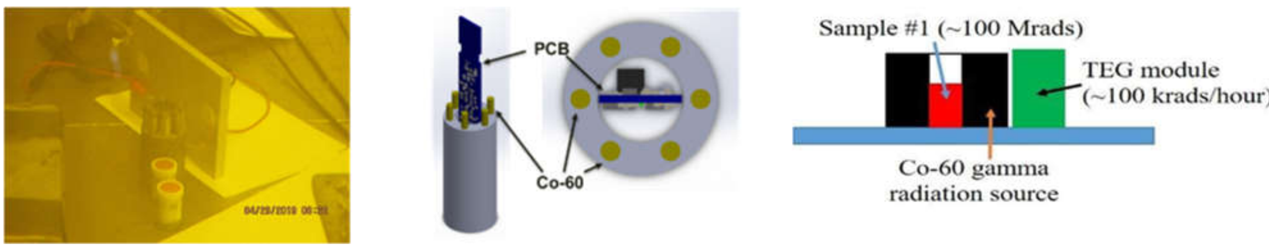

Figure 2.18. Thermoelectric material radiation test setup: View of irradiation setup through shielding glass (left), PCB and Co-60 physical configuration (center), and side view showing TEG placement (right).

2.6.2 Radiation test of thermoelectric materials and generator

The thermoelectric materials used for the TEG energy harvester were a Bi_2Te_3 sample from TECTEG and a Bi_2Te_3 based TEG module (TEG2-126LDT from TECTEG, 8×8×8 cm^3) which need to be tested under radiation condition. A cylindrical Co-60 gamma radiation source with a diameter of 50 mm was placed on a lifting jack plate in the experiment.

Small PCB samples and TE materials were put in the center of Co radiation sources and were subjected to highest dosing rate 300-400 krad/hr (measured 369 krad/h), while a TEG module was put as close as possible to the gamma sources but outside of the source center, with a dosing rate of 100 krad/hour. The TEG module was heated periodically by a 1.5-inch 200W cartridge heater controlled by a heat controller. The open-circuit voltage of the TEG modules and the temperatures of the source and the ambient environment were measured and recorded every 10 seconds. The source temperature was controlled to oscillate between ~25 °C and ~ 60 °C to work as the input energy for the thermoelectric generator. [79]

The temperature profiles for the gamma radiation test and the no-radiation control group were plotted in Fig. 19 (a). The slight difference between the two cases is because the device mass was small and the temperature controller had limited accuracy. The open circuit voltage output of the TEG module is presented in Fig. 19 (b), which varied between 0.1 V and 1.2 V accordingly with the source temperature. There was no significant voltage output difference between the two tests. This implies that the impact of the gamma radiation on the simultaneous performance of the TEG module was minimal.

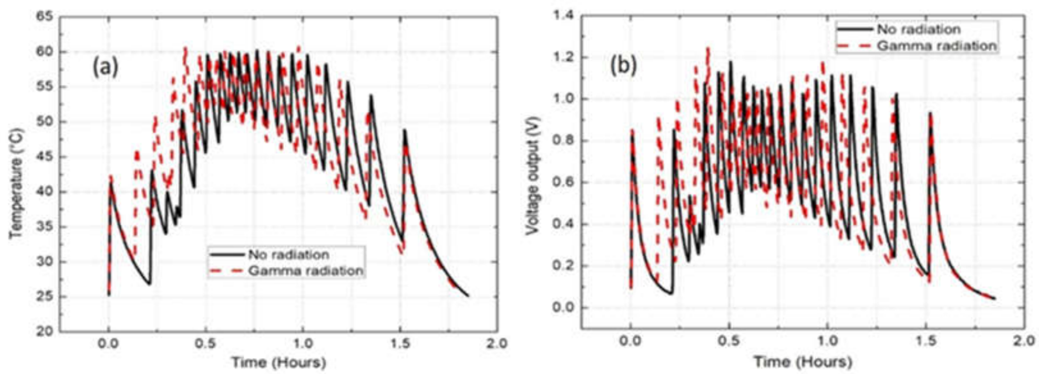

Figure 2.19. (a) Temperature profile of the heating source; (b) The open circuit voltage output of the TEG module. [79]

Besides the transient effect of the gamma radiation on the TEG, the influence of the accumulated gamma radiation dose on the Bi_2Te_3 material was also examined. The Seebeck coefficient, electrical conductivity, and thermal conductivity of material sample before and after the gamma radiation test were characterized and compared, and the results are shown in Fig. 20 (a), (b), and (c), respectively. The results show no significant difference before and after the radiation exposure test, considering the characterization error of the instruments. This indicates that the gamma radiation impact on the bismuth telluride material was minimal.

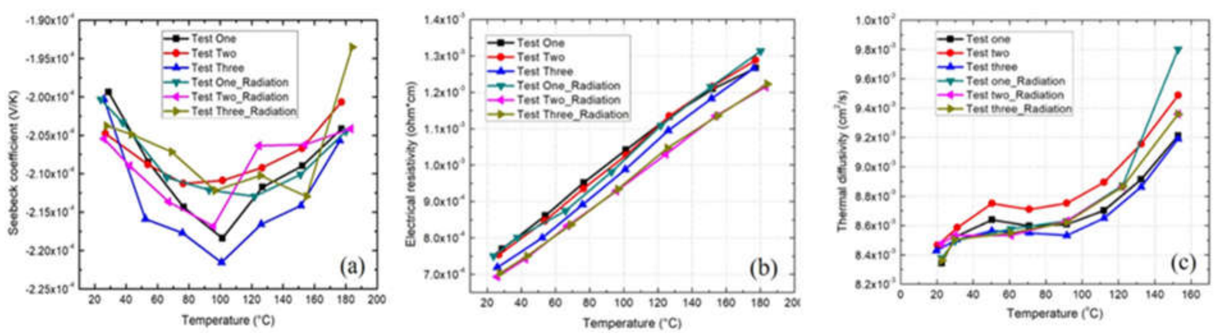

Figure 2.20. The comparison of (a) Seebeck coefficient, (b) electrical resistivity, and (c) thermal diffusivity of the Bi2Te3 sample before and after gamma radiation. [79]

2.6.3 Radiation test of the ultrasonic data communication system

To investigate the influence of nuclear radiation on the ultrasonic data transmission system, the ultrasonic data communication system was also sent to Westinghouse Company's radiation hot cell test facility. The total of 101 Mrad Gamma radiation has been applied to the TRS BT200 piezoelectric transmitter and receiver attached on an aluminum plate. The dosing rate is about 150 kRads/hour, closer to the radiation source than the TEG modules. The transmitter and receiver were exposed to the radiation source and the recorded binary data transmission in the three different days are plotted in Fig. 21. From Fig.21, it can be seen that the system successfully maintained the power level of the recovered binary data after nuclear radiation, indicating that the material as well as the data transmission have not been subjected to significant degradation over time. The system is still able to transmit and recover the data through the wall after strong Gamma radiation exposure.

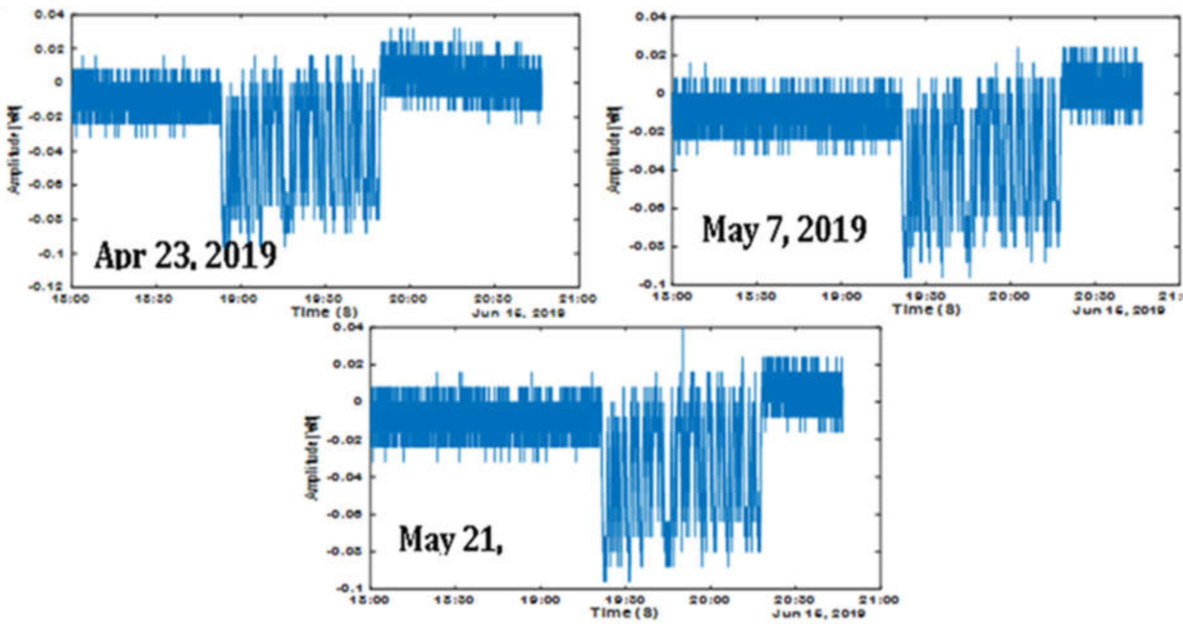

Figure 2.21. The radiation test results of ultrasonic data communication system over four weeks of Gamma radiation test: on Day 0, Day 21, and Day 28.

2.6.4 Radiation test of electronics:

Determining the total radiation dose that each circuit can tolerate without failure is critical. As such, the initial 2 Mrad (Si) gamma irradiation testing at Westinghouse (Pittsburgh, PA) on the JFET-based circuis was performed simultaneously. [82] Two printed circuit boards were placed in the hot cell at a given time with a dose rate of about 15 kRads/hr and were irradiate during operation to a total of 2 Mads. These two boards were each monitored by oscilloscopes set to acquire 1 megasamples per capture on each channel with a sampling rate of 10 MHz. During the test, each oscilloscope measured an independent board.

The data from each capture were saved with the corresponding timestamp. The data was analyzed by first implementing an fast Fourier transform (FFT) on each data set. [83] From the FFT of each capture, the frequency and magnitude of each signal-of-interest was recorded using a peak detection algorithm. An estimation of the mixer local oscillator frequency and sensor frequency was also recorded from the mixer FFT. The frequency with respect to dose was plotted for the JFET sensor (Fig. 22a) and RF band signals (Fig. 22b). The magnitudes of the signals were plotted with respect to dose for the oscillators (Fig. 22c) and for the mixer (Fig. 22d).

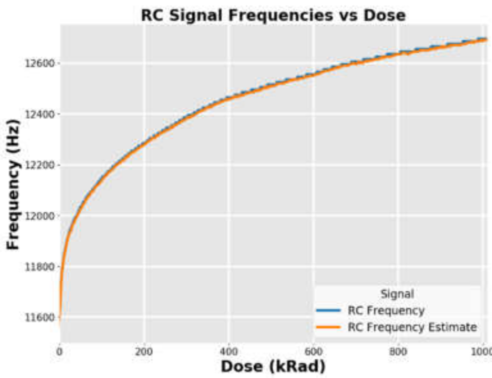

(a) Measured and estimated RC sensor frequencies with respect to dose.

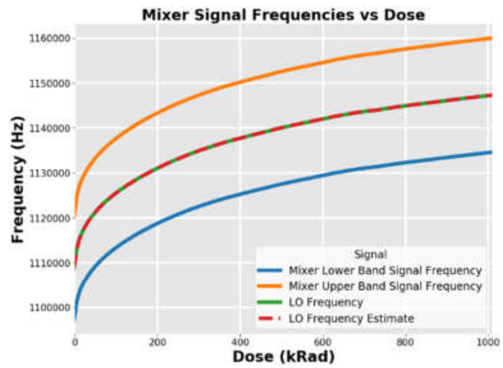

(b) Measured and estimated Mixer and LO signals with respect to dose.

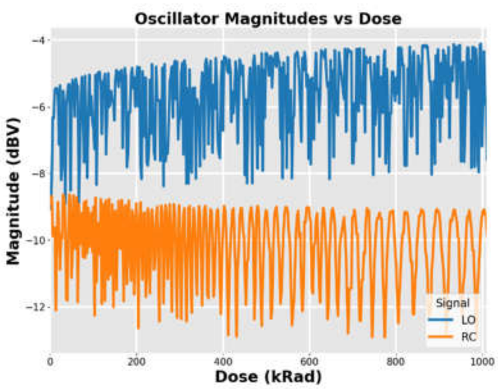

(c) Measured oscillator fundamental frequency magnitudes with respect to dose.

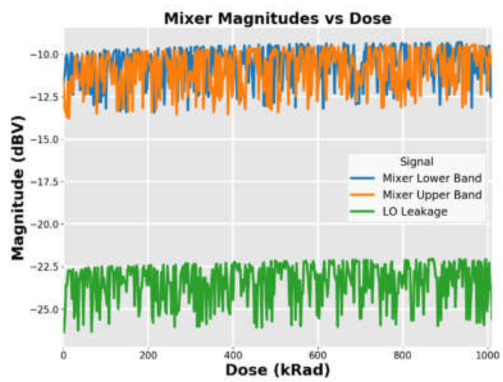

(d) Measured magnitudes of the Gilbert mixer signals of interest.

Figure 2.22. The radiation test results of JFET electronics [82]

The results from the irradiation tests are promising; but with a dose rate of approximately 15 krad/hr, the PCB electronics would require over 6,000 hours (0.75 years) to reach the target dose of 100 Mrad. Increasing the dose rate on the existing boards by moving them closer to the source, would decrease the uniformity of the radiation dose across the board, due to the large width of the board as compared to the smaller diameter of the radiation source. Alternatively, by placing the PCB in the center of the radiation source, a dose rate of ~500 krad/hr can be obtained. Thus, the circuit boards were redesigned (Fig. 23) to increase the radiation dose rate while maintaining the uniformity of the dose by enabling placement inside the source, as depicted in Figure 19 (middle). This 2nd revision of the JFET PCBs removed some extra circuits present in the previous design and featured only a single sensor-controlled oscillator.

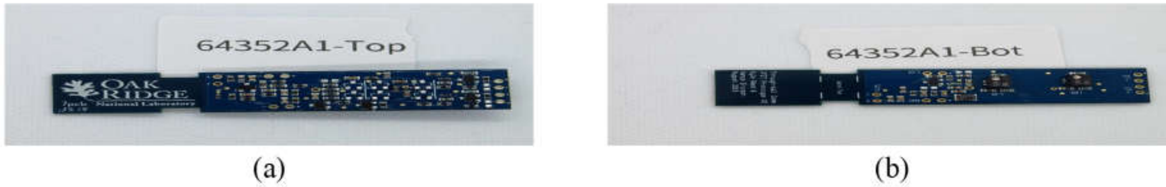

Figure 2.23. Design of the JFET electronics: Top (a) and bottom (b) of the revised JFET PCB.

2.6.5 Radiation shielding

To shield both the neutron and gamma radiation the tungsten boron carbide (W-B4C) was chosen because of its effectiveness and compactness for both gamma-ray and neutron radiation shielding. The neutron flux in the cask was seven orders smaller than the gamma radiation. Though the neutron has higher average particle energy (~2.2 MeV), the accumulated neutron radiation dose bypassing the shielding materials was still six orders less than the gamma radiation. Therefore, the neutron radiation was considered minor in this case. Therefore, the mass fraction of the composite was chosen as W: 77%, B-10: 4%, B-11: 14%, and C: 5%, respectively and the result density of the composite is 15.34 g/cm^3. [79]

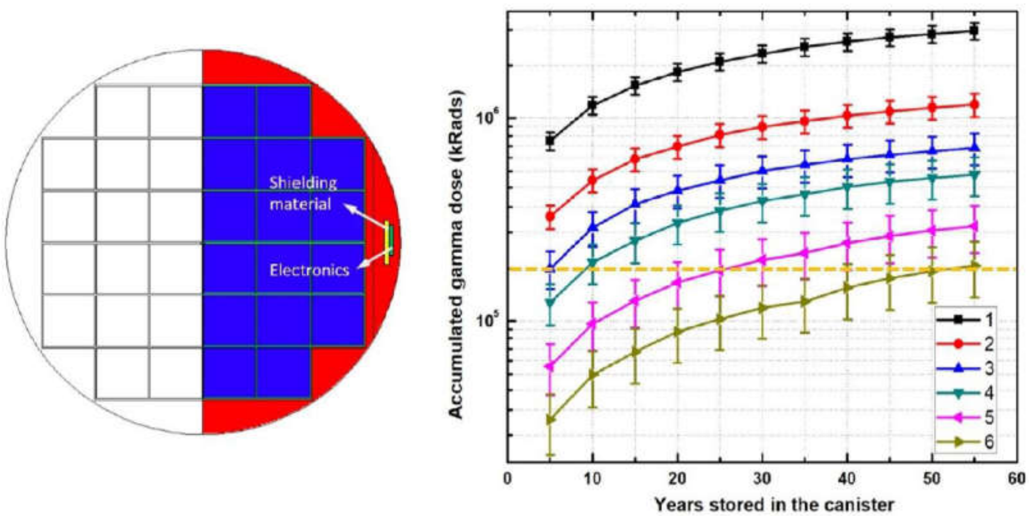

Figure 2.24. The radiation shielding (left) and accumulated gamma dose in the electronics vs time at different tungsten thickness 1-6 cm.

The radiation source values for the MCNP6 simulation mentioned in Section 2 were obtained from the SCALE calculation. The shielding box with a footprint 200 mm x 200 mm is designed and placed on the inner surface of the dry cask, as shown in Fig. 24 (left). The electronics are fixed inside the shielding box and also attached to the vessel wall and the radiation is assumed from one side the shielding box. Fig. 24 (right) shows that accumulated gamma dose at different tungsten thickness. As references, commercial Si-BJT electronics we tested in Westinghouse hot cell failed at gamma radiation dose was 94.4 kRads [84], and Si-JFET electronics survived after 2 MRads in our test and 55 MRads in literature. [81] According to the results in Fig. 24, the Si-BJT electronics, even with 60mm tungsten shielding, will fail after 20 years of canister service. W-B4C (77% W) shielding of 25mm can protect the gamma radiation of electronics at threshold 1.1 MRads. If Si-JFET electronics can tolerate 100 M Rad radiation, we only need W-B4C shielding of less than 1mm thickness.

2.6.6 Thermal protection design

Known from the simulation mentioned above [73], the environmental temperature is also a challenge to the electronics. For the year 5 case, the helium gas temperature near the canister wall was as high as 480 K, while the wall temperature was about 410 K. Thus, a temperature shielding layer and a temperature uniformization layer was also integrated. The whole structure was shown in Fig. 25. The thermal conductivity and thickness of each layer were presented in Table 3.

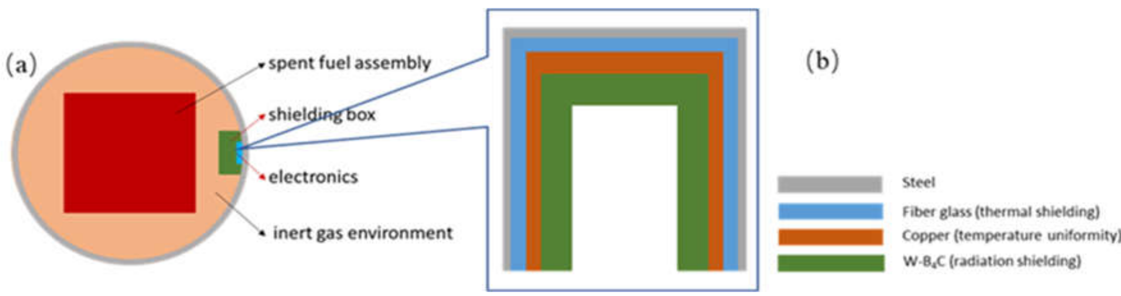

Figure 2.25. (a) The placement of the shielding box, size exaggerated and (b) the cross section of the shielding box.

Table 2.3. The thermal conductivity and thickness of each layer

Materials	**Thermal conductivity (W/(m*K))**	**Thickness (mm)**
Steel	50.2	2
Silica	1.4	5
Fiberglass	0.04	10
Copper	400	10
W-B4C	141.5 (Weight averaged)	25

A simulation [73] was carried out in the COMSOL and the inner surface temperature was found to be less than 423 K (150°C) for the year 5 case, as shown in Fig. 26. That temperature met the feasible margin for the temperature-hardened electronics.

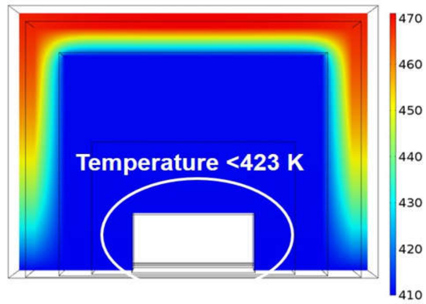

Figure 2.26. Temperature profile of the shielding box. [79]

2.7 Integration Test at High Temperature Environment

All the built modules of the entire self-powered monitoring and wireless data communication system were tested separately and then sent to the Center for Energy Harvesting Materials and Systems at Virginia Tech to conduct the integration test (Fig. 27). The different modules were connected by wires with high-temperature durable insulation. The system was first tested at the room temperature with a swaged 50 W cartridge heater (OMEGA Engineering) to simulate the thermal energy source for the TEG energy harvester.

To obtain the high-temperature environment, a Fisher ISOTEMP® Vacuum Oven Model 281 was used to provide and maintain a temperature up to 280 °C with approximately uniform temperature profile. Two cartridge heaters (OMEGA Engineering) were used to generate the temperature difference which was controlled by a temperature controller (CN7800, OMEGA Engineering) and the thermocouple temperature sensors to get the necessary temperature difference. A Keysight DSO1014A Oscilloscope was used to detect the input and output signal of the communication module.

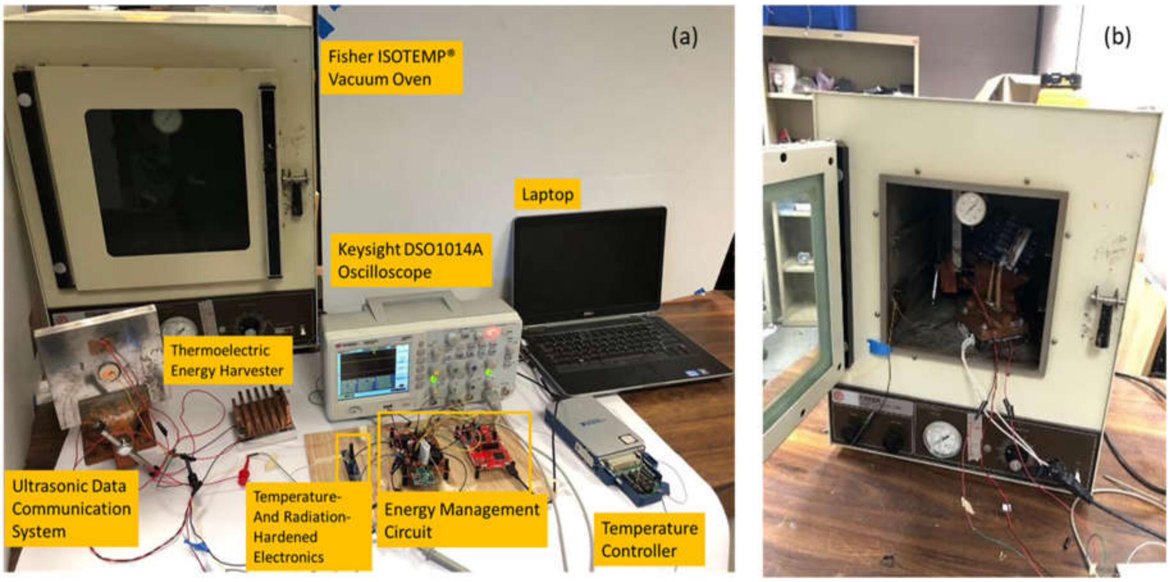

Figure 2.27. The experimental setup of the integrated self-powered monitoring and through-wall wireless data communication system in (a) room temperature and (b) high temperature.

The oscilloscope probes were connected to the input positive and output positive electrodes of the ultrasound wireless communication module. The input voltage signal was generated by the temperature and radiation-hardened PCB board. The whole system is powered only by the thermal energy harvester with the developed energy management electronics. All functioning modules of the system were integrated and placed in the vacuum oven after the oven was preheated to the targeted temperature. The tested temperature range was from 120 °C to 150 °C. At each selected temperature, the system was placed in the environment for more than one hour to examine whether there was accumulated damage. Then the functions of the system including energy harvesting, sensing data transmission, and power electronics were tested. Destructive test was finally conducted to determine the maximum temperature that the system could survive. In the destructive test, the temperature raised from 150 °C and remained 10 minutes every 5 °C until the system failed to output the signal.

The experimental results show that the system survived and worked properly at 120 °C, 130 °C, 140 °C, and 150 °C. For each of the one-hour tests, the oscilloscope readings were recorded at 20 minutes, 40 minutes, and 1 hour. The signal input and output comparisons are as below. Only 0.2 millisecond of the waves in the 3-second active phase of the work cycle is shown to clearly compare the input and output signals. The destructive test show that the system failed to send out a signal at 195 °C. The signals recorded before the system failure are all normal as in Figure 28.

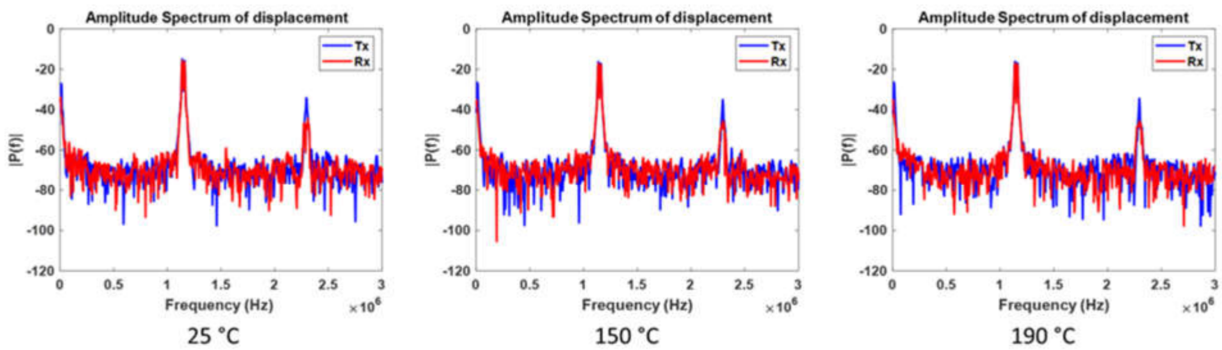

Figure 2.28. The input and output signal amplitude spectrum of displacement at increasing temperatures of 25 °C (room temperature), 150 °C (designated working temperature), and 190 °C (last successful transmission before failure).

When the system failed, the multimeter still had a valid voltage reading, which confirmed that the Thermoelectric energy harvesting module still worked. Nevertheless, the input reading of the oscilloscope remained zero and the indicator LED of the PCB board was out. After the modules were taken out and cooled down to the room temperature, the PCB board was tested again and gave no response. Therefore, the first component that failed to the increasing temperature was proved to be the PCB board. Another finding is the glue layer between the piezoelectric transducers and the metal wall was found to split off, indicating a failure of the ultrasound transmission.

During the whole process until the destructive test, no component was changed or replaced, which means the entire system could survive in a long-term duty under the environment of at least 190 °C as designated. In the Seebeck coefficient characterization, the thermoelectric materials worked properly at over 250 °C. Therefore, one could increase the system's temperature tolerance by further strengthening the electronic board.

2.8 Chapter Conclusion

A self-powered through-wall data communication system for monitoring inside conditions of spent nuclear fuel canisters is developed and experimentally demonstrated. The system is composed of energy harvesting, through-wall ultrasonic communication, power management, and sensing electronics. Two energy harvesters are designed to convert the thermal energy and gamma radiation inside the canister into usable electricity as a sustainable power supply for the sensing and data communication. Numerical results show that the power output of the radiation energy harvester is very low and therefore only TEG harvester was built and tested. Energy harvesting circuits were designed and built to manage the harvested irregular voltages. The high-temperature and radiation shielding was performed and experimentally validated to protect the power electronics. The individual modulus was first tested in a lab separately to validate their respective functions, then integrated together as the whole system, which was tested and demonstrated successfully for the designed objectives. The main findings are given as the following.

1) The thermoelectric energy material was tested in gamma irradiation and can withstand up to a total ionizing dose (TID) of 124 MRads. The power output of the thermoelectric energy harvester starts from 94 mW (year 5) to 46 mW (year 55), which is enough to power the proposed monitoring and data communication system.

2) Temperature and radiation tolerant sensing and communication electronics architecture was developed and implemented using BJTs initially, and then transitioned so that the design was based on JFETs. This approach, based on minimizing the circuit complexity and number of active devices, was tested to over 2 Mrad TID (gamma, JFEt-based) and operated correctly. Testing is underway for >100 Mrad exposure, a TID that the JFET-based circuits should tolerate.

3) The through wall ultrasound data transmission system was fabricated and tested at both room temperature and elevated temperature. The system has been tested in gammas radiation facility and has shown the capability of withstanding strong Gamma radiation for over 101 Mrad TID.

4) The integrated system was tested in a high temperature environment and successfully demonstrated to be able to harvest thermal energy and power the data communication system at elevated temperature. Destructive experiment results suggested that the maximum temperature of the system could survive is 190-195 °C because of the failure of the PCB board and the glue between the piezoelectric transducers and the metal wall at higher temperature.

5) Tungsten boron carbide (W-B4C) based shielding for both gamma-ray and neutron radiations was designed and simulated to ensure the proposed self-powered through-wall communication system to survive in 55 years of spent fuel canister service life.

This chapter is adapted from a published paper of the author, "Modeling the selective laser melting-based additive manufacturing of thermoelectric powders", listed in the Publications section.

3 Chapter 3. Modeling the selective laser melting based additive manufacturing of thermoelectric powders

3.1 Chapter Introduction

The thermoelectric generator is a solid state thermal engine for thermal and electrical energy conversion using electrons and holes as the working "fluid" [85]. The conventional methods, such as hot press and spark plasma sintering, are not perfect for large scale thermoelectric module fabrication because of their drawbacks in practice, such as the long processing time and misalignment issue during the assembly. Selective laser sintering (SLM, Figure 1), on the other hand, was considered as an emerging technology for thermoelectric material fabrication because of its desired characteristics to fabricate components with arbitrary shape. During the SLM process, it was easy to implement chemical composition adjustment and functionally doping along the thermo-element, the average ZT value of the thermoelectric module could be improved. A novel optimization method for the construction of high efficient segmented TEGs was outlined in a recent literature. [86] The cross-sectional area and the chemical composition of the thermoelectric element varied with the temperature profile to achieve highest energy conversion efficiency. This complicate geometry could only be realized by SLM. By integrating nanostructured nanocomposites, SLM manufacturing offered unprecedented opportunities of manipulating electron and phonon transport for the significant enhancement of figure-of-merit (ZT) [87-90]. In a recent research done by Tang et al. [91], an averaged ZT of ~0.7 in the temperature range of 300-550 K was achieved in the n-type $Bi_2Te_{2.7}Se_{0.3}$ fabricated by laser sintering. The performance of the sintered thermoelectric material was comparable to materials commercially available. However, there was still a lack of modeling work to analyze the impacts of the processing parameters on the deposited thermoelectric material.

The SLM process [92] uses a high power laser (Figure 1(a)), for example, a carbon dioxide laser, to fuse specific material powders into a mass that has a desired shape and physical properties. It fabricated the components layer by layer (1-200 μm) according to the 3-D digital description of the part which generated from CAD file or scan data. Due to its high energy input, SLM can fabricate high melting-temperature material with high density (up to 99% full density) without adhesives for binding purpose, which was extremely desired for the thermoelectric materials fabrication.

The powder changes from solid phase to liquid phase and then back to solid phase rapidly and repeatedly during the SLM fabrication (Figure 1(b)). The latent heat was released or absorbed at the moving boundary created by the moving laser. Though an inert gas environment is sustained during the SLM fabrication, oxidation might happen even if a small amount of oxygen existing in the environment. Since the evaporation caused by the operation temperature as high as 1500 °C, the control of the deposited material properties is a practical problem. At the edge of the melting pool, the powders are in a state of partly solid and partly liquid making its properties very different from the other parts of the powder bed. The properties of the material depends on the temperature evolution. Varying the SLM process parameters, such as the laser wavelength, energy power, laser scan speed and spacing, and powder characteristics dramatically influence the resulting part properties, such as surface quality and part density.

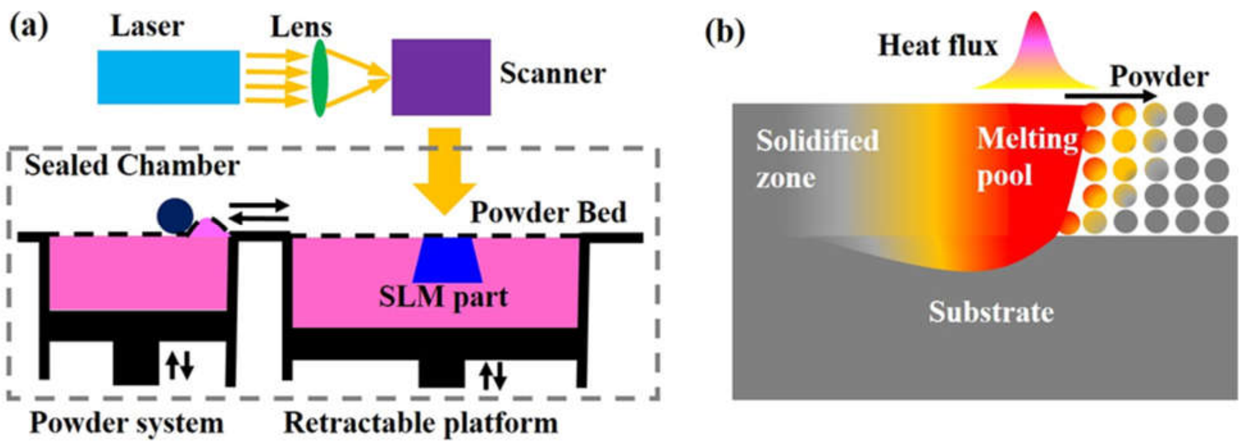

Figure 3.1. (a) The SLM equipment and (b) fabrication process

A laser beam with adjustable power input and diameter was used to heat and melt the thermoelectric powders. The absorption of the laser beam in the material was known to depend on several factors such as the material absorption coefficient, the nature of the surface, the wavelength of the incident laser beam, and surface temperature. For simplicity, a surface Gaussian heat flux was assumed in many modeling works [93, 94]. The more sophisticated model took the penetration depth and material absorption coefficient into consideration [95].

Fluid behavior has great influence on the physical properties of the deposited materials. The fluid pattern associated with the heat and mass transfer processes within the melting pool strongly depends on the fluid phenomenon, such as viscosity, surface tension (or Raleigh instabilities), thermo-capillary (or Marangoni convection), wetting, evaporation, and oxidation. Therefore, it is necessary to develop a sound physical model which incorporates the functions to study the impacts of the processing parameters on the sintered materials. Computational heat and mass analysis [96, 97] and the lattice Boltzmann method [98, 99] were two important tools to address this issue. Computational heat and mass analysis was widely used for the modeling of the melting and re-solidification process during the SLM fabrication. Voller and Brent [100] summarized the one-phase modeling of binary alloy solidification systems into three general models according to the problem domain. These models successfully predicted the aggregation patterns during the solidification. Li et al. [97] established a three-dimensional numerical model to study the laser melting of ceramic materials. This model tool the binary phase diagram of the sintered ceramic material into consideration and had the capacity to track phase change phenomena and flow motion in the melting pool. Xiao and Zhang [96] developed an even comprehensive physical model, in which functions were added to study the shrinkage phenomena in the powder bed and the fluid flow driven by buoyancy force and surface tension gradient. Recently, Luo et al. [101] built a three dimensional transient finite element model to analyze the temperature and stress fields during the SLM of SnTe using ANSYS. Their model considered the latent heats associated with the melting and vaporization phenomena.

In this paper, a 3D model was developed to simulate the SLM manufacturing of thermoelectric material (Mg_2Si powder) with nanoparticles (Si nanoparticles) embedded for high thermoelectric performance. This physical model cooperating the ability to analyze the fluid flow driven by buoyancy force and surface tension, can be utilized to analyze the influence of the process parameters on the pool size, particle aggregation, and temperature profile in the powder bed. The governing equations, including the continuity, momentum, energy, and nanoparticles transport equations, were discrete using the finite volume method (FVM), and then solved in a pressure-based manner. The total variation diminishing (TVD) discretization scheme was used for all the governing equations to preserve second order accuracy and unconditional stability. The SIMPLER algorithm integrated with the alternating direction implicit (ADI) method and block correction method was used to accelerate the convergence. The shrinkage of the powder bed during the SLM fabrication was tracked using an adaptive grid method.

3.2 The mathematical model

3.2.1 The physical model

The concept of using SLM for thermoelectric powder fabrication was shown in Figure 2(a). SLM was a non-equilibrium manufacturing method, which can produce tremendous grain boundaries and defects within the sintered material. As shown in Figure 2(b), a Gaussian laser beam was moving over the powder bed with a velocity of U_b. The powders absorbed partition of the laser energy and formed a liquid pool in which the un-melted nanoparticles might be aggregated. The melting pool cooled down and solidified into a densified part after the laser beam moving away. As shown in Figure 2(b), four distinct regions, including a un-sintered region, a sintered region, a mushy region, and a fluid region with dispersed nanoparticles, were identified in the powder bed. This system can be described by the conservation equations governing the transport of mass, momentum, energy, and nanoparticles. The computational domain had a size of 3.6 mm× 1.2 mm× 1.2 mm, which was much larger than the melting pool. The temperature on the boundaries far away from the melting pool were assumed constant. In this model, only half of the powder bed was simulated to save half of the computational resource.

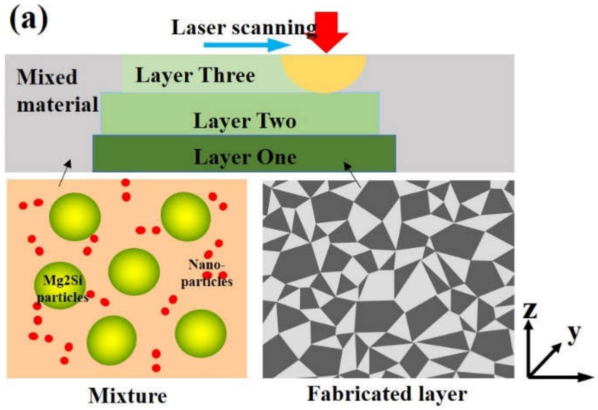

Figure 3.2. (a) SLM manufacturing of multi-component thermoelectric powders with nanoparticles embedded. (b) Four distinct regions in the powder bed.

3.2.2 Governing equations

The model used for the simulation was a one phase model developed based on one of the three general models illustrated in ref. [100] according to the current problem domain. Like the treatment in ref. [96], some terms of the governing equations were modified to fit the situation of moving coordinate. The assumptions made to simplify the problem were illustrated as follows:

A single-phase model was developed for the simulation inspired by the models illustrated in [102], based on the current problem domain. Moreover, similar to the technique in [103], the governing equations were relatively modified to fit the moving coordinates. To simplify the problem, some assumptions were made as follows:

a. The density of the powder bed was assumed uniform. Because of the presence of liquid during the sintering, the gas in the porous structure was squeezed out gradually. In the fluid region and the sintered region, the gas was completely drain out.

The powder bed was assumed to be uniform in density. During the sintering process, the gas in the porous structure was squeezed out gradually by the pressure introduced by the liquid. Finally, in the liquid region and the solidified region, the gas was completely out.

b. The buoyancy force caused by the density change was evaluated by the Boussinesq approximation.

The Boussinesq approximation was used to calculate the buoyancy force introduced by the density change.

c. The thermo-physical properties, including the thermal conductivity, specific heat, viscosity, and diffusion coefficient, were constant for the powders. But their values were different in the solid, mushy, and liquid regions because of phase change.

The powders have constant thermo-physical properties, including the thermal conductivity, specific heat, viscosity, and diffusion coefficient. However, those values would not stay the same after phase change.

d. The velocity induced by the shrinkage of the powder bed is in the *z*-direction. It only had impacts on the regions near the powder bed surface.

The shrinkage only has influence over z-direction. Its impact on x and y directions was neglected.

e. The code here focuses on the simulation of the first trail on the powder bed. However, it can be easily adapted to simulate other cases in the SLM process.

The first trail on the powder bed is the focus of this code. However, not much effort is needed to adapt the code to simulate SLM process for multi-trail or other cases.

Similar to the cases in refs. [96, 104], the laser beam was moving on the powder bed with a constant speed (u_b). The governing equations were accommodated to a one-phase model for all the four distinct regions in a moving coordinate system as follows.

The scanning speed of the laser beam remained constant (u_b). A one-phase model accommodated the governing equations in a moving coordinate for all the four regions shown below:

The continuity equation

$$\frac{\partial \rho}{\partial t} + \frac{\partial\left(\rho(u-u_b)\right)}{\partial x} + \frac{\partial(\rho v)}{\partial y} + \frac{\partial(\rho w)}{\partial z} = 0 \tag{3.1}$$

The momentum equation

$$\frac{\partial\left(\rho(u-u_b)\right)}{\partial t} + \frac{\partial\left[\rho(u-u_b)^2\right]}{\partial x} + \frac{\partial\left(\rho(u-u_b)v\right)}{\partial y} + \frac{\partial\left(\rho(u-u_b)w\right)}{\partial z} = -\frac{\partial p}{\partial x} + \frac{\partial}{\partial x}\left(\mu^+ \frac{\partial u}{\partial x}\right) + \frac{\partial}{\partial y}\left(\mu^+ \frac{\partial u}{\partial y}\right) + \frac{\partial}{\partial z}\left(\mu^+ \frac{\partial u}{\partial z}\right) \tag{3.2}$$

$$\frac{\partial(\rho v)}{\partial t} + \frac{\partial\left[\rho v(u-u_b)\right]}{\partial x} + \frac{\partial(\rho v v)}{\partial y} + \frac{\partial(\rho v w)}{\partial z} = -\frac{\partial p}{\partial y} + \frac{\partial}{\partial x}\left(\mu^+ \frac{\partial v}{\partial x}\right) + \frac{\partial}{\partial y}\left(\mu^+ \frac{\partial v}{\partial y}\right) + \frac{\partial}{\partial z}\left(\mu^+ \frac{\partial v}{\partial z}\right) \tag{3.3}$$

$$\frac{\partial(\rho w)}{\partial t}+\frac{\partial[\rho w(u-u_b)]}{\partial x}+\frac{\partial(\rho wv)}{\partial y}+\frac{\partial(\rho ww)}{\partial z}=-\frac{\partial p}{\partial z}+\frac{\partial}{\partial x}\left(\mu^+\frac{\partial w}{\partial x}\right)+\frac{\partial}{\partial y}\left(\mu^+\frac{\partial w}{\partial y}\right)+\frac{\partial}{\partial z}\left(\mu^+\frac{\partial w}{\partial z}\right)+$$
$$\rho_{ref}g_r(T-T_e)(\beta_T+\beta_s C_s)$$

(3.4)

The energy equation

$$\frac{\partial(\rho h)}{\partial t}+\frac{\partial(\rho h(u-u_b))}{\partial x}+\frac{\partial(\rho hv)}{\partial y}+\frac{\partial(\rho hw)}{\partial z}=\frac{\partial}{\partial x}\left(k^+\frac{\partial T}{\partial x}\right)+\frac{\partial}{\partial y}\left(k^+\frac{\partial T}{\partial y}\right)+\frac{\partial}{\partial z}\left(k^+\frac{\partial T}{\partial z}\right)+S_h$$

(3.5)

The nanoparticle transport equation

$$\frac{\partial(\rho C^+)}{\partial t}+\frac{\partial\left(\rho C^+(u-u_b)\right)}{\partial x}+\frac{\partial(\rho C^+v)}{\partial y}+\frac{\partial(\rho C^+w)}{\partial z}=\frac{\partial}{\partial x}\left(D^+\frac{\partial C^+}{\partial x}\right)+\frac{\partial}{\partial y}\left(D^+\frac{\partial C^+}{\partial y}\right)+\frac{\partial}{\partial z}\left(D^+\frac{\partial C^+}{\partial z}\right)+S_C$$

(3.6)

where u, v, and w are the velocities in x, y, and z directions respectively, ρ is the density, p is the pressure, h is the enthalpy, μ^+ is the effective viscosity, k^+ is the effective thermal conductivity, C^+ is the effective particle concentration, D^+ is the effective diffusion coefficient, S_C and S_h are source terms for the energy equation and nanoparticle equation respectively, β_T is the liquid thermal expansion coefficient, β_s is the solid particle expansion coefficient, and C_s is the solid mass concentration.

Because the thermal expansion coefficient and mass concentration of Si nanoparticle were relatively small, Si nanoparticles played a minor role in the Buoyance force. Thus the solid expansion term in Eq. (4) was neglected in the calculation. Like the treatment in ref. [96], the relative velocity (w_s) to the coordinate system caused by the shrinkage of the porous powder bed was given by

Since the Si nanoparticles had relatively small thermal expansion coefficient and mass concentrations, they had little influence over buoyance force. Therefore, in Eq. (4), its effect over solid expansion was neglected. Similar to the method in reference [103], the relative velocity (w_s) to the coordinate introduced by shrinkage could be calculated by:

$$w_s=\begin{cases}0, & z\geq s\\ \varepsilon\left(\frac{\partial s}{\partial t}-u_b\frac{\partial s}{\partial x}\right), & z<s\end{cases}\tag{3.7}$$

It was assumed that the powders started to melt at $T_M-\Delta T$, and became fully melted at a temperature of T_M. The mass fraction of the liquid was assumed linearly correlated to the temperature in this temperature interval (ΔT). To simplify the model, the porosity of the fully melted material was assumed 0.0. Also, no density changes during the phase change process.

One of the assumptions was that that the powders started to melt at $T_M - \Delta T$, and melted completely at a temperature of T_M. Moreover, it was assumed that the mass fraction of the liquid was linearly correlated to the temperature in this temperature window. At the same time, the porosity of the melted liquid was assumed to be 0. Also, the density remained unchanged during the phase change process.

$$f_l = \begin{cases} 1, & T \geq T_M \\ \frac{T_M - T}{\Delta T}, & T_M - \Delta T < T < T_M \\ 0, & T < T_M - \Delta T \end{cases} \tag{3.8}$$

The physical properties of the partially melted material in the mush region were simplified as the summation of that of the powder and liquid weighted by their corresponding mass fractions. The effective diffusion coefficient and the effective thermal conductivity were given by

It was also assumed that the physical properties of the partially melted material in the mushy region had a linear relationship to the fractions of liquid mass and powder mass. The effective diffusion coefficient and the effective thermal conductivity were as below:

$$\mu^+ = \mu_s f_s + \mu_l f_l \tag{3.9}$$

$$k^+ = f_s k_s + f_l k_l \tag{3.10}$$

The powders used for the laser sintering was not pure materials. For example, doping elements and additive nanoparticles were mixed with the thermoelectric powders to enhance the ZT value. The thermal conductivity of the final powders was assumed to be the summation of the thermal conductivity (k_{pi}) of the different powder components weighted by their corresponding mass fractions (g_{pi}).

The powders used in the process were not completely pure. Doping materials and nanoparticles were also in the powders to enhance the ZT value. Similar to above, the thermal conductivity of the mixture was assumed to be the summation of the thermal conductivity (k_{pi}) of the different powder components weighted by their corresponding mass fractions (g_{pi}).

$$k_p = \sum_{i=1}^{n} g_{pi} k_{pi} \tag{3.11}$$

For a randomly packed powder bed with large thermal conductivity ratio (k_p/k_g, k_p and k_g were the thermal conductivities of the particle and gas, respectively), an empirical equations built by Hadley [105] and further outlined in ref. [96] was employed to estimate the effective thermal conductivity of the mixed powders.

To estimate the effective thermal conductivity of the porous powder bed in the SLM process, an empirical equation was used which was built by Hadley [105] and further outlined in ref. [96]. The equation is capable to calculate the effective thermal conductivity of a porous material whose solid fraction has a much higher thermal conductivity than its gas fraction.

$$\frac{k_{eff}}{k_g} = (1-\alpha_0)\frac{\varepsilon f_0 + (k_p/k_g)(1-\varepsilon f_0)}{1-\varepsilon(1-f_0)+\varepsilon(k_p/k_g)(1-f_0)} + \alpha_0 \frac{2(k_p/k_g)^2(1-\varepsilon)+(1+2\varepsilon)(k_p/k_g)}{(2+\varepsilon)(k_p/k_g)+1-\varepsilon} \tag{3.12}$$

where

$$f_0 = 0.8 + 0.1\varepsilon, \tag{3.13}$$

$$\log \alpha_0 = \begin{cases} -4.898\varepsilon & 0 \le \varepsilon \le 0.0827 \\ -0.405 - 3.154(\varepsilon - 0.0827) & 0.0827 \le \varepsilon \le 0.298 \\ -1.084 - 6.778(\varepsilon - 0.298) & 0.298 \le \varepsilon \le 0.580 \end{cases} \tag{3.14}$$

The concentration of the additive particles in original powder was C_s. The nanoparticle concentration ratio between the solid and the liquid was assumed to be a constant ($C_s = \varphi C_l$). Similar to the treatment in ref. [10], the effective nano-particle diffusive coefficient of the powder was estimated by

$$D^+ = f_s D_s + f_l D_l/\varphi \tag{3.15}$$

The thermal capacity of the powders was temperature dependent. The enthalpy of the powders was calculated by the integration of thermal capacity.

$$h = \int_0^T c_{ps} dT \tag{3.16}$$

The melting and solidification processes accompanied latent heat absorption and release. The latent heat was proportional to the liquid mass fraction. The enthalpy change during the phase transition can be divided into two parts, including the thermal capacity change and the latent heat.

The impact of the latent heat was also important here. Both melting and re-solidification process were involved with it. Moreover, the latent heat was proportional to the liquid mass fraction. Two parts existed in the enthalpy change during the phase transition which were the thermal capacity change and the latent heat.

$$\delta H = \left[\int_0^T (c_{pl} - c_{ps})\, dT + L\right] f_l \tag{3.17}$$

As the thermal capacity of the liquid and the solid was assumed the same in this study, Eq. (3.17) was simplified as

$$\delta H = \begin{cases} 0, & T < T_M - \Delta T \\ L f_l, & T_M - \Delta T < T < T_M \\ L, & T > T_M - \Delta T \end{cases} \tag{3.18}$$

The source term for the energy equation were adapted from ref. [100]. While the first term was the transient term caused by the latent heat absorption and release, the others were the source terms introduced by the mass convection in the melting pool.

The source terms were developed as below. The first term was the transient term introduced by the latent heat and the others were the source terms caused by the mass convection in the melting pool.

$$S_h = \frac{-\partial}{\partial t}(\rho\delta H) - \frac{\partial}{\partial x}(\rho(u-u_b)\delta H) - \frac{\partial}{\partial y}(\rho v\delta H) - \frac{\partial}{\partial z}(\rho w\delta H) \tag{3.19}$$

The source terms for nanoparticle transport equation was presented in Eq. (20), where the first term on the right of the equation was the transient term caused by the melting and solidification of the power, and the other terms were introduced by the mass convection.

Eq. (20) was the source terms for nanoparticle transport, where the first term on the right hand side of the equation was the transient term caused by the melting and solidification of the powder, and the other terms were the mass convection.

$$S_C = \frac{-\partial}{\partial t}\left[\left(\frac{1}{k}-1\right)\rho f_1 C_s\right] - \frac{\partial}{\partial x}\left[\left(\frac{1}{k}-1\right)\rho f_1 C_s(u-u_b)\right] - \frac{\partial}{\partial y}\left[\left(\frac{1}{k}-1\right)\rho f_1 C_s v\right] - \frac{\partial}{\partial z}\left[\left(\frac{1}{k}-1\right)\rho f_1 C_s w\right] \tag{3.20}$$

3.2.3 Shrinkage tracking

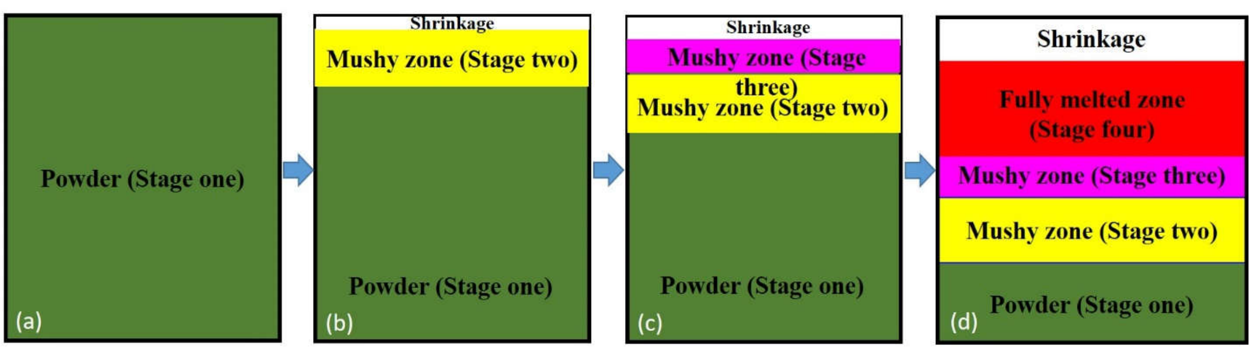

Figure 3.3. The shrinkage phenomenon in the powder bed during the SLM process: (a) Stage One, (b) Stage Two, (c) Stage Three, (d) Stage Four.

Because of the capillary effect and gravity force, when the powder was melted, the liquid would take the place of the gas gap, forming a liquid pool of full density. The shrinkage in the powder bed introduced extra difficulty to the thermal and fluid analysis for the SLM process. In this paper, the heating process was divided into four sub-stages (Figure 3).

After the powders were melted, the capillary effect and gravity force would drive the liquid to take the place of the gap which used to be the air, to form a liquid pool. Therefore, a shrinkage would happen because of the difference in their densities. In this paper, 4 stages were set to represent the different status of the materials in the heating process.

Stage One: Pre-heating ($T < T_M - \Delta T$)

At this stage, the temperature of the heated powder was lower than the melting point. No melting and shrinkage happened in the powder bed.

At this stage, the melting point was not reached. So no melting would happened till next stage in the powder bed.

Stage Two: Preliminary melting ($T_M - \Delta T \leq T \leq T_M - \Delta T \frac{\varepsilon}{1-\varepsilon}$)

At this stage, only a small proportion of the powders was melted. A partition of the gas gap within the powder was occupied by the liquid. The volume of the powder melted in a local grid can be expressed as $f_l(1-\varepsilon)dxdydz$. Since the gas gap volume in the powder bed was not completely filled at this stage, the shrinkage volume in the powder equaled to the melted powder volume, which was given by

At this stage, only a small part of the powders was melted. The liquid took up a partition of the gap where used to be gas. The volume of the powder melted in a local grid can be expressed as $f_l(1-\varepsilon)dxdydz$. Currently, the gas was not fully driven out, so the shrinkage volume in the powder equaled to the melted powder volume, which was given by

$$\Delta S_2 = f_l(1-\varepsilon)dxdydz \tag{3.21}$$

Stage Three: Partially melting ($T_M - \Delta T \frac{\varepsilon}{1-\varepsilon} < T < T_M$)

At this stage, as the gas within the powder bed was completely driven out, further powder melting would not lead to further shrinkage. The shrinkage at the local position equaled to the volume of the powder porosity.

At this stage, the gas in the powders was completely out, thus the melting would not cause further shrinkage due to gas driven out. The shrinkage at the local position equaled to the volume of the powder porosity.

$$\Delta S_3 = \varepsilon dxdydz \tag{3.22}$$

Stage Four: Fully melting ($T \geq T_M$)

At this stage, the powders were fully melted and no gas was left in the powder bed. As the density change was not considered during the phase change process, no further shrinkage happened in this stage.

At this stage, there were neither powder left, nor the gas. Because the density change was not considered during phase change process, no shrinkage would happen in this stage any further.

$$\Delta S_4 = \varepsilon dxdydz \quad (3.23)$$

Accumulated shrinkage

The accumulated shrinkage in the powder bed was calculated by integrating the shrinkage of each cell along the z-direction.

$$s = \left(\sum_{T_M-\Delta T}^{T_M-\Delta T*\frac{1-\varepsilon}{\varepsilon}} \Delta S_2 + \sum_{Tf}^{T_M} \Delta S_3 + \sum_{T_M}^{T_{MAX}} \Delta S_4 \right) / (dxdy)$$

(3.24)

3.2.4 The boundary conditions

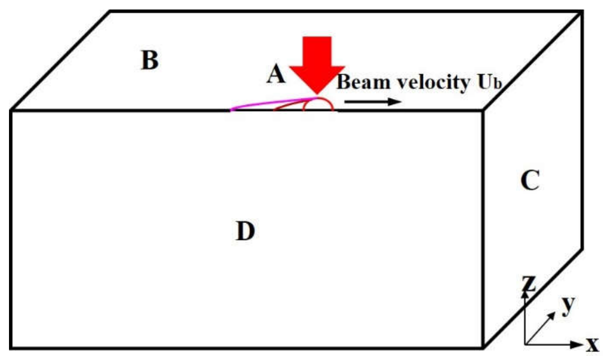

Figure 3.4. The boundaries of the computation domain.

Boundary A (The heating spot in Figure 4): A Gaussian heat flux entered into the powder bed through boundary A. A part of the energy was lost through convection and radiation.

$$-k_{eff}\partial T/\partial z|_{z=s} = \theta q_{laser} + h_c(T - T_a) + \varepsilon_b \sigma_b (T^4 - T_a^4) \quad (3.25)$$

where the Gaussian heat flux was given by

$$q_{laser} = -\frac{q_0}{\pi R^2} exp\left(-\frac{r^2}{R^2}\right) \quad (3.26)$$

The thermo-capillary effect was caused by the temperature gradients near the power bed surface. The shear force and surface tension at the free surface was assumed to achieve a balance during the SLM process.

The temperature gradients near the powder bed surface caused the thermo-capillary effect. It was assumed that the shear force and surface tension at the free surface reached a balance.

$$\mu^{+}\left(\partial v_{s_1}/\partial n_1 + \partial v_{n1}/\partial s_1\right) = \sigma_{s_1}\frac{\partial T}{\partial s_1}\ (xz\ plane) \tag{3.27}$$

$$\mu^{+}\left(\partial v_{s_2}/\partial n_2 + \partial v_{n2}/\partial s_2\right) = \sigma_{s_2}\frac{\partial T}{\partial s_2}\ (yz\ plane) \tag{3.28}$$

The nanoparticle concentration gradient was zero at this boundary.

$$\partial C^{+}/\partial z|_{z=s} = 0 \tag{3.29}$$

Boundary B (The top surface except for A in Figure 4): All the conditions were the same to boundary A but the temperature. An energy balance was achieved at this boundary.

$$-k_{eff}\partial T/\partial z|_{z=s} = h_c(T - T_a) + \varepsilon_b\sigma_b(T^4 - T_a^4) \tag{3.30}$$

Boundary C (The right, left, and bottom surfaces in Figure 4): The side and bottom surfaces were far away from the heat source. As the thermal conductivity of the powder was relative small, the temperature fluctuations on these boundaries were minimal. Thus constant temperatures were assumed on these surfaces.

It could be seen that the side and bottom surfaces were far away enough from the heat source. Moreover, the thermal conductivity of the powder was pretty small and the temperature fluctuations on these boundaries were neglectable. Then the constant temperatures were assumed on these surfaces.

$$T = T_a \tag{3.31}$$

No particle motion was assumed on the boundary. The nanoparticle concentration gradient was zero.

$$u = v = w = 0 \tag{3.32}$$

$$\partial C^{+}/\partial x|_{z=0,L} = 0 \tag{3.33}$$

Boundary D (The front surface in Figure 4): It is a symmetric surface.

$$\partial T/\partial y|_{y=0} = 0 \tag{3.34}$$

$$v = 0, \frac{\partial u}{\partial y} = \frac{\partial w}{\partial y} = 0 \tag{3.35}$$

$$\partial C^{+}/\partial y|_{y=0} = 0 \tag{3.36}$$

3.2.5 Numerical procedures

The SLM process was a three-dimensional quasi-steady state heat and mass transfer problem in a moving coordinate system. The mathematical model, specified by the continuity, momentum, energy, and nano-particle transport equations (equation (1)-(6)), as well as the constitute equations (equation (7)-(20)), were solved numerically using the SIMPLER algorithm [106]. The properties of the material were updated according to the temperature updated from the last iteration. Because the shrinkage of the powder surface was unknown beforehand, a false transient method was employed for surface tracking. The solution was assumed converged when the velocity and temperature distributions did not change with the false time. The convection and diffusion terms were discretized utilizing a total variation diminishing (TVD) scheme proposed by Van Leer [107] with the limiter function given by Eq. (37). The TVD scheme was utilized here because it was of second order accuracy and unconditionally stable without overshoot.

The SLM process should be considered as a three-dimensional quasi-steady state heat and mass transfer problem in a moving coordinate system. The SIMPLER algorithm [106] was used to solve the model numerically which involved the continuity, momentum, energy, and nano-particle transport equations (equation (1)-(6)), as well as the constitute equations (equation (7)-(20)). The properties of the material were updated simultaneously as the temperature was updated from the last iteration. For the surface tracking without knowing the shrinkage of the powder surface beforehand, a false transient method was employed. The solution was assumed to converge when the velocity and temperature distributions did not change with the false time. A total variation diminishing (TVD) scheme proposed by Van Leer [107] with the limiter function given by Eq. (37) was utilized to discretize the convection and diffusion terms. The TVD scheme was of second order accuracy and unconditionally stable without overshoot.

$$\psi(r) = \frac{r+|r|}{1+r} \tag{3.37}$$

The discretized equations in a three-dimensional Cartesian grid system was extended from that in a two-dimensional system documented in ref. [108],

$$a_P\phi_P = a_W\phi_W + a_E\phi_E + a_S\phi_S + a_N\phi_N + a_F\phi_F + a_B\phi_B + S_u^{DC} + S_\phi \tag{3.38}$$

where the central coefficient was

$$a_P = a_W + a_E + a_S + a_N + a_F + a_B + (F_e - F_w) + (F_n - F_s) + \left(F_b - F_f\right)$$

and a_W, a_E, a_S, a_N, a_F and a_B were the TVD neighbor coefficients [108].

The deferred correction source term was given by

$$S_u^{DC} = \frac{1}{2}F_e[(1-\alpha_e)\psi(r_e^-) - \alpha_e\psi(r_e^+)](\phi_E - \phi_P) + \frac{1}{2}F_w[-(1-\alpha_w)\psi(r_w^-) + \alpha_w\psi(r_w^+)](\phi_P - \phi_W) + \frac{1}{2}F_n[(1-\alpha_n)\psi(r_n^-) - \alpha_n\psi(r_n^+)](\phi_N - \phi_P) + \frac{1}{2}F_s[-(1-\alpha_s)\psi(r_s^-) + \alpha_s\psi(r_s^+)](\phi_P - \phi_S) + \frac{1}{2}F_b[(1-\alpha_b)\psi(r_b^-) - \alpha_b\psi(r_b^+)](\phi_B - \phi_P) + \frac{1}{2}F_f\left[-\left(1-\alpha_f\right)\psi\left(r_f^-\right) + \alpha_b\psi(r_b^+)\right](\phi_P - \phi_B) \tag{3.39}$$

where $r_e^+, r_e^-, r_w^+, r_w^-, r_n^+, r_n^-, r_s^+, r_s^-, r_b^+, r_b^-, r_f^+$, and r_f^- are defined the same to ref. [108].

The thermal boundaries was treated using the additional source term method. A grid system with uniform structured hexahedron grids 200×90×90 in the *x*, *y*, and *z* directions, was utilized. The false time step was 0.0001 s to make sure CFL<1.0 for all the grids. The iterative procedure continued until the residuals of all the governing equations were less than 10^{-5} for each time step. The solution was assumed to be converged when $\left|\frac{\phi_N-\phi_{N-1}}{\phi_N}\right| < 10^{-3}$. The block correction method [109] and the alternating direction implicit (ADI) method [108, 109] was employed to accelerate the convergence.

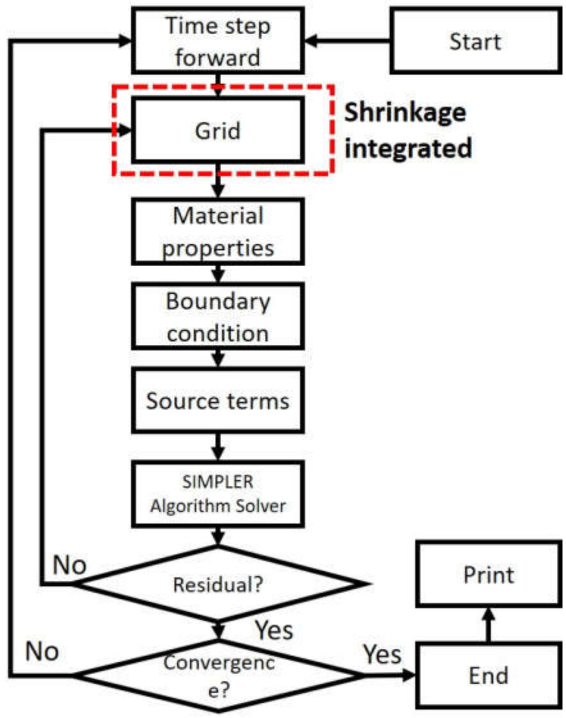

Figure 3.5. The numerical scheme for SLM simulation

3.2.6 Material physical properties and input parameters

The Mg_2Si powders were selected as the thermoelectric materials for SLM simulation. Some Si nano-particles were added into the Mg_2Si powders to enhance both the thermoelectric performance and the mechanical properties of the sintered material. The thermal conductivity of the Mg_2Si documented in ref. [110] was used to monitor the properties of the . Other physical properties of Mg_2Si, including the thermal capacity and the thermal expansion coefficient, were cited from ref. [111]. In this paper, the additive material (Si particles) was assumed weighted 10% of the total mass. The physical properties of the Si documented in ref. [112] were used for this simulation. The material physical properties and SLM conditions used for the simulation were listed in Table 1 as follows

In this SLM simulation, the Mg_2Si powders were chosen to be the working powders. A small proportion of silicon nanoparticles were added into the powder to enhance both the thermoelectric performance and the mechanical properties of the final product. The thermal conductivity of the Mg_2Si documented in ref. [110] was used in this paper. And as for other thermal and physical properties, including the thermal capacity and the thermal expansion coefficient, data from ref. [111] was used. The doping ratio of silicon particles was set to be 10%. The physical properties of silicon were cited from ref. [112]. All the properties and the conditions in the process were listed in Table 1 as below

Table 3.1. The material physical properties and SLM operation conditions

Scanning speed	$u_b = 0.01 - 0.2\ m \cdot s^{-1}$
Specific heat	$c_p = 67.87\ J \cdot kg^{-1} \cdot K^{-1}$
Solid thermal conductivity	$k_p = 7.0\ W \cdot m^{-1} \cdot K^{-1}$
Liquid thermal conductivity	$k_l = 5.0\ W \cdot m^{-1} \cdot K^{-1}$
Gas thermal conductivity	$k_g = 0.024\ W \cdot m^{-1} \cdot K^{-1}$
Porosity	$\varepsilon = 0.2$
Density	$\rho = 1990\ kg \cdot m^{-3}$
Liquid viscosity	$\mu_l = 5.0 \times 10^{-3}\ kg \cdot m^{-1} \cdot s^{-1}$
Solid viscosity	$\mu_s = 1.0 \times 10^{4}\ kg \cdot m^{-1} \cdot s^{-1}$
Specific diffusion coefficient	$D = 4.8 \times 10^{-9}\ m^2 \cdot s^{-1}$
Latent heat	$L = 4.5 \times 10^{5}\ J \cdot kg^{-1}$
Permeability coefficient	$K_0 = 2.0 \times 10^{6}\ kg \cdot m^{-3} \cdot s^{-1}$
Thermal expansion coefficient	$\beta_T = 1.1 \times 10^{-5}\ K^{-1}$
Melting point of pure material	$T_M = 1375\ K$
Equilibrium partition ratio	$k = 0.8$
Ambient temperature	$T_a = 298.15\ K$
Convective heat transfer coefficient	$h_c = 10.0\ W \cdot m^{-2} \cdot K^{-1}$
Laser diameter	$R = 0.003\ m$

Laser intensity	$Q = 10\sim100\ W$
Boltzmann constant	$\sigma_b = 5.67 \times 10^{-8}\ W \cdot m^{-2} \cdot K^{-4}$
Change rate of surface tension	$\partial\sigma/\partial T = -10^{-5}\ kg \cdot s^{-2} \cdot K$
Laser intensity	$q_0 = 1.8 \times 10^{4}\ W \cdot m^{-2}$

3.3 Results and discussion

3.3.1 Verification of the code

Before the simulation of the multi-component powders, this code was used to simulate the SLM fabrication of the nonporous 6063 aluminum sheet with dimensions of 229×152×3.2 mm^3. In an experiment documented in ref. [113], a continuous-wave CO_2 laser with a power of 1.3 kW and a travel speed of 4.23 mm/s were used to process the nonporous aluminum sheet. The diameter of the laser beam was measured to be 0.6 mm. The heat flux distribution of the beam was Gaussian. The power absorbed by the workpiece was measured calorimetrically [114]. The measurement showed that about 86% of energy irradiated by the laser beam was lost via laser reflection, thermal radiation, and heat convection. In the simulation, the physical properties of the nonporous 6063 aluminum sheet and the boundary conditions were the same to the ref. [113]. The simulation result was compare with the simulation result presented in ref. [96, 113] and experimental result in ref. [114]. It showed that the simulated and measured fusion boundaries were in good agreement with each other.

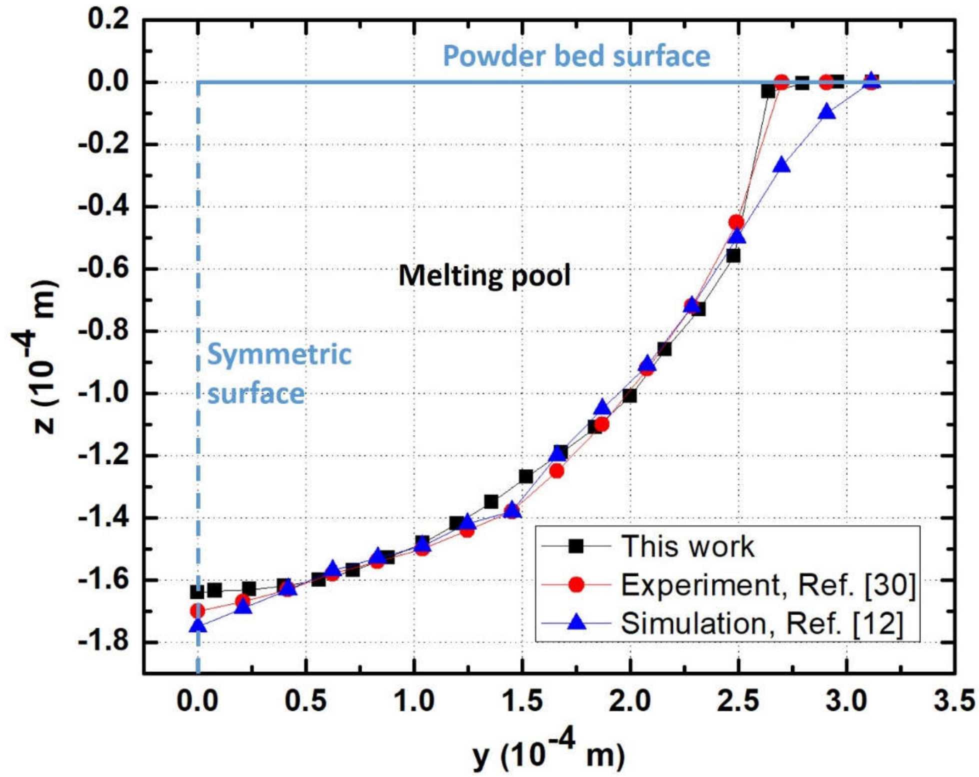

Figure 3.6. The comparison of the simulated and measured fusion boundaries for SLM of the 6063 aluminum sheet.

3.3.2 Shrinkage in the powder bed

The validated code was then used to simulate the SLM of Mg_2Si powders with Si nanoparticles mixed as the additive material. Figure 7 showed the shrinkage of the powder bed during the SLM process with different laser power inputs and scanning speeds. It was observed that the surface of the melting pool was not flat anymore. The maximum shrinkage depth was about 0.06 mm with a power input of 18.75 W. With the input power increased, the shrinkage region became broader and deeper. The scanning speed also affected the shrinkage of the powder bed. The higher scanning speed tended to uniform the temperature and thus led to more extensive and shallow shrinkage on the powder bed. Due to the shrinkage phenomenon, it was a challenge to control the contact quality between two layers of fabricated substrates. To reduce the shrinkage of the powder bed, the porosity of the powder bed should be as low as possible. Meanwhile, appropriate laser power should be selected, as too small energy input cannot melt the powder while too large energy input resulted in significant power shrinkage and substantial deposited layer overlap. Finally, the scanning speed should be adjusted according to the laser energy input. For high power laser, the scanning speed should be higher so as to alleviate the potential evaporation and oxidation caused by the high temperature. The laser power input and the scanning speed should be calibrated synchronously to achieve the optimal performance.

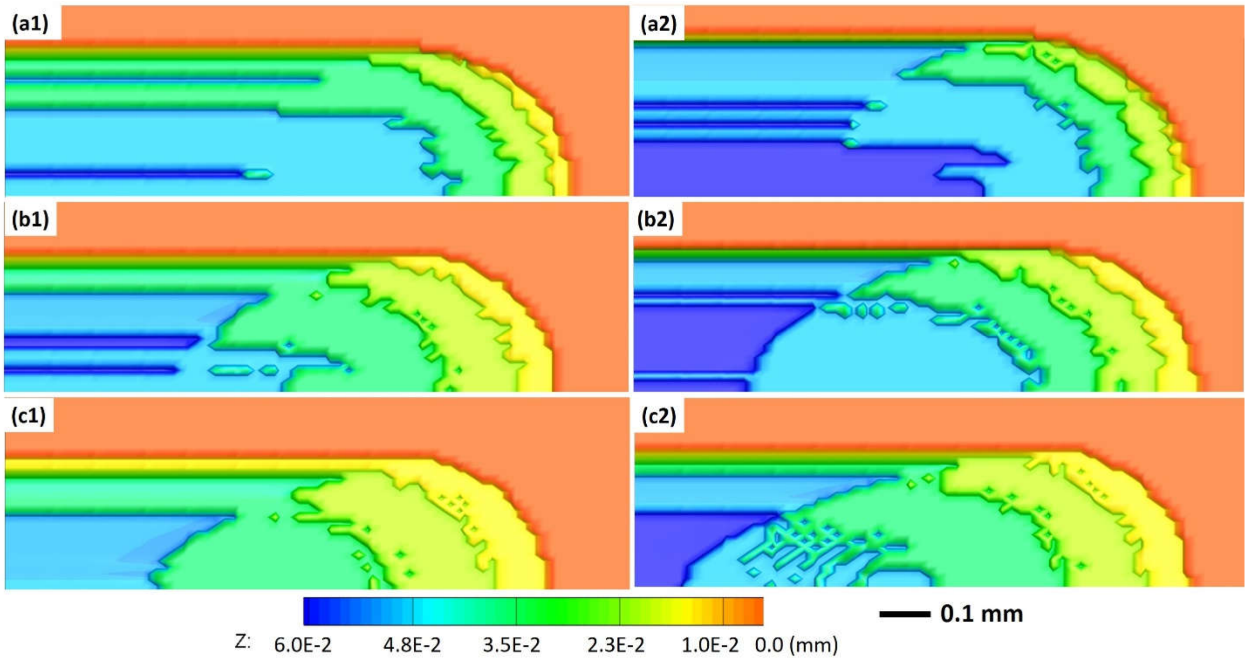

Figure 3.7. The shrinkages of the powder bed during the SLM process. P=18.75 W, R=0.3 mm, (a1) V= 0.02m/s; (b1) V= 0.04 m/s; (c1) V= 0.06 m/s; P=25 W, R=0.3 mm, (a2) V= 0.02 m/s; (b2) V= 0.04 m/s; (c2) V= 0.06 m/s.

3.3.3 Temperature profile

Shown in Figure 8 were the temperature profiles on the upper surface of the powder bed during the SLM process. A high-temperature spot was caused by the laser heating of the powder bed. As the laser beam moving from the left side to the right side, a high-temperature tail was left behind the laser. The highest temperature happened near the center of the laser on the surface of the powder bed with a peak temperature of ranges 2100-2500 K for different cases. With the laser input energy increasing, the high-temperature region expanded gradually. Since the peak temperature of the heating surface was much higher than the melting temperature, undesired evaporation and oxidation might happen during the SLM process. The input power of the laser beam should be carefully controlled to avoid such a situation. The laser scanning speed could be another factor that significantly affected the temperature distribution within the melting pool. The higher the scanning speed, the more extended high-temperature wake was observed. For the same laser energy input, the higher scanning speed resulted in lower peak temperature. By calibrating the scanning speed and the laser power, one could find the best processing parameters for specific material fabrication.

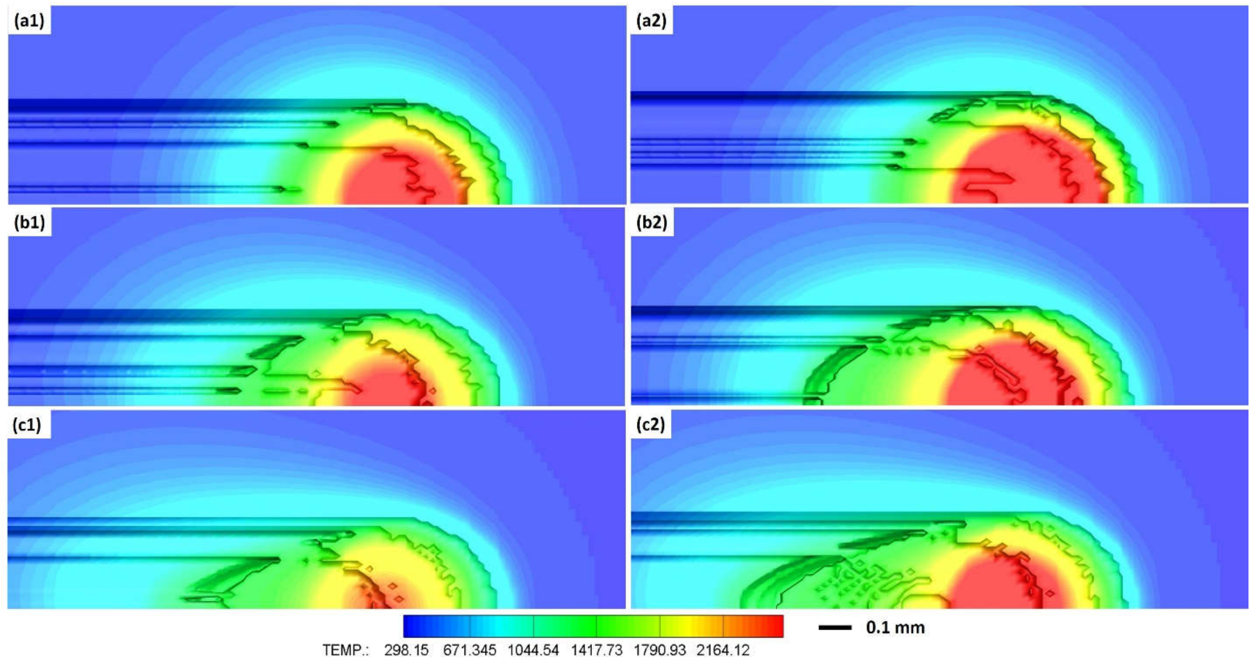

Figure 3.8. The temperature profiles during the SLM process. P=18.75 W, R=0.3 mm, (a1) V= 0.02m/s; (b1) V= 0.04 m/s; (c1) V= 0.06 m/s; P=25 W, R=0.3 mm, (a2) V= 0.02 m/s; (b2) V= 0.04 m/s; (c2) V= 0.06 m/s.

3.3.4 Melting pool size

The melting pool size played a vitally important role during the SLM process, as the pool fluid dynamics significantly influenced the quality of the fabricated parts. The melting and re-solidification phenomenon in the melting pool was effected by the convective heat and mass transfer process. The thermo-capillary and buoyancy effects, which drove the fluid circulation in the melting pool, was primarily determined by the size of the melting pool. The larger melting pool should induce stronger convection, which resulted in particles aggregation at the boundary of the melting pool. Particles aggregation was not desired to achieve uniform material properties. However, if the melting pool was too small, the powder would not be fully melted. The density of the final product would be too small to sustain good electrical conductivity, which was essential for good thermoelectric performance. Shown in Figure 9 was the melting pool sizes for different simulation cases. The red region in the figure was the fully melted region, and the green region was powder region, while the yellow and blue region was the mushy zone. It was observed that the higher energy input generated the larger the melting pool. The shape of the melting pool changed accordingly with the scanning speed. The high scanning speed led to a narrow and long melting pool in the power bed. The melting pool was not symmetrical in the scanning direction as the laser beam was moving. The un-symmetricity was more evident for the cases with the higher laser scanning speed.

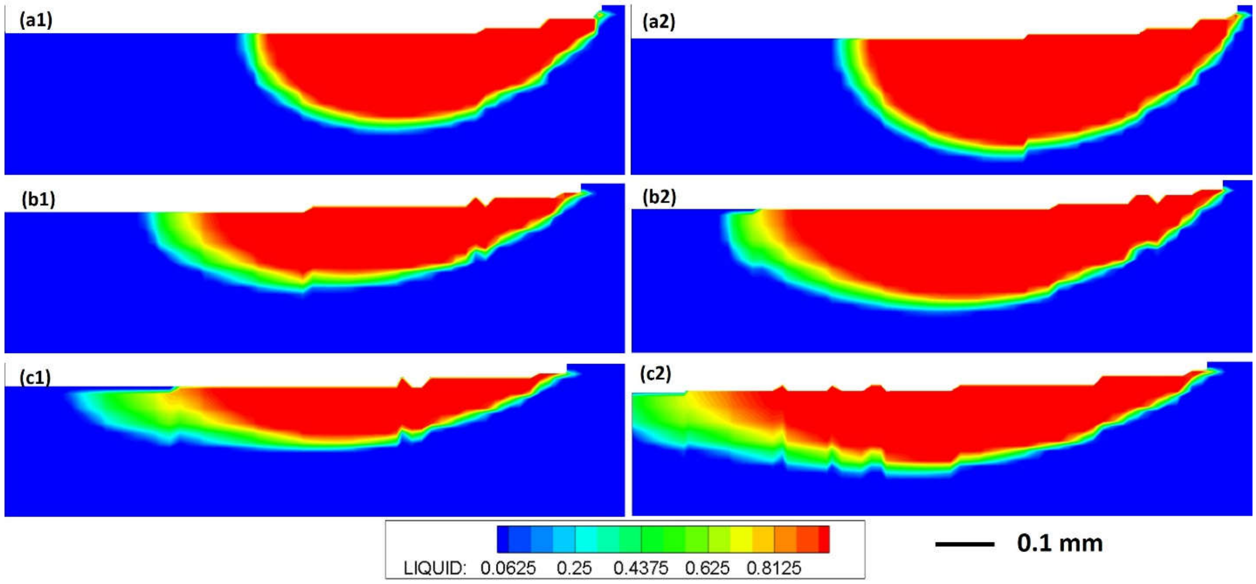

Figure 3.9. The melting pool size during the SLM process. P=18.75 W, R=0.3 mm, (a1) V= 0.02m/s; (b1) V= 0.04 m/s; (c1) V= 0.06 m/s; P=25 W, R=0.3 mm, (a2) V= 0.02 m/s; (b2) V= 0.04 m/s; (c2) V= 0.06 m/s.

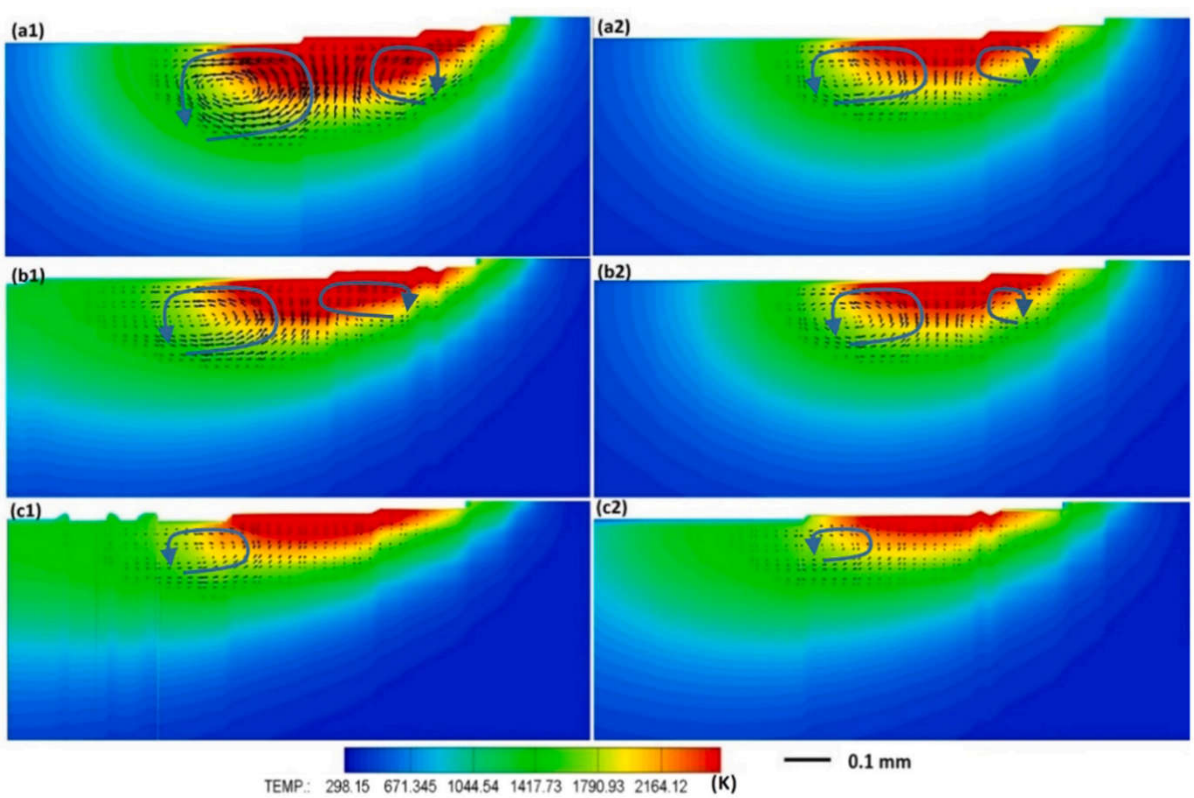

Figure 3.10. The velocity vector in the melting pool. P=18.75 W, R=0.3 mm, (a1) V= 0.02m/s; (b1) V= 0.04 m/s; (c1) V= 0.06 m/s; P=25 W, R=0.3 mm, (a2) V= 0.02 m/s; (b2) V= 0.04 m/s; (c2) V= 0.06 m/s.

3.3.5 Velocity profile

During the melting process, the non-uniform heating of the free surface led to unbalanced surface tension. The thermo-capillary flow induced by surface tension variations along the liquid-gas interface together with the buoyancy force caused by the density variation drove the fluid to circulate in the melting pool. The peak velocity, in the order of 10^{-4} mm/s, was very small. As shown in Figure 10, the circulation pattern within the melting pool was complicated. The surface tension force tended to pull the flow from the center to the edge of the melting pool, while the buoyancy force drove the flow from the bottom to the upper surface of the melting pool. With these two effects combined, a circulation was created, where the flow ran up from the center and down from the edge of the melting pool. The circulation pattern at the front face was not strictly symmetrical because of the moving laser beam, with the left circle was significant larger than the right circle. This circulation pattern found in this paper was consistent with the results documented in the literature [96, 113]. With the input power increased, the circulation and convection within the molting pool became stronger. A careful observation of the melting pool found that, with the scanning speed increased, the circulation pattern became even un-symmetrical, with the right side growing stronger and the left side being suppressed. The convection process accelerated the mass transport processes during the fabrication. Its impact on the nanoparticle aggregation should be carefully monitored and controlled during the process.

3.3.6 Nano-particle concentration

Though the Si nanoparticles were uniformly mixed with the Mg_2Si powders before the SLM process, the Si nanoparticles became non-uniformly distributed in the fabricated parts, as shown in Figure 11. It was found that the nanoparticles aggregated at the left side boundary of the melting pool, resulting in a lower concentration in the melting pool. This phenomenon was undesired for the thermoelectric material fabrication. As the doping level shifted from the optimum value, the performance of the thermoelectric material could be severely deteriorated. A potential way to combat with this phenomenon was increasing the scanning speed to shorten the residence time for material diffusion and convection. Other ways included reducing the input power to suppress the material diffusion and convection rates in the melting pool.

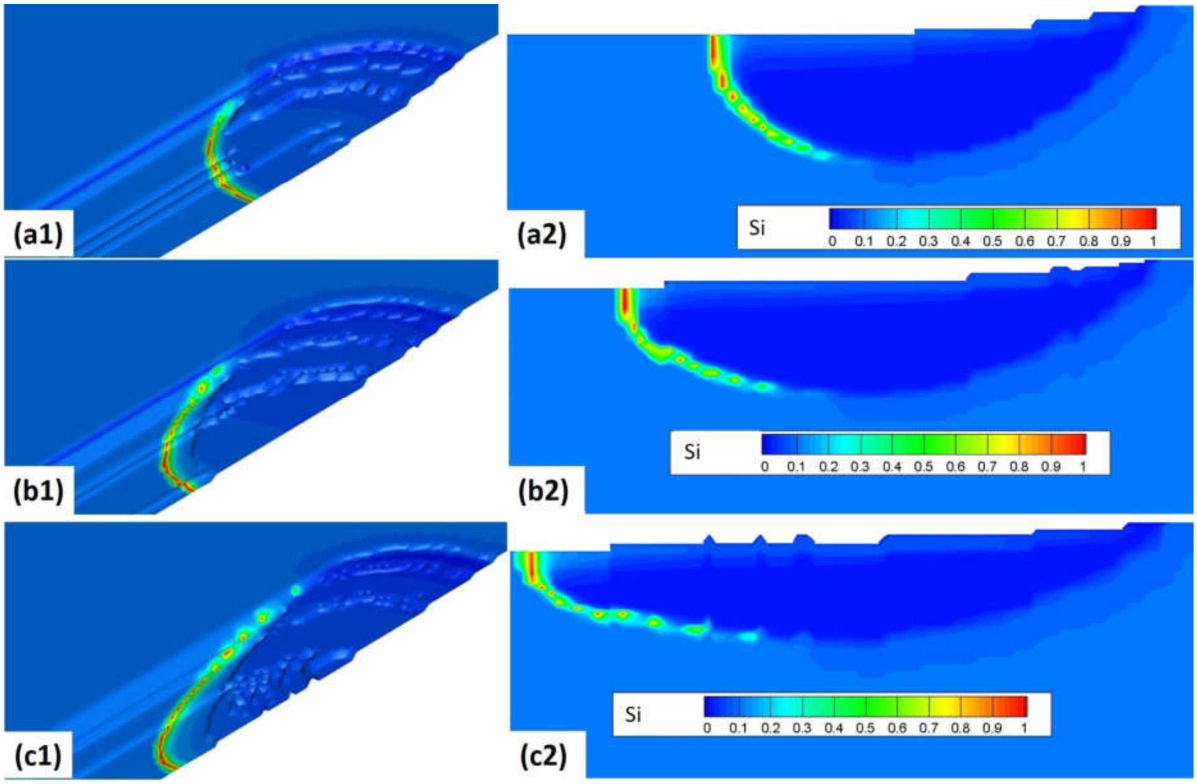

Figure 3.11. The Si nanoparticles concentration ratio distribution near the melting pool. P=18.75 W, R=0.3 mm, (a1) V= 0.02m/s; (b1) V= 0.04 m/s; (c1) V= 0.06 m/s; P=25 W, R=0.3 mm, (a2) V= 0.02 m/s; (b2) V= 0.04 m/s; (c2) V= 0.06 m/s.

3.4 Chapter Conclusion

In this paper, a comprehensive 3D model was developed to simulate the convection-diffusion process during the SLM fabrication of thermoelectric powders (Mg_2Si) embedded with nanoparticles (Si). This model provided detailed information about the shrinkage of the powder bed, the shape of the melting pool, the temperature and velocity profiles, and the nanoparticles concentration ratio in the powder bed during the SLM fabrication. The code was validated by examining a case reported in literature before it was used for the thermoelectric material simulation.

(1) Because of the porosity in the thermoelectric powder bed, a shrinkage region was observed during the SLM fabrication. The shrinkage depth and coverage area were larger for cases with larger power input. The scanning speed helped to uniform the temperature profiles. The high scanning speed resulted in a long but shallow shrinkage region on the powder bed.

(2) Both the energy input and the scanning speed had significant impacts on the melting pool. The energy input affected the size of the melting pool, while the scanning speed had more influence on the shape of the melting pool. The un-symmetricity of the melting pool was caused by the laser scanning speed direction.

The simulation results showed that the flow circulation induced by the surface tension and buoyancy force within the melting pool matched well with literature. The aggregation of the nanoparticles at the boundary of the melting pool should deteriorate the performance of the sintered thermoelectric material.

This chapter is adapted from a published paper of the author, "Direct energy deposition applied to soft magnetic material additive manufacturing", listed in the Publications section.

4 Chapter 4. Direct Energy Deposition Applied to Soft Magnetic Material Additive Manufacturing

4.1 Chapter Introduction

Additive manufacturing (AM) gets its term contrasting the subtractive manufacturing. Also known as 3D printing, it fabricates the products by printing material layer by layer from the 3D model previously prepared by computer-aided design (CAD) software. Thanks to its novel fabrication features, AM has recently converted from a mere rapid prototyping method to a widely accepted fabrication technology to solve many problems that subtractive manufacturing cannot [115]. Researchers have emphasized its usage of structural materials while seldom considering functional materials [115, 116]. Thus, there are still many blanks in the study of AM on functional material, including soft magnetic material. Works have been done on applying laser-based AM to novel materials and functionally graded materials, [117] which are very inspiring and motivate this research.

Soft magnetic materials are the materials that have reduced (ideally null) magnetocrystalline anisotropy fields [118], which appear to be easy to magnetize and demagnetize. Electrical steel (iron silicon alloy) is the most common soft magnet material in commercial use [119]. 13,560 thousand tonnes of electrical sheets and strips were fabricated in 2014 [120]. There have been studies to apply other laser-based AM techniques, including selective laser melting and ink jetting, to silicon iron [121, 122].

The objective for the soft magnetic material in this study is to have low coercivity, low core loss, and high mechanical strength to work as the motor iron cores. Additionally, considering the eddy currents, it also has to be high in electric resistance to reduce the eddy current loss [123]. The traditional solution to those problems and requirements is fabricating a lamellar silicon iron core. Plenty of silicon iron sheets, hot-rolled and coated, are laminated with insulation layers to assemble one iron core, which is often complicated in geometry to fit the coil winding better. Thus, the traditional method can be costly and time-consuming. Meanwhile, the lamination structure also weakens the structural strength of the core.

The direct energy deposition (DED) technique is also one of the laser-aided additive manufacturing techniques. However, unlike other powder-bed-based techniques, the materials are fed simultaneously with the energy beam to the work surface to form a molten pool. Compared with existing additive manufacturing techniques on soft magnet manufacturing, the DED has distinct advantages: limitless workspace dimensions, an effective feeding mechanism, on-site fabrication feasibility, etc. Its most important and common usage is repairing structures [124] or adding additional material to finalized products [125] but also proven to be practical to fabricate functional materials, such as functionally graded materials composed of stainless steel and nickel alloys, as seen in review [126]. A DED machine is a coaxial system consisting of a material feed nozzle, an energy beam generator, laser or electron, and often another nozzle sending out inert gas to provide shielding. The material feed nozzle deposits material powder onto the work surface, where it melts into a sweeping molten pool by the coaxial energy beam and resolidifies into printed tracks. With a multi-degree-of-freedom robot arm, it can deposit material to any shape or angle on a work surface.

The impacting factors of the laser-based AM technologies are relatively straightforward and less in number than traditional manufacturing methods. Most of them are the preset parameters of the AM process, whose effects on the product microstructures and subsequent influence on performances, mechanical and functional, have been researched in this study. The leading independent variables to tune during DED are the printing parameters set before the whole process, which will directly influence the microstructural and functional properties of the final products. The local optimization work focuses on their control [116].

The major influence of the printing parameters is defect generation, of which the most common is porosity. Porosity is apparently harmful to mechanical strength and thus unwanted and negatively affects magnetic properties, especially permeability. It can also initiate the formation of other defects, such as cracks and balling. Porosity is essentially gases trapped in the printed material during the AM process. Gases are inevitable in the powder, but most can be released during the powder melting process. Factors that result in gas trapped after re-solidification can be classified as inlet and outlet. Inlet factors are the ones which introduce more gases into the material, including powder quality and powder feed mechanism. If the powder particles are too coarse or the shapes are too irregular, the gaps among the adjacent particles can be too large where gases are easier to trap. The powder feed mechanism sprays the powder out of the nozzle with inert gas airflow. When the airflow is overwhelmingly strong, it can also increase the gas trapped in the molten pool and subsequently increase the gas trapped in the solidified parts. Outlet factors prevent gases from getting out. They are the nature of the solidification of the material and other processing parameters, including laser power, scanning speed, feed rate, and hatch spacing. Those factors can either influence the time window during the solidification process when the gas can expel or the path length that the gas must travel before releasing. Additionally, when the energy is insufficient to melt the particles completely, the solid-liquid mixture phase is even higher in the possibility of trapping more gases. Though post-processing techniques, for instance, annealing, have been proved to be helpful in reducing the porosity, they are not omnipotent and often cannot remove all the porosity [127].

Cracking is another important defect that impacts the performance. The high temperature gradient nature of any laser-involving manufacturing method causes the extreme thermal expansion difference and then internal stress in the material, where cracks are nearly inevitable. It happens even more frequently when the material is too brittle. Intertrack and interlayer cracks [128] are the most common when the high-temperature molten pool sweeps through the after-cooling solidified material. Porosity in the material, as mentioned above, and grain boundaries [129] are good tipping points for cracks to start. As another mode of cracking, liquation cracking happens near the fusion line of the previously printed layer [130] that appears to increase while the scanning speed rises. However, cracks can be avoided by carefully controlling the printing parameters. Most cracks happen when energy more than necessary is projected to the material [131], causing too high a temperature gradient. Less or even no crack can be achieved by controlling and optimizing the printing parameters to provide just sufficient energy to the mass.

Balling happens when melted material fails to solidify into layers but instead forms spheres (balls) [132]. It starts with a discontinuous molten pool and accumulates when more and more layers cover it [133]. It is also observed to happen more often when the energy input is excessive [134]. Thus, controlling the parameters is also essential to avoid balling.

Printing parameters have the following impacts on the microstructure and resulting mechanical and magnetic performances of the AM printed samples:

- Low energy input, caused by too low laser power, too high scanning speed or powder feed rate, and too large hatch spacing, can cause incomplete powder melting, which subsequently causes porosity and cracking. Porous and cracked components have poor mechanical strength and low permeability but high electric resistance [135].
- In contrast, high energy input introduces high temperature gradients, which will cause cracking and balling. Its primary impact is on mechanical strength. Thijs, L. et al. reported that high energy density could result in large grain sizes [136], inducing lower coercivity which is undesired.
- Cooling rate, as a general result of all energy input and other parameters, plays a very significant role in material phase change, grain structure, and defect generation. It is controlled by the combination of all the printing parameters, heat convection of the environment, thermal conductivity, and thermal capacity of the material and the substrate. The major goal of controlling and optimizing printing parameters should be finding the optimal cooling rate for the specific material, which is silicon iron in this study.

In summary, laser-based AM printing parameters firstly influence the microstructural features, including grain structure, porosity, cracks, balling, and other potential defects, thereby affecting electric resistance and magnetic domain wall generation and thus the coercivity, permeability, and core loss [137, 138]. Temperature gradients and cooling rate, the values about temperature versus space and temperature versus time, influence the internal stress and grain growth mechanism, which are the fundamental physical reasons that the parameters influence performances [139, 140]. Post-processing techniques, mainly annealing, were also shown to be effective in removing internal stress and continuing grain growth, thus reducing coercivity [141].

Genichi Taguchi developed a system of methods to solve quality control problems [142], among which his innovative theory in the design of experiments is very inspiring. The theory involves robust parameter design, the Pareto principle, elimination of variation in final product quality, and minimization of effects of the noise variables. Here, robust parameter design [143] and the Pareto principle [144] are used in this study to help design an experiment to eliminate defects of the AM printed samples with multiple optimized printing parameters.

This paper investigated the feasibility of applying the direct energy deposition (DED) method to manufacture silicon iron alloy products as soft magnets with better microstructural strength and magnetic properties. The influence of the printing parameters on the product performances were also investigated. Efforts were made to determine the optimal printing process parameters to obtain products with minimal defects and cracks with a set of quality improvement experiments, designed with the inspiration of the Taguchi methods [142]. Samples with similar defect conditions were characterized to further investigate their microstructures and magnetic properties. This study shows that direct energy deposition, as an emerging 3D printing technology, has its potential in manufacturing better functional materials.

4.2 Methods

4.2.1 Experiment Setup

A direct laser melting deposition system was customized to conduct a series of experiments that aims to eliminate the defects and produce the soft magnetic samples, including blocks and rings. As shown in Fig. 1, the powder of Fe-2.5%Si was deposited on the steel substrate, with the laser processing head with coaxial powder feeding device. A continuous wave (CW) fiber laser (YLS-5000 from IPG Photonics) with 1070 nm wavelength and 5 kW maximum output power was used in this experiment. The laser was transmitted through an optical fiber of 600 μm in core diameter to a laser processing head (Laserline YW52), in which the focal length of collimator and focus lens were 150 mm and 250 mm, respectively, and the focal radius of laser beam was 0.5 mm. The laser processing head was mounted on an industry robot (KUKA Robotics KR 16).

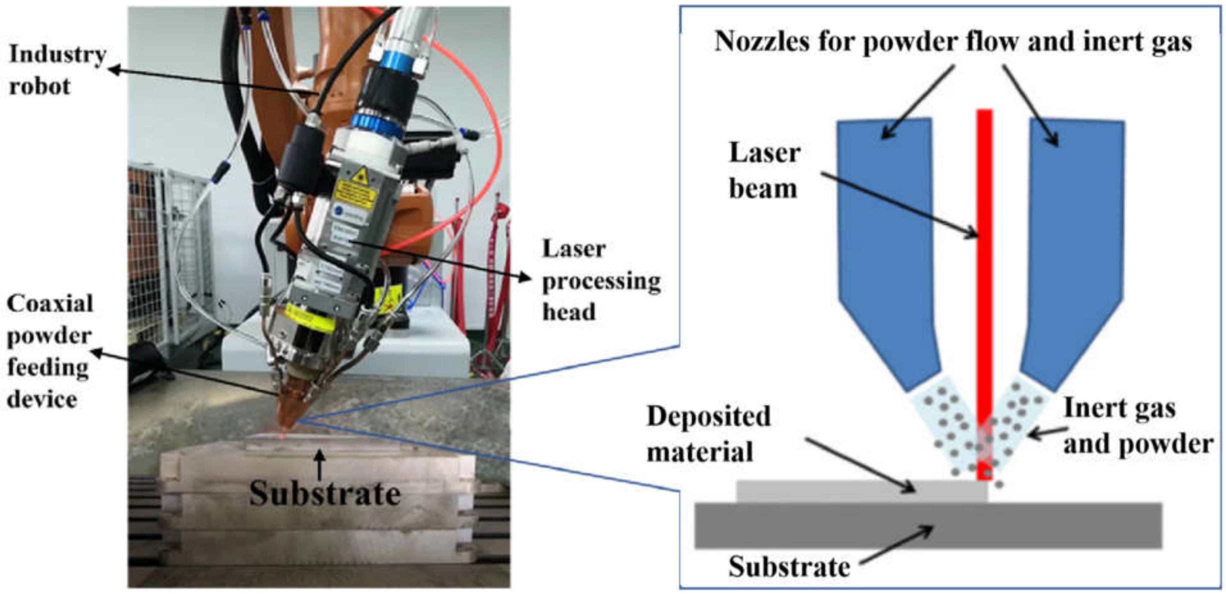

Figure 4.1. The experiment setup and the schematic of a powder nozzle feeding laser welding DED method.

4.2.2 Printing and Optimization

Firstly, a preliminary experiment was conducted to deposit a block up to a height of 15mm. Each layer of the block consisted of a series of parallel cladding tracks with a certain overlap, and the relative cladding direction between each layer was 90°. The block and its longitudinal section were shown in Fig. 2. The section showed that there were large number of unfused holes on the longitudinal section of sample. Fig. 2 also showed that there were large, stripe-shape holes between each crack, and most of the long sides of them were all parallel to the build direction. It indicated that the unproper process parameters, including lack of laser energy input and the excessive hatch spacing, should cause these defects. These unfused holes would severely reduce the magnetic permeability and damage the mechanical strength of the final products. Therefore, a series of quality improvement experiments inspired by Taguchi methods [142] was designed. In the parameter design phase, the quality characteristic is determined to be a value to quantify the defect happening frequency, introduced in the following contents. The control factors are undoubtedly the printing parameters. An extensive set of factorial screening experiments was designed to analyze the effects of four different factors on the quality characteristic. To test every possible combination with four levels, 4^4= 256 runs must be done. Thus, robust parameter control was applied to reduce the number to 32 by fractioning the matrix with the Pareto principle. And then, the parameters were optimized based on the statistical analysis results to obtain samples with few defects. The in-detailed procedure is shown in the following contents.

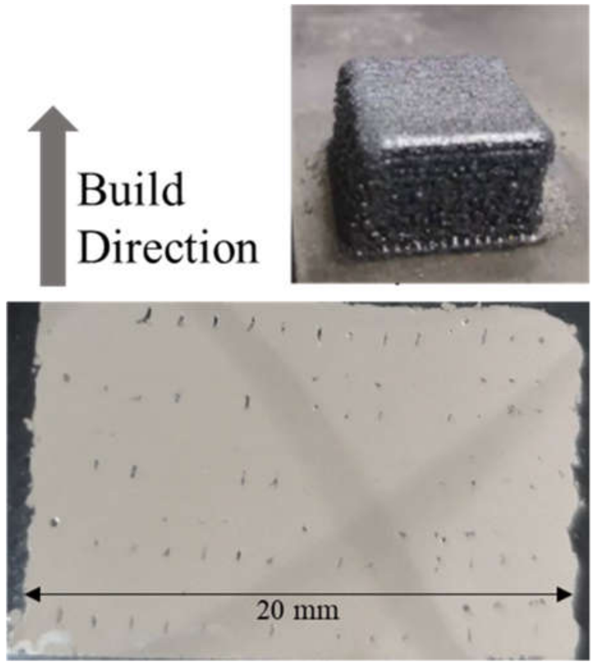

Figure 4.2. Longitudinal section of the sample in preliminary experiment

In the next step, a two-level and four-factor (process parameter) partial factorial screening experiment was designed to figure out the important factors that caused the formation of the unfused defects. This There were four types of process parameters that mainly affected the quality and density, including laser power, scanning speed, powder feed rate and hatch spacing. These were selected to conduct this screening experiment. The two levels, which vary widely (>=50%), were selected to improve the screening effect. The *rate of lack of fusion*, as the characteristic of the quality result, was calculated by the rate of the area of all defects to the area of entire longitudinal section of the sample. In order to compare the density of defects at the same cladding situation, all blocks were deposited with the same number of layers and the same length of single cladding track, and their longitudinal sections were shown in Fig. 3. Meanwhile, detailed data of parameters and results of eight samples were shown in Table 1.

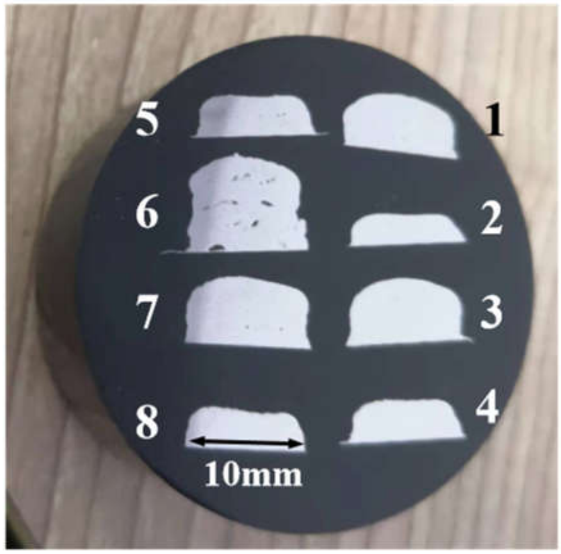

Figure 4.3. Longitudinal sections of sample in the partial-factor screening experiment

Table 4.1. Parameters and results of screening experiment

Item	Laser power (W)	Scanning speed (mm/s)	Powder feed rate (g/s)	Hatch spacing (mm)	Rate of lack of fusion (%)
1	1400	8	6.93	0.8	0.6860
2	1400	12	4.62	0.8	0.5504
3	1400	8	4.62	1.2	0.1742
4	900	8	4.62	0.8	0.7200
5	900	12	4.62	1.2	0.9813
6	900	8	6.93	1.2	2.1600
7	1400	12	6.93	1.2	0.5880
8	900	12	6.93	0.8	0.9813

The Pareto chart of the standardized effects was plotted by Minitab, shown as Fig. 4, after calculating the rate of lack of fusion and analyzing the effects of all the factors of the screening experiment on the rate of lack of fusion. The Minitab calculated standardized effects by t-statistics that test the null hypothesis that the effect of the factor is 0. The absolute value of t obtained by t-statistics test (standardized effects) of each effect was taken as abscissa. According to the selected significance level α (0.4), which is the difference between the confidence level and 1, the critical value of t was given, and effects whose absolute value exceeds the critical value would be selected for further comprehensive-factorial experiment.

Hence the laser power and the powder feed rate are shown to have the most significant influence on the formation of unfused defects. Meanwhile, the interaction of laser power and hatch spacing also affected it greatly. Therefore, four levels of laser power, powder feed rate and two levels of hatch spacing were designed to further set in the comprehensive-factorial experiment.

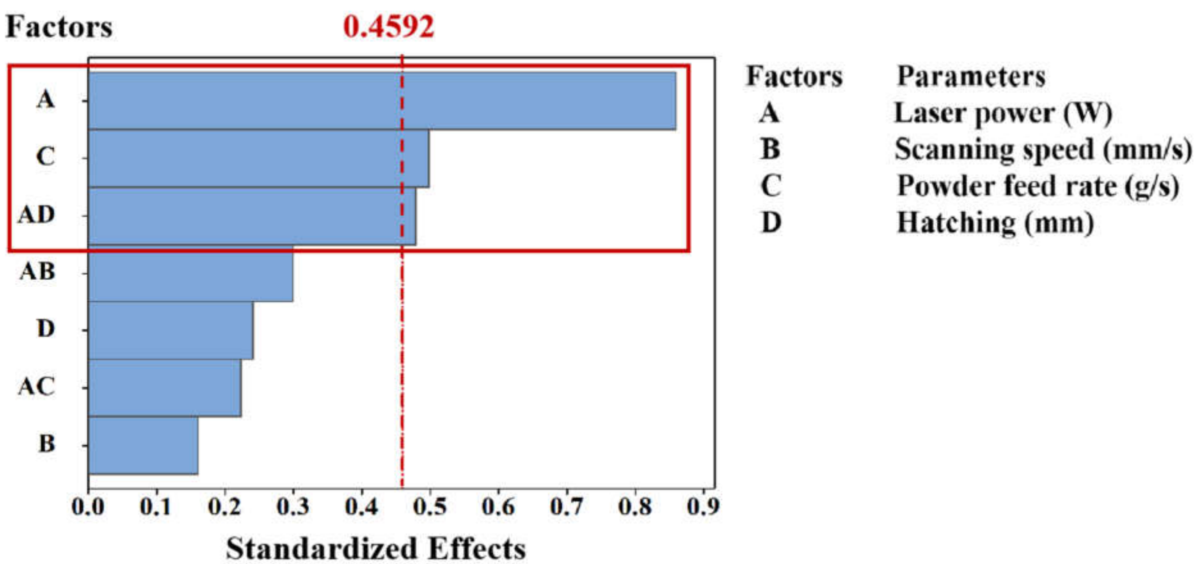

Figure 4.4.The Pareto chart of the standardized effects of all the factors on the rate of lack of fusion, generated by Minitab, α=0.4.

Furthermore, the main effect diagram showed whether the major factors had a really significant effect on the response (rate of lack of fusion), as shown in Fig. 5. The regression lines of factors laser power and powder feed rate were quite steep, which meant these two factors indeed had a great influence on the response. And the major factor of hatch spacing also had a steep regression line, so this factor should be considered in the further experiment. By contrast, the regression line of scanning speed factor was relatively flat, so its main effect was not significant. In order to achieve the lowest rate of lack of fusion, the higher laser power, the lower value of powder feed rate and hatch spacing should be considered. This indicated that the combination of parameters including laser power 1400W, powder feed rate 4.62g/s and hatch spacing 0.8mm has the lowest formation rate of unfused defects. Therefore, the parameters around of them were selected for the further experiment, which included laser power (1300W, 1400W, 1500W, 1600W), powder feed rate (3.08g/s, 3.85g/s, 4.62g/s, 5.39g/s) and hatching spacing (1.0mm, 1.2mm). And the detailed sets of parameters for the comprehensive-factorial experiment were shown in Table 2. The numbering followed the order generated by the multiple linear regression function of Minitab.

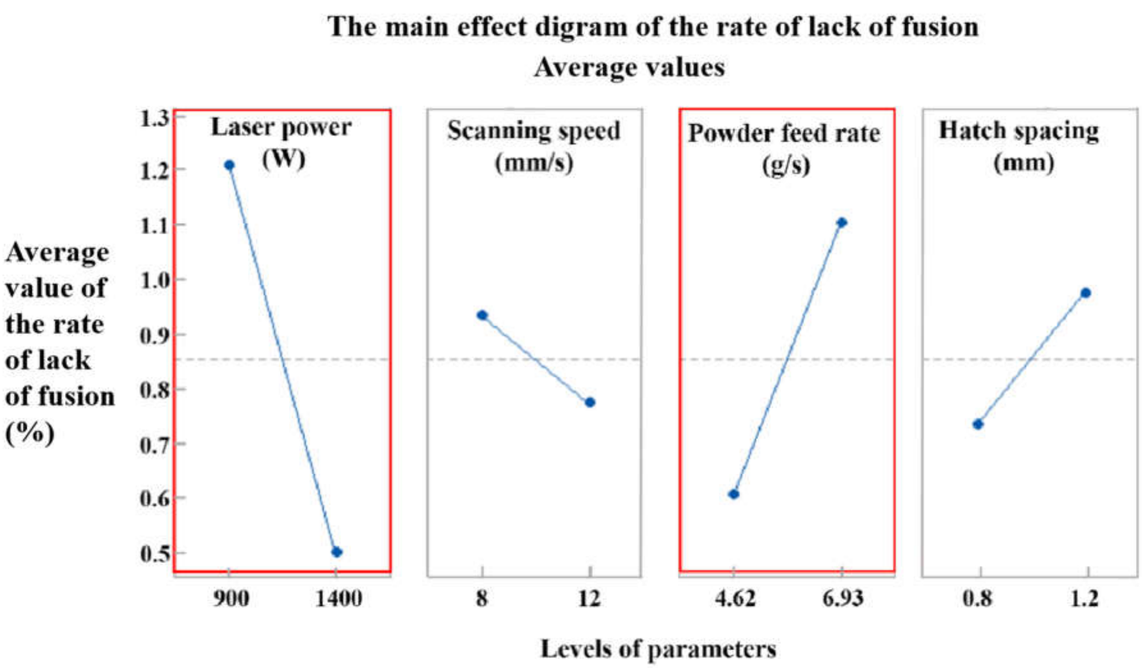

Figure 4.5. The main effect diagram of the rate of lack of fusion.

Table 4.2. Combinations of parameters of comprehensive factorial experiment

Laser power (W)	Powder feed rate (g/s)	Hatch spacing (mm)	Scanning speed (mm/s)	Rate of lack of fusion (%)	Numbering in Fig. 6(e)	Pattern Group in Fig. 6(a-d)
1300	3.08	1.2	9	0.3733	1	A
1300	3.08	1	9	0.0123	**17**	D
1300	3.85	1.2	9	0.0083	5	D
1300	3.85	1	9	0.0473	14	C
1300	4.62	1.2	9	0.2139	19	B
1300	4.62	1	9	0.1047	9	B
1300	5.39	1.2	9	0.1602	28	B

1300	5.39	1	9	0.2617	16	B
1400	3.08	1.2	9	0.0298	29	C
1400	3.08	1	9	0.0133	**31**	D
1400	3.85	1.2	9	0.4939	32	A
1400	3.85	1	9	0.0166	18	D
1400	4.62	1.2	9	0.0943	4	B
1400	4.62	1	9	0.2254	12	A
1400	5.39	1.2	9	0.0786	15	B
1400	5.39	1	9	0.0349	23	C
1500	3.08	1.2	9	0.0259	26	C
1500	3.08	1	9	0.0198	2	D
1500	3.85	1.2	9	0.0624	24	B
1500	3.85	1	9	0.0376	3	C
1500	4.62	1.2	9	0.0625	13	B
1500	4.62	1	9	0.0164	7	D
1500	5.39	1.2	9	0.0499	20	C
1500	5.39	1	9	0.0079	**21**	D
1600	3.08	1.2	9	0.0365	25	C
1600	3.08	1	9	0.481	11	A
1600	3.85	1.2	9	0.1121	8	A
1600	3.85	1	9	0.296	30	A
1600	4.62	1.2	9	0.0318	27	C
1600	4.62	1	9	0.1085	10	A
1600	5.39	1.2	9	0.0119	6	D
1600	5.39	1	9	0.042	22	C
1400	3.08	1	6	N/A	33*	N/A

1400	3.08	1	12	N/A	34*	N/A

* Additional sets of parameters for the next round of experiments

With the combinations of parameters listed in table 2, it is clear that the factor effects calculated in the last round of the experiment were still correct. The laser powers and powder feed rates were also the dominating parameters. While the laser power increased, the powder feed rate had to rise to keep the rate of lack of fusion low. But that was only a trend. It was also observed that samples with similar ratios of laser power to powder feed rate have significantly different performances, for example, sample 1 and sample 17.

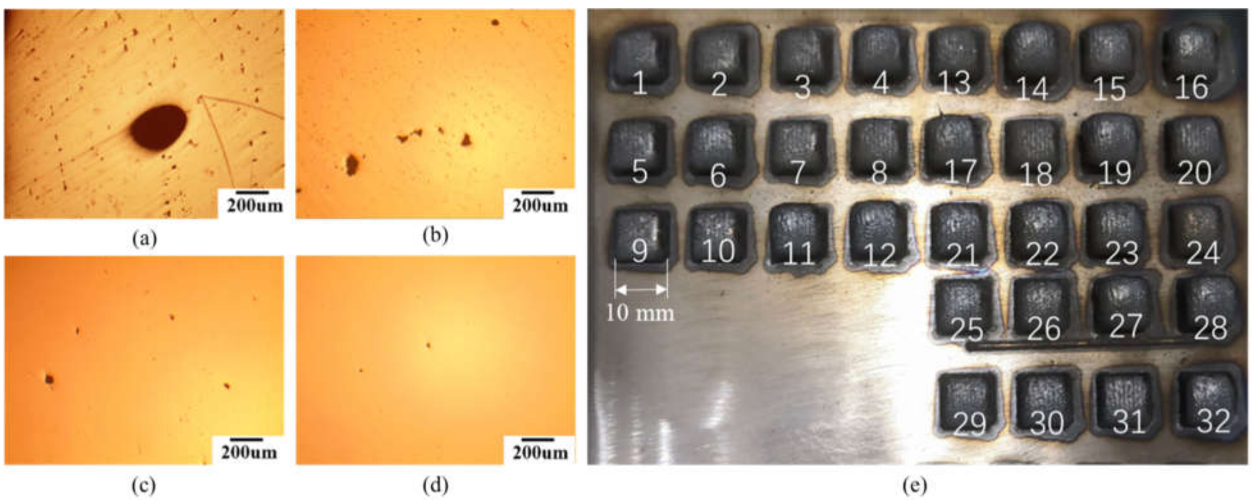

Figure 4.6. The optical microscope images of the four types of defect patterns and (e) the photo of all results of the comprehensive experiment

In order to explore the best density and the lowest rate of lack of fusion, the comprehensive-factorial experiment was conducted. The parameters and results of comprehensive experiment with metallographic microscope has been reported in Fig. 6. The results showed that there are four typical examples of defect patterns caused by parameter combinations, which are separated according to the rate of lack of fusion and pores, and the shape and size of holes. Fig. 6(a) showed the type A defect pattern. The type A had the highest average rate of lack of fusion and pores (>0.1%), and the pores were also very huge with above 200um of the diameter. Meanwhile, the shape of holes was circular and the edge of them were smooth. The parameters with high laser power, low powder feed rate and small hatch spacing always occurred in this type. The Fig. 6(b), type B showed that there was second highest average rate of lack of fusion and pores (>0.05%). However, compared with type A, the shape of holes in type B were irregular and there were burrs around the edge. The level of powder feed rate and hatch spacing were always relatively high, whereas the level of laser power was low. The Fig. 6(c), type C showed a low average rate of lack of fusion and pores (<0.05%), and there were small pores on the metallographic microscope. Finally, in the Fig. 6(d), the lowest average rate of lack of fusion and pores (<0.02%) occurred in this group. There were almost no pores and unfused holes on the longitudinal metallographic microscope. The combination of parameters for the production would be selected from the type D, shown in Fig. 6(d). The lack of fusion and pattern group information was also list in Table 2 in blue.

At first glance, the values in the table do not show any apparent trends or correlations between the printing parameters and the characteristic, which is the rate of lack of fusion. However, based on physical common sense, strong enough laser power input and sufficient powder supply should be present to achieve less defect generation [145]. Therefore, regression analysis was done to further study their influence and association.

Linear regression between the rate of lack of fusion and all three original parameters gave the equation:

$$\begin{aligned}\text{Rate of lack of fusion}/\% \\ &= 0.318 - 0.0001\ \text{Laser Power/W} - 0.0204\,\text{Powder Feed Rate}/\left({}^{g}/_{s}\right) \\ &+ 0.0370\,\text{Hatching/mm}\end{aligned}$$

Their P-values are respectively 0.621, 0.485, and 0.883. And their correlation coefficients to the rate of lack of fusion are respectively -0.093, -0.132, and 0.028.

Then two factors calculated from the original parameters were analyzed.

The area energy density was obtained by laser power divided by the product of scanning speed and hatch spacing. The equation of the linear regression is:

$$Rate\ of\ lack\ of\ fusion\ (\%) = -0.0082\ Area\ Energy\ Density/(J/mm^2) + 0.1116$$

The P-value is 0.7430. The correlation coefficient of the two variables is only -0.0603.

The linear energy density was calculated by dividing laser energy by scanning speed. The equation of the linear regression is:

$$Rate\ of\ lack\ of\ fusion\ (\%) = -0.0126\ Linear\ Energy\ Density/(J/mm) + 0.1116$$

The P-value is 0.6110. The correlation coefficient of the two variables is only -0.0934.

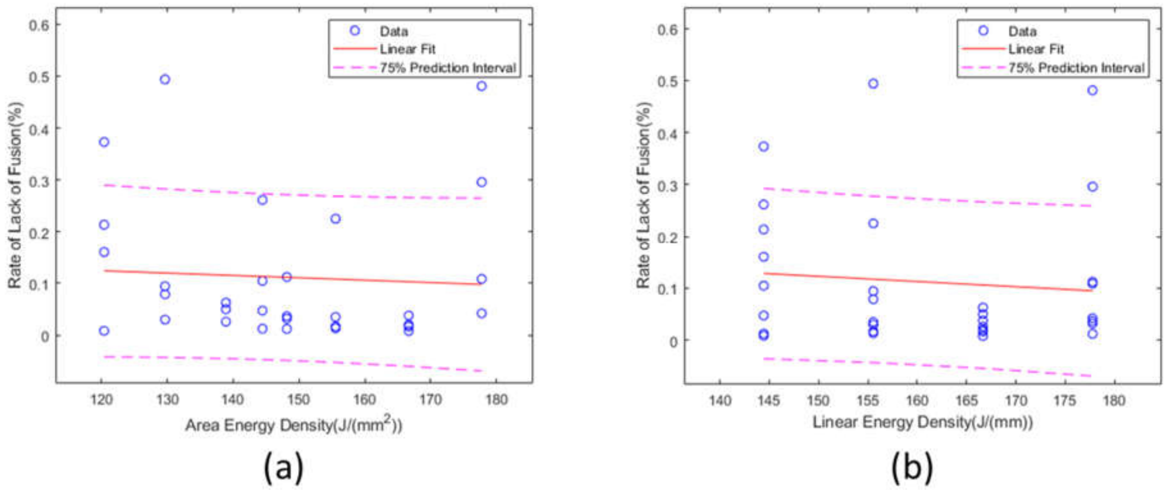

Figure 4.7. Plots of linear regression between the rate of lack of fusion and (a) the area energy density and (b) the linear energy density.

Fig. 7 is the plot of the two equations. Together with the wide 75% prediction interval, both fits looked weak.

As a conclusion of all the regression analysis, the trends of the rate of lack of fusion are:

1. Higher laser power and energy density can decrease the rate of lack of fusion.

2. Larger powder feed rate can decrease the rate of lack of fusion and is slightly more critical than laser power.

3. Wider hatching will increase the rate of lack of fusion but has little correlation.

Finally, the combinations of parameters of the number of #17, #21, #31 have been selected to print the samples for property characterization, one cuboid and one ring for each set. In addition, the velocity of 6 mm/s and 12 mm/s with same parameters as #31 except velocity has been selected to produce #33 and #34, respectively. The cuboid samples were cut into halves to expose longitudinal sections and prepared for the further characterizations, as shown in Fig. 8. There are no obvious macroscopic defects, such as pores and unfused holes on all longitudinal sections of samples. No further post-processing was done.

Figure 4.8. Longitudinal sections of samples #17, #21, #31, #33, and #34.

Furthermore, a low-magnification optical microscope image from the work of Sangwoo Nam et al. [146] is shown below, compared with the similar-magnification image of the longitudinal section of sample #17. It could be seen that sample #17 has much less pores and cracks, except the cutting scratches were not clearly polished off.

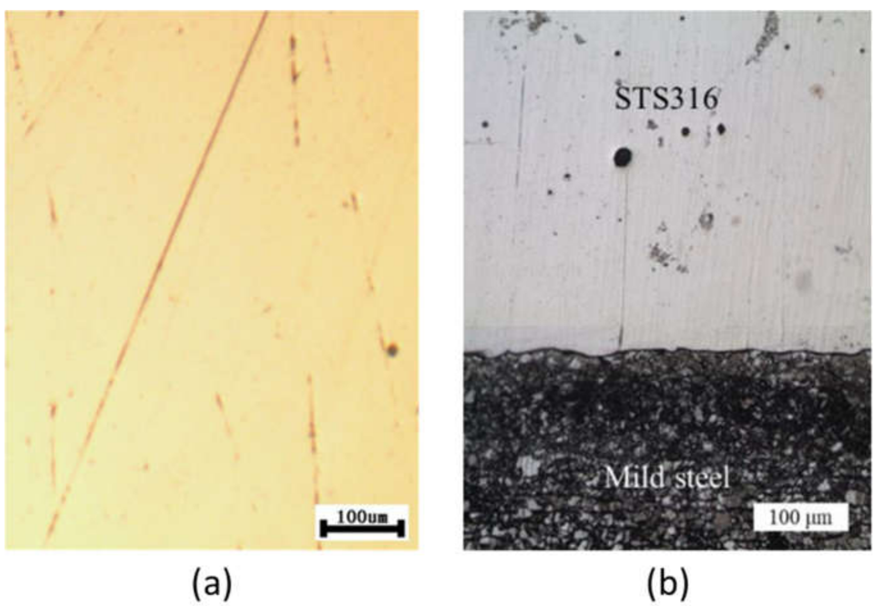

Figure 4.9. (a)Low magnification microscope image of the sample #17 compared with (b) DED cladding of STS316 on the mild steel [146].

The Scanning Electron Microscope (SEM) analysis on those samples was carried out with the JSM-IT500 InTouchScope™ Scanning Electron Microscope from JEOL Ltd. Five of the best samples were numbered and examined. EDS spectra were taken to analyze the defects that appeared in the SEM images.

4.3 Characterization of microstructures and magnetic properties

The samples of printed silicon iron in a rectangular shape were mechanically polished before being etched with 3% nitric acid-isopropyl alcohol solution for 2 minutes. After nitric etching, the samples were thoroughly cleaned with isopropyl alcohol for any following optic and electron-based characterization.

4.3.1 Optical Microscopy

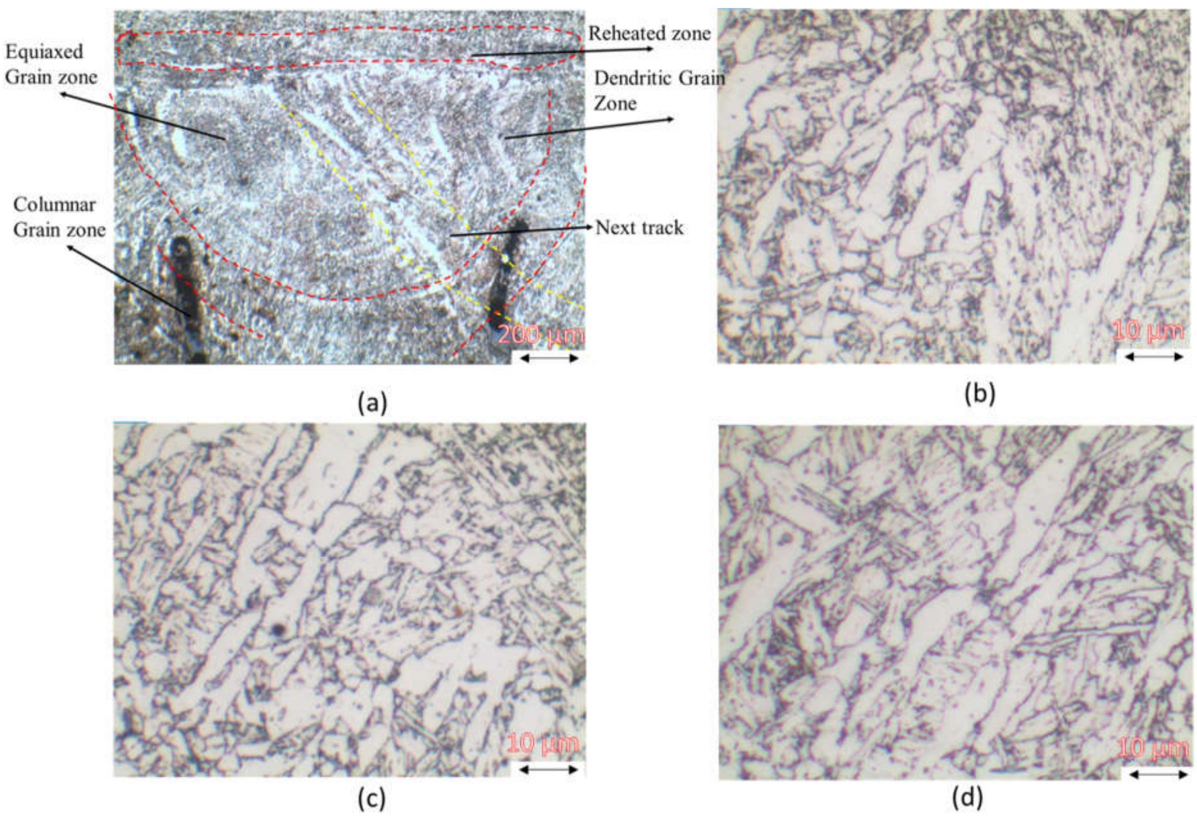

Figure 4.10. The optical microscope images of (a) the cross section of molten pool tracks with a magnification of 100 times, (b) the sample #17 with a magnification of 2000 times, (c) the sample #21, and (d) the sample #31.

Fig.10(a) displays the optical micrograph of the cross-section of the early sample, showing the different solidification processes caused by the marching molten pool and overlapping of the adjacent tracks. As a result of the radial heat transfer nature from the laser focal point, the thermal conditions, especially temperature gradients, are highly diverse along with the heated material. Thus, the re-solidified silicon iron showed different metallographic forms at different points. The equiaxed phases could be seen in the central area near the focal point. Dendrite patterns could be seen in the highly heated areas. The edge of the molten pool appeared columnar, showing a lower and directional temperature gradient. Then the next overlapped track would reheat and rebuild them all over again. In Fig.9(b-d), the non-equiaxed zones were magnified to show the alignment of columnar and dendrite grains caused by the drastic temperature drop after the molten pool sweeping by.

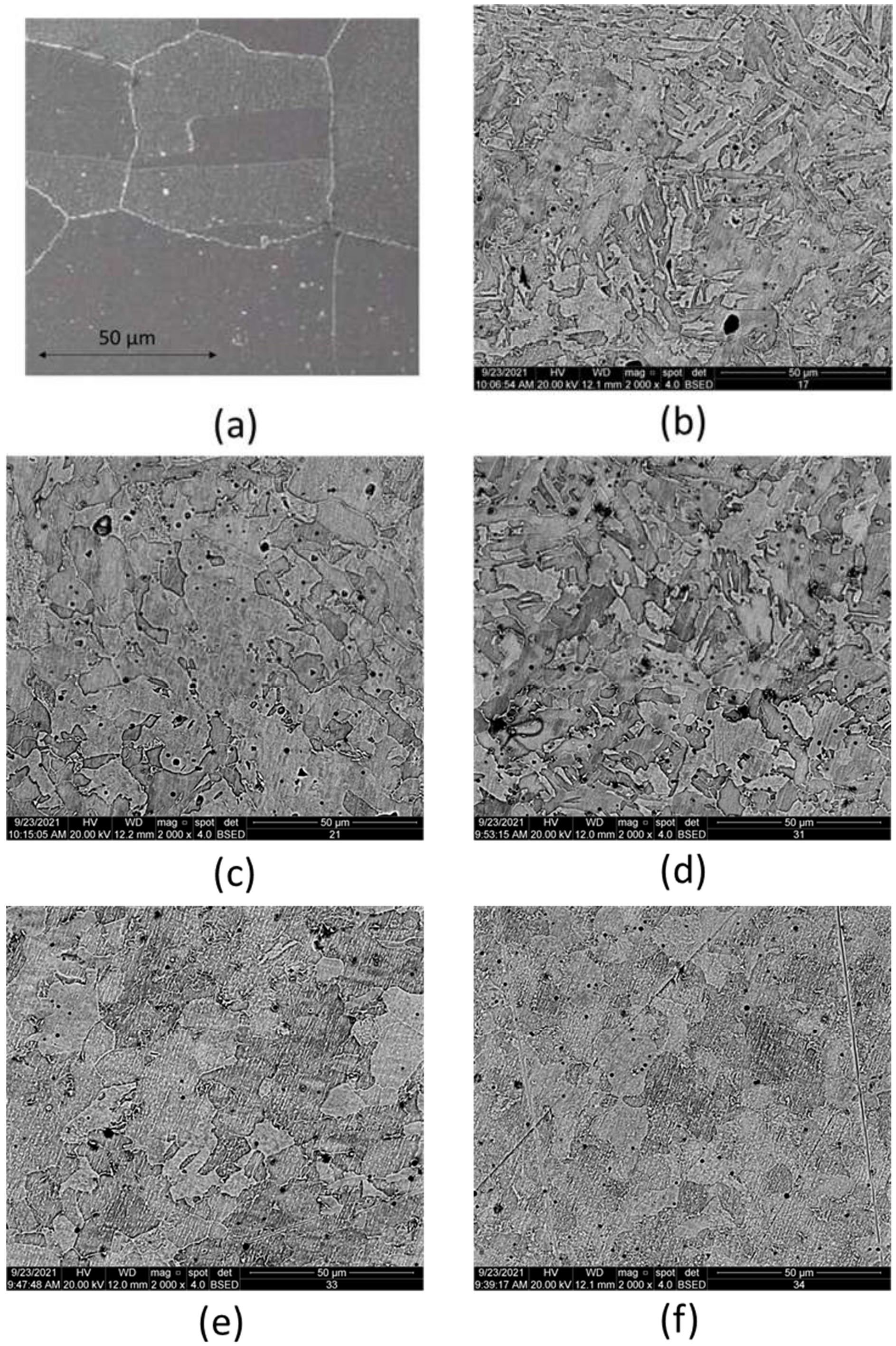

Figure 4.11. Scanning electron microscope images of (a) traditionally manufactured silicon iron alloy [147], (b) sample #17, (c) sample #21, (d) sample #31, (e) sample #33, and (f) sample #34. The scales are displayed in images.

4.3.2 Scanning Electron Microscopy (SEM)

Fig.11 shows the differences in surface appearance for five different samples with different printing parameter sets, listed in Table 3. Compared with the traditionally fabricated silicon iron alloy [147], the DED printed samples show exceedingly smaller grain sizes, as predicted. Especially sample 31 (Fig.9d) and sample 34 (Fig.10f), which have the highest energy to mass ratios, presented grain sizes of around 10~30 micrometers.

However, it had been believed sample 34 (Fig.10f) should have smaller grain sizes since it was fabricated with a higher scanning speed thus a higher cooling rate. But the SEM images did not support the hypothesis. It is because accelerating scanning speed from 9 mm/s to 12 mm/s did not change so much on the cooling rate compared with changing the laser power level.

Moreover, compared with Fig.9(a) taken in the preliminary tests, all of the SEM images show no significant different grain patterns. It is believed that the optimized parameters result in the dominance of the reheating effect. Thus, most grains turned out to be equiaxed.

Table 4.3. The printing parameters of the characterized samples presented in Fig.9.

Sample Number	Laser Power (W)	Scanning Speed (mm/s)	Powder Feeding Rate(g/s)	Energy to Mass Ratio (J/g)	Linear Energy Density (J/mm)
17 (b)	1300	9	3.08	422.08	144.44
21 (c)	1500	9	5.39	278.29	166.67
31 (d)	1400	9	3.08	454.55	155.56
33 (e)	1400	6	3.85	363.64	233.33
34 (f)	1400	12	3.08	454.55	116.67

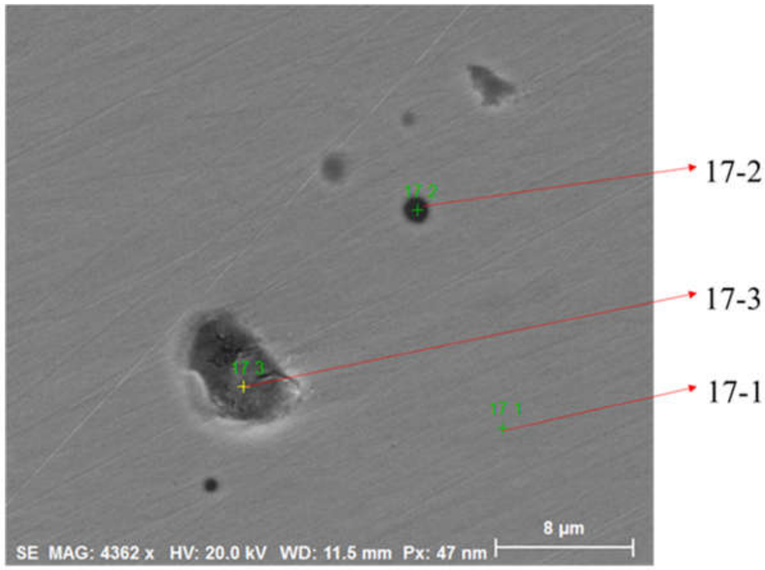

(a)

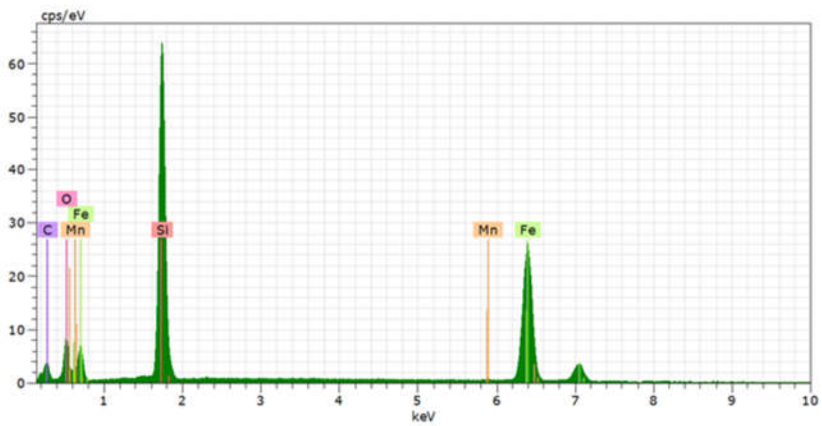

(b)

Figure 4.12. (a) The locations of the three spectrum sample points and (b) their signal strengths on spectrum.

Table 4.4. The atomic percent of each sample point.

Spectrum	C	O	Al	Si	Mn	Fe
17-1	-	-	-	2.69	0.44	96.87
17-2	-	42.52	6.62	19.00	2.38	29.48
17-3	37.82	19.61	-	24.07	-	18.50

The EDS spectrums of the existed defects were shown in Fig.12 and quantitative result was shown as Table 4. The 17-1 result was the general contents, which showed the component of the applied silicon iron (2.5% Si, 0.4% Mn, balance Fe). The point 17-2 and point 17-3 of probed areas represented two types of impurity defects appearing on all of the printed samples. The spectrums showed that the most common defects, the round-shaped dark areas, were mainly oxides, including SiO2 and Fe_xO_y. Aluminum detected at that spot should be the remaining of the abrasives. The largest defects were consisted of mostly carbon which made sense for any iron products where carbon was not particularly taken care of.

4.3.3 Magnetic Characteristics

The samples of rings were prepared for the measurement of magnetic properties, as shown in Fig.13. The prepared rings have a dimension of OD ≈ 54 mm, ID ≈ 36 mm and height is about 6~8 mm. To measure the magnetic properties, primary (100 turns) and secondary (100 turns) windings are placed around the sample core as shown in the figure below. Coercivity and core loss was then measured using an AC/DC hysteresisgraph system under conditions of B=1.5T@50Hz and B=1.0T@400Hz. The results are shown in Table 5.

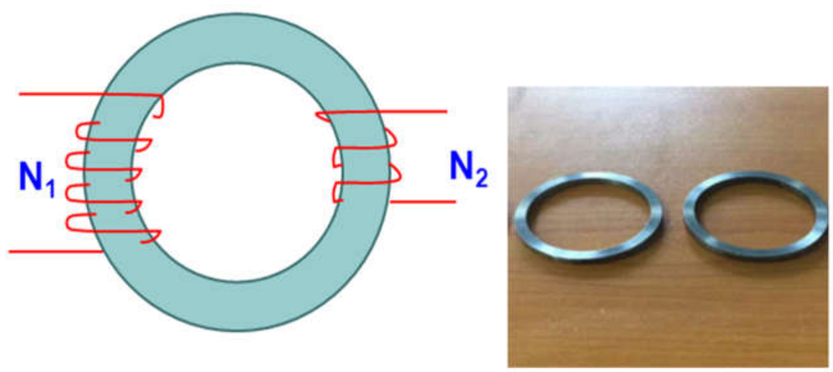

(a) (b)

Figure 4.13. (a) Magnetic measurement schematic diagram. N1 is the primary winding and N2 is the secondary one. (b) And the prepared sample rings for the magnetic characterization.

Table 4.5. The magnetic characterization results

Sample Number	Laser Power (W)	Scanning Speed (mm/s)	Powder Feeding Rate(g/s)	Coercivity Hc (A/m)	Core loss Pc (1.5T @50Hz) (W/kg)	Core loss Pc (1T @400Hz) (W/kg)

17	1300	9	3.08	2662	106	1521
31	1400	9	3.08	3525	142	1980
21	1500	9	5.39	2913	108	1753
33	1400	6	3.85	3087	123	1751
34	1400	12	3.08	3094	124	1736
Pham et al 2018 (0.25% Boron doped)[148]*				~10000	~10	100~1000
Tiismus et al 2021 [149]**				500~2500	30~200	
Ouyang et al 2019 (Fe-6.5% Si high silicon steel)[150]				~1000	~5	>50

* Ink jet printing

** Laser fusing powder-bed printing

The magnetic characterization results showed that the different printing parameters have a significant influence on the final magnetic properties. The sample 17 with 1300 W laser power, 9 mm/s scanning speed, and 3.08 g/s feeding rate showed the lowest coercivity and lowest core loss at each condition. As benchmarks for the additive manufactured results, Pham et al. applied the binder jet printing method with Fe91Si9 doped with 0.25% Boron (95.02% Fe, 4.73% Si, and 0.25% B by mass) in 2018 [148]. Tiismus et al. used laser fusing powder-bed printing on silicon iron powders with 3.7%wt Si in 2021 [149]. Correspondingly, on the traditional industry side, Ouyang et al. published a review paper that summarized the high silicon steel (6.5%wt Si) performance in 2019 [150]. All those data were listed in Table 5 along with our results to compare with.

Compared with literature results [148, 149], the samples showed similar level coercivity and core loss. However, compared with industrialization level traditionally fabricated silicon iron with 6.5% silicon, all the three additive manufactured products, including [26], [27] and this paper, showed interior properties. As suggested by Ouyang et al. [150], one reason might be because the microstructure advantages of additive manufactured products could not yet beat the laminated sheets, and defective nature of them affect the coercivity and other magnetic properties.

4.4 Chapter Conclusion

The direct energy deposition (DED) method was proved feasible for additive manufacturing of soft magnetic material. Sample of silicon iron rings and bulks were printed and characterized both for their microstructures and magnetic properties. The following concluding remarks were drawn:

- Different sets of the DED printing parameters, including feeding rate, scanning speed, track overlapping ratio, were designed and optimized via several rounds of quality control experiments to reduce the unfused defects. The design of the experiment is inspired by the Taguchi methods.
- With the optimized parameter sets, five pairs of rings and bulks were printed and showed decent quality. Few defects and flaws were found in them.
- The samples were examined by optical microscopy and scanning electron microscopy. All of them showed acceptable numbers of defects. The microstructure of the samples consisted of a uniform and equiaxed structure.
- Their magnetic properties were characterized. The results showed similar level coercivity and core loss as other additive manufactured products. However, it is yet worse than traditional products in terms of magnetic performance.

In conclusion, DED additive manufacturing is a promising method for soft magnet manufacturing. It has all the merits same as other additive manufacturing methods such as fast prototyping, geometric capability, on-time processing, and so on. It also has its distinct advantages including large fabrication dimension and on-site availability. However, compared with soft iron products manufactured traditionally, the DED fabricated ones are still inferior in terms of magnetic properties, as a result of smaller grain sizes. That fact inspires us to further study how to take the advantage of the microstructural optimization nature of the laser-based technologies to beat the time consuming and high-cost traditional lamination building method.

5 Chapter 5 Conclusion and Future Work

5.1 Conclusions

This dissertation explored interdisciplinary topics at the intersection of thermoelectric energy systems, additive manufacturing, and radiation-resilient technologies. By integrating advances in thermoelectric materials, energy harvesting systems, and innovative manufacturing techniques, it addresses critical challenges in sustainable energy, monitoring systems, and fabrication processes. The key contributions of this work span both theoretical and experimental domains, reflecting a comprehensive approach to solving real-world problems in energy and manufacturing sciences.

5.1.1 Innovations to Thermoelectric Energy Systems and Monitoring Technologies

One of the most significant contributions of this dissertation is the development and demonstration of a **self-powered through-wall data communication system** designed for the harsh environment of spent nuclear fuel canisters. This work demonstrated the feasibility of using thermoelectric energy harvesting to power data communication systems under extreme conditions of temperature, radiation, and longevity. Key findings include:

1. **Thermoelectric Material Resilience:** Experimental results demonstrated that thermoelectric materials can withstand gamma radiation doses up to 124 MRads while maintaining sufficient power output (94 mW in year 5 and 46 mW in year 55). This resilience validates the use of these materials in long-term monitoring applications.

2. **High-Temperature, Radiation-Tolerant Electronics and Through-Wall Communication:** (*credited to Oak Ridge National Lab and University of South Texas*) The transition from BJT to JFET-based circuit designs resulted in systems capable of functioning under TIDs exceeding 2 MRads, with ongoing tests for >100 MRads. This innovation ensures reliable performance in high-radiation environments. Ultrasonic data transmission systems were successfully fabricated and tested under both room temperature and elevated temperature conditions, as well as in gamma radiation environments. The system demonstrated resilience to radiation doses exceeding 101 MRads TID.

3. **Integrated System Demonstration:** A complete system integrating energy harvesting, shielding, and communication electronics was demonstrated at high temperatures. The system survived up to 195°C, revealing limitations in current PCB materials and adhesive solutions, prompting recommendations for future improvements.

4. **Radiation Shielding:** The design and simulation of tungsten-boron carbide-based shielding provided effective gamma and neutron radiation protection, ensuring the viability of the monitoring system over the 55-year service life of nuclear canisters.

This work not only advances the field of thermoelectric energy systems but also establishes a foundation for applying these technologies in extreme environments. The outcomes highlight the potential of interdisciplinary approaches to address sustainability challenges in nuclear energy management.

5.1.2 Contributions to Additive Manufacturing for Thermoelectric and Soft Magnetic Materials

Another significant focus of this dissertation is the application of **additive manufacturing (AM)** techniques to improve the fabrication of thermoelectric materials and soft magnetic components. These efforts leveraged both experimental and modeling approaches to address long-standing challenges in material properties and production efficiency.

1. **Selective Laser Melting (SLM) for Thermoelectric Powders:**
    - A comprehensive 3D model simulated the convection-diffusion processes during the SLM fabrication of Mg2Si thermoelectric powders with embedded Si nanoparticles. This simulation revealed critical insights into the shrinkage of the powder bed, the morphology of the melting pool, and the aggregation of nanoparticles.
    - Results showed that high scanning speeds improve temperature uniformity, whereas increased energy input enhances the size and shape of the melting pool. However, nanoparticle aggregation at the melt pool boundaries was identified as a factor that may degrade material performance.
    - These findings provide actionable insights for optimizing SLM parameters, enabling the production of thermoelectric materials with enhanced performance and reduced defects.
2. **Direct Energy Deposition (DED) for Soft Magnetic Materials:**
    - The feasibility of DED for fabricating silicon iron rings and bulk components was demonstrated. Through systematic parameter optimization inspired by Taguchi methods, the study achieved high-quality samples with minimal defects.
    - Microscopic analyses revealed a uniform and equiaxed microstructure in the fabricated components. Magnetic property testing showed performance comparable to other AM methods but inferior to traditional manufacturing.
    - The findings underscore the promise of DED for fast prototyping and large-scale fabrication while emphasizing the need for further work to optimize microstructures for improved magnetic performance.

5.2 Broader Implications and Future Directions

The interdisciplinary nature of this dissertation bridges gaps between energy science, material engineering, and advanced manufacturing. By integrating modeling, experimentation, and system-level optimization, this work lays the groundwork for innovative solutions to pressing global challenges.

1. **Sustainability and Energy Efficiency:** The research advances the development of self-sustaining systems powered by thermoelectric energy harvesting, particularly in extreme environments. These technologies could be applied to other domains, such as space exploration, remote monitoring, and disaster response.

2. **Additive Manufacturing in Energy Applications:** The combination of AM techniques with material science offers new opportunities for tailoring microstructures and enhancing properties of thermoelectric and magnetic materials. These findings inspire further exploration into hybrid manufacturing processes and the use of nanomaterials to achieve superior performance.

3. **Radiation-Resilient Systems:** The results highlight the importance of designing systems that can operate reliably under extreme conditions. Future work could explore alternative materials and electronics that extend operational limits beyond the demonstrated temperature and radiation thresholds.

4. **Modeling and Simulation:** The computational models developed in this dissertation provide a foundation for simulating complex thermal, mechanical, and material interactions during AM processes. Expanding these models to incorporate additional phenomena, such as phase transformations and stress-strain relationships, could lead to deeper insights and broader applications.

5. **Interdisciplinary Collaboration:** The research presented here demonstrates the power of integrating insights from multiple fields, including thermoelectrics, radiation physics, materials science, and manufacturing. This approach could serve as a model for addressing other multifaceted challenges in science and engineering.

5.3 Final Remarks

This dissertation contributes to the understanding and advancement of thermoelectric energy systems and additive manufacturing technologies. The findings emphasize the importance of interdisciplinary collaboration in tackling complex problems, offering innovative solutions with real-world applicability. By addressing challenges in energy sustainability, extreme-environment monitoring, and advanced material fabrication, this work paves the way for future research and development in these critical areas.

The journey from theory to practical demonstration underscores the transformative potential of thermoelectric and AM technologies. While adequate progress has been made, the findings also highlight opportunities for further innovation, particularly in material optimization, manufacturing scalability, and system resilience. Future efforts in these directions hold the promise of advancing both science and industry, contributing to a more sustainable and technologically advanced world.

6 Reference

[1] Seebeck, T. J., 1895, Magnetische polarisation der metalle und erze durch temperatur-differenz, W. Engelmann.
[2] Goldsmid, H., and Goldsmid, H., 1964, "Applications of thermoelectric refrigeration," Thermoelectric Refrigeration, pp. 210-223.
[3] Peltier, J., 1834, "Investigation of the heat developed by electric currents in homogeneous materials and at the junction of two different conductors," Ann. Chim. Phys, 56(1834), p. 371.
[4] Rowe, D. M., 2018, CRC handbook of thermoelectrics, CRC press.
[5] Thomson, W., 1857, "4. on a mechanical theory of thermo-electric currents," Proceedings of the Royal society of Edinburgh, 3, pp. 91-98.
[6] Ioffe, A. F., 1958, Semiconductor Thermoelements, And, Thermoelectric Cooling, Infosearch.
[7] Hicks, L. D., and Dresselhaus, M. S., 1993, "Effect of quantum-well structures on the thermoelectric figure of merit," Physical Review B, 47(19), p. 12727.
[8] Suryanarayana, C., 2001, "Mechanical alloying and milling," Progress in materials science, 46(1-2), pp. 1-184.
[9] Groza, J. R., and Zavaliangos, A., 2000, "Sintering activation by external electrical field," Materials Science and Engineering: A, 287(2), pp. 171-177.
[10] Scherrer, H., Rowe, D., Kajikawa, T., Matsubara, K., Issi, J.-P., Goldsmid, H. J., Bhandari, C. M., Burkov, A. T., Zaitsev, V. K., and Fedorov, M. I., 2018, "Thermoelectrics Handbook: Macro to Nano."
[11] Venkatasubramanian, R., Siivola, E., Colpitts, T., and O'quinn, B., 2001, "Thin-film thermoelectric devices with high room-temperature figures of merit," nature, 413(6856), pp. 597-602.
[12] Poudel, B., Hao, Q., Ma, Y., Lan, Y., Minnich, A., Yu, B., Yan, X., Wang, D., Muto, A., and Vashaee, D., 2008, "High-thermoelectric performance of nanostructured bismuth antimony telluride bulk alloys," science, 320(5876), pp. 634-638.
[13] Xie, W., Tang, X., Yan, Y., Zhang, Q., and Tritt, T. M., 2009, "Unique nanostructures and enhanced thermoelectric performance of melt-spun BiSbTe alloys," Applied Physics Letters, 94(10).
[14] Xiao, F., Hangarter, C., Yoo, B., Rheem, Y., Lee, K.-H., and Myung, N. V., 2008, "Recent progress in electrodeposition of thermoelectric thin films and nanostructures," Electrochimica Acta, 53(28), pp. 8103-8117.
[15] Sun, Y., Qiu, L., Tang, L., Geng, H., Wang, H., Zhang, F., Huang, D., Xu, W., Yue, P., and Guan, Y. s., 2016, "Flexible n-type high-performance thermoelectric thin films of poly (nickel-ethylenetetrathiolate) prepared by an electrochemical method," Advanced materials, 28(17), pp. 3351-3358.
[16] Kanatzidis, M. G., 2010, "Nanostructured thermoelectrics: the new paradigm?," Chemistry of materials, 22(3), pp. 648-659.
[17] Snyder, G. J., and Toberer, E. S., 2008, "Complex thermoelectric materials," Nature materials, 7(2), pp. 105-114.
[18] Kim, F., Kwon, B., Eom, Y., Lee, J. E., Park, S., Jo, S., Park, S. H., Kim, B.-S., Im, H. J., and Lee, M. H., 2018, "3D printing of shape-conformable thermoelectric materials using all-inorganic Bi2Te3-based inks," Nature Energy, 3(4), pp. 301-309.

[19] Ashcroft, N. W., Mermin, N. D., and Rodriguez, S., 1978, "Solid state physics," American Journal of Physics, 46(1), pp. 116-117.
[20] Franz, R., and Wiedemann, G., 1853, "Ueber die wärme-leitungsfähigkeit der metalle," Annalen der Physik, 165(8), pp. 497-531.
[21] Peierls, R., 1929, "Zur kinetischen theorie der wärmeleitung in kristallen," Annalen der Physik, 395(8), pp. 1055-1101.
[22] Boltzmann, L., 1872, Weitere studien über das wärmegleichgewicht unter gasmolekülen, Aus der kk Hot-und Staatsdruckerei.
[23] Ibáñez, M., Hasler, R., Genç, A., Liu, Y., Kuster, B., Schuster, M., Dobrozhan, O., Cadavid, D., Arbiol, J., and Cabot, A., 2019, "Ligand-mediated band engineering in bottom-up assembled SnTe nanocomposites for thermoelectric energy conversion," Journal of the American Chemical Society, 141(20), pp. 8025-8029.
[24] He, M., Zhao, Y., Wang, B., Xi, Q., Zhou, J., and Liang, Z., 2015, "3D printing fabrication of amorphous thermoelectric materials with ultralow thermal conductivity," Small, 11(44), pp. 5889-5894.
[25] Cahill, D. G., and Pohl, R. O., 1987, "Thermal conductivity of amorphous solids above the plateau," Physical review B, 35(8), p. 4067.
[26] Yang, G., Niu, R., Sang, L., Liao, X., Mitchell, D. R., Ye, N., Pei, J., Li, J. F., and Wang, X., 2020, "Ultra-high thermoelectric performance in bulk BiSbTe/amorphous boron composites with nano-defect architectures," Advanced Energy Materials, 10(41), p. 2000757.
[27] Cahill, D. G., 1990, "Thermal conductivity measurement from 30 to 750 K: the 3ω method," Review of scientific instruments, 61(2), pp. 802-808.
[28] Pauw, L. J. V. d., 1958, "A method of measuring specific resistivity and Hall effect of discs of arbitrary shape," Philips Res. Rep, 13(1), pp. 1-9.
[29] Riko, A., "Seebeck Coefficient / Electric Resistance Measurement System ZEM-3 series," https://advance-riko.com/en/products/zem-3/.
[30] Chen, G., 2005, Nanoscale energy transport and conversion: a parallel treatment of electrons, molecules, phonons, and photons, Oxford university press.
[31] Simon, R., 1962, "Thermoelectric Figure of Merit of Two-Band Semiconductors," Journal of Applied Physics, 33(5), pp. 1830-1841.
[32] Pei, Y., Shi, X., LaLonde, A., Wang, H., Chen, L., and Snyder, G. J., 2011, "Convergence of electronic bands for high performance bulk thermoelectrics," Nature, 473(7345), pp. 66-69.
[33] Heremans, J. P., Jovovic, V., Toberer, E. S., Saramat, A., Kurosaki, K., Charoenphakdee, A., Yamanaka, S., and Snyder, G. J., 2008, "Enhancement of thermoelectric efficiency in PbTe by distortion of the electronic density of states," Science, 321(5888), pp. 554-557.
[34] Mahan, G., and Sofo, J., 1996, "The best thermoelectric," Proceedings of the National Academy of Sciences, 93(15), pp. 7436-7439.
[35] Minnich, A., Dresselhaus, M. S., Ren, Z., and Chen, G., 2009, "Bulk nanostructured thermoelectric materials: current research and future prospects," Energy & Environmental Science, 2(5), pp. 466-479.
[36] Baudry, M., Savelli, G., and Roux, G., 2023, "3D printing of bulk thermoelectric materials: laser powder bed fusion of N-type silicon germanium," Materials Science and Engineering: B, 298, p. 116897.
[37] Wang, Z., Cui, W., Yuan, H., Kang, X., Zheng, Z., Qiu, W., Hu, Q., Tang, J., and Cui, X., 2023, "Direct ink writing of Bi2Te3-based thermoelectric materials induced by rheological design," Materials Today Energy, 31, p. 101206.

[38] Zhou, X., Yan, Y., Lu, X., Zhu, H., Han, X., Chen, G., and Ren, Z., 2018, "Routes for high-performance thermoelectric materials," Materials Today, 21(9), pp. 974-988.
[39] Hossain, M. S., Li, T., Yu, Y., Yong, J., Bahk, J.-H., and Skafidas, E., 2020, "Recent advances in printable thermoelectric devices: materials, printing techniques, and applications," RSC advances, 10(14), pp. 8421-8434.
[40] Biswas, K., He, J., Blum, I. D., Wu, C.-I., Hogan, T. P., Seidman, D. N., Dravid, V. P., and Kanatzidis, M. G., 2012, "High-performance bulk thermoelectrics with all-scale hierarchical architectures," Nature, 489(7416), pp. 414-418.
[41] El-Desouky, A., Carter, M., Mahmoudi, M., Elwany, A., and LeBlanc, S., 2017, "Influences of energy density on microstructure and consolidation of selective laser melted bismuth telluride thermoelectric powder," Journal of Manufacturing Processes, 25, pp. 411-417.
[42] Kim, F., Yang, S. E., Ju, H., Choo, S., Lee, J., Kim, G., Jung, S.-h., Kim, S., Cha, C., and Kim, K. T., 2021, "Direct ink writing of three-dimensional thermoelectric microarchitectures," Nature Electronics, 4(8), pp. 579-587.
[43] Kruth, J. P., Mercelis, P., Van Vaerenbergh, J., Froyen, L., and Rombouts, M., 2005, "Binding mechanisms in selective laser sintering and selective laser melting," Rapid prototyping journal, 11(1), pp. 26-36.
[44] Liu, Z., He, B., Lyu, T., and Zou, Y., 2021, "A review on additive manufacturing of titanium alloys for aerospace applications: directed energy deposition and beyond Ti-6Al-4V," Jom, 73, pp. 1804-1818.
[45] Ahn, D.-G., 2021, "Directed energy deposition (DED) process: state of the art," International Journal of Precision Engineering and Manufacturing-Green Technology, 8(2), pp. 703-742.
[46] Aprilia, A., Wu, N., and Zhou, W., 2022, "Repair and restoration of engineering components by laser directed energy deposition," Materials Today: Proceedings, 70, pp. 206-211.
[47] Svetlizky, D., Das, M., Zheng, B., Vyatskikh, A. L., Bose, S., Bandyopadhyay, A., Schoenung, J. M., Lavernia, E. J., and Eliaz, N., 2021, "Directed energy deposition (DED) additive manufacturing: Physical characteristics, defects, challenges and applications," Materials Today, 49, pp. 271-295.
[48] Administration., U. S. E. I., 2020, "Electric Power Monthly."
[49] Administration, U. S. E. I., 2013, "Form Gc-859, Nuclear Fuel Data Survey."
[50] Commission, U. S. N. R., 2016, "Spent Fuel Pool."
[51] Wang, D., Gauld, I. C., Yoder, G. L., Ott, L. J., Flanagan, G. F., Francis, M. W., Popov, E. L., Carbajo, J. J., Jain, P. K., and Wagner, J. C., 2012, "Study of Fukushima Daiichi nuclear power station unit 4 spent-fuel pool," Nuclear technology, 180(2), pp. 205-215.
[52] Chopra, O., 2014, "Managing Aging Effects on Dry Cask Storage Systems for Extended Long-term Storage and Transportation of Used Fuel, Rev. 2," ANL-13/15.
[53] Champiri, M. D., Mohammadipour, A., Mousavi, R., Willam, K. J., and Gencturk, B., 2017, "Added mass effect for tip-over analysis of dry cask composite structures at two different scales," Annals of Nuclear Energy, 110, pp. 126-139.
[54] Tan, C., Lyons, D. J., Pan, K., Leung, K. Y., Chuirazzi, W. C., Canova, M., Co, A. C., and Cao, L. R., 2016, "Radiation effects on the electrode and electrolyte of a lithium-ion battery," Journal of Power Sources, 318, pp. 242-250.
[55] Zabunoðlu, O., and Yavuz, U., 2006, "Design of a dry cask storage system for spent LWR fuels: radiation protection, subcriticality, and heat removal aspects," Kerntechnik, 71(4), pp. 214-221.

[56] Heibel, M. D., 2022, "Method and apparatus for enhancing the electrical power output of a nuclear reactor power generation system," Google Patents.
[57] Van Herwaarden, A., and Sarro, P., 1986, "Thermal sensors based on the Seebeck effect," Sensors and Actuators, 10(3-4), pp. 321-346.
[58] Rowe, D., 1991, "Applications of nuclear-powered thermoelectric generators in space," Applied Energy, 40(4), pp. 241-271.
[59] Dillner, U., Kessler, E., and Meyer, H.-G., 2013, "Figures of merit of thermoelectric and bolometric thermal radiation sensors," Journal of Sensors and Sensor Systems, 2(1), pp. 85-94.
[60] Nozariasbmarz, A., Poudel, B., Li, W., Kang, H. B., Zhu, H., and Priya, S., 2020, "Bismuth telluride thermoelectrics with 8% module efficiency for waste heat recovery application," IScience, 23(7).
[61] Ye, C., Zheng, M., Wang, M., Zhang, R., and Xiong, Z., 2013, "The design and simulation of a new spent fuel pool passive cooling system," Annals of Nuclear Energy, 58, pp. 124-131.
[62] Tseng, V. F.-G., Bedair, S. S., and Lazarus, N., 2018, "Acoustic power transfer and communication with a wireless sensor embedded within metal," IEEE Sensors Journal, 18(13), pp. 5550-5558.
[63] Carstens, T. A., Corradini, M. L., Blanchard, J. P., Liu, C.-H., Li, M., Behdad, N., and Ma, Z., 2012, "Thermoelectric powered wireless sensors for dry-cask storage," IEEE Transactions on Nuclear Science, 60(2), pp. 1072-1079.
[64] Chakraborty, S., Saulnier, G. J., Wilt, K. W., Curt, E., Scarton, H. A., and Litman, R. B., 2015, "Low-power, low-rate ultrasonic communications system transmitting axially along a cylindrical pipe using transverse waves," IEEE transactions on ultrasonics, ferroelectrics, and frequency control, 62(10), pp. 1788-1796.
[65] Graham, D. J., Neasham, J. A., and Sharif, B. S., 2011, "Investigation of methods for data communication and power delivery through metals," IEEE Transactions on industrial electronics, 58(10), pp. 4972-4980.
[66] Lawry, T. J., Wilt, K. R., Ashdown, J. D., Scarton, H. A., and Saulnier, G. J., 2012, "A high-performance ultrasonic system for the simultaneous transmission of data and power through solid metal barriers," IEEE transactions on ultrasonics, ferroelectrics, and frequency control, 60(1), pp. 194-203.
[67] Murphy, T. L., 2005, "Ultrasonic digital communication system for a steel wall multipath channel: Methods and results," Knolls Atomic Power Lab.(KAPL), Niskayuna, NY (United States).
[68] Saulnier, G., Scarton, H., Shoudy, D., Das, P., and Gavens, A., 2010, "Ultrasonic Through-Wall Communication (UTWC) System," Google Patents.
[69] Saulnier, G. J., Scarton, H. A., Gavens, A. J., Shoudy, D., Murphy, T., Wetzel, M., Bard, S., Roa-Prada, S., and Das, P., "P1g-4 through-wall communication of low-rate digital data using ultrasound," Proc. 2006 IEEE Ultrasonics Symposium, IEEE, pp. 1385-1389.
[70] Bagatin, M., and Gerardin, S., 2016, "Ionizing Radiation Effectsin Electronics."
[71] Wu, Y., Klein, J., Zhou, H., Zhang, H., and Zuo, L., 2019, "Energy harvesting for wireless communications in nuclear environment," Annals of Nuclear Energy, 126, pp. 376-388.
[72] Li, J., and Liu, Y. Y., 2016, "Thermal modeling of a vertical dry storage cask for used nuclear fuel," Nuclear Engineering and Design, 301, pp. 74-88.
[73] Wu, Y., Klein, J., Zhou, H., and Zuo, L., 2018, "Thermal and fluid analysis of dry cask storage containers over multiple years of service," Annals of Nuclear Energy, 112, pp. 132-142.
[74] Weihermiller, W., and Allison, G., 1979, "LWR nuclear fuel bundle data for use in fuel bundle handling," Battelle Pacific Northwest Labs., Richland, WA (United States).

[75] Wu, Y., Klein, J., Zhou, H., and Zuo, L., "Energy Harvesting for Nuclear Waste Sensing and Monitoring," Proc. International Design Engineering Technical Conferences and Computers and Information in Engineering Conference, American Society of Mechanical Engineers, p. V01AT02A008.
[76] Giménez, M., and Lopasso, E., 2018, "Tungsten carbide compact primary shielding for small medium reactor," Annals of Nuclear Energy, 116, pp. 210-223.
[77] Briesmeister, J. F., 2000, "MCNPTM-A general Monte Carlo N-particle transport code," Version 4C, LA-13709-M, Los Alamos National Laboratory, 2.
[78] Klein, J. A., 2017, "Energy Harvesting Opportunities Throughout the Nuclear Power Cycle for Self-Powered Wireless Sensor Nodes," Virginia Tech.
[79] Wu, Y., 2019, "Thermoelectric Energy Harvesting for Sensor Powering."
[80] Maurath, D., Ortmanns, M., and Manoli, Y., "High efficiency, low-voltage and self-adjusting charge pump with enhanced impedance matching," Proc. 2008 51st Midwest Symposium on Circuits and Systems, IEEE, pp. 189-192.
[81] Citterio, M., Rescia, S., and Radeka, V., 1995, "Radiation effects at cryogenic temperatures in Si-JFET, GaAs MESFET, and MOSFET devices," IEEE Transactions on Nuclear Science, 42(6), pp. 2266-2270.
[82] Reed, F. K., Ericson, M. N., Ezell, N. D. B., Kisner, R. A., Zuo, L., Zhang, H., and Flammang, R., 2022, "A 100-Mrad (Si) JFET-based sensing and communications system for extreme nuclear instrumentation environments," Nuclear Technology, 208(10), pp. 1497-1510.
[83] Waly, E.-S. A., and Bourham, M. A., 2015, "Comparative study of different concrete composition as gamma-ray shielding materials," Annals of Nuclear Energy, 85, pp. 306-310.
[84] Chen, J., Klein, J., Wu, Y., Xing, S., Flammang, R., Heibel, M., and Zuo, L., 2016, "A thermoelectric energy harvesting system for powering wireless sensors in nuclear power plants," IEEE Transactions on nuclear science, 63(5), pp. 2738-2746.
[85] Rowe, D. M., 2005, Thermoelectrics handbook: macro to nano, CRC press.
[86] Mingo, N., Hauser, D., Kobayashi, N., Plissonnier, M., and Shakouri, A., 2009, "“Nanoparticle-in-Alloy” approach to efficient thermoelectrics: silicides in SiGe," Nano Lett, 9(2), pp. 711-715.
[87] Mingo, N., Hauser, D., Kobayashi, N. P., Plissonnier, M., and Shakouri, A., 2009, ""Nanoparticle-in-Alloy" Approach to Efficient Thermoelectrics: Silicides in SiGe," Nano Lett, 9(2), pp. 711-715.
[88] Wang, S. Y., Yang, J., Toll, T., Yang, J. H., Zhang, W. Q., and Tang, X. F., 2015, "Conductivity-limiting bipolar thermal conductivity in semiconductors," Sci Rep-Uk, 5.
[89] Poudel, B., Hao, Q., Ma, Y., Lan, Y. C., Minnich, A., Yu, B., Yan, X. A., Wang, D. Z., Muto, A., Vashaee, D., Chen, X. Y., Liu, J. M., Dresselhaus, M. S., Chen, G., and Ren, Z. F., 2008, "High-thermoelectric performance of nanostructured bismuth antimony telluride bulk alloys," Science, 320(5876), pp. 634-638.
[90] Minnich, A. J., Dresselhaus, M. S., Ren, Z. F., and Chen, G., 2009, "Bulk nanostructured thermoelectric materials: current research and future prospects," Energy & Environmental Science, 2(5), pp. 466-479.
[91] Mao, Y., Yan, Y. G., Wu, K. P., Xie, H. Y., Xiu, Z. K., Yang, J. H., Zhang, Q. J., Uher, C., and Tang, X. F., 2017, "Non-equilibrium synthesis and characterization of n-type Bi2Te2.7Se0.3 thermoelectric material prepared by rapid laser melting and solidification," Rsc Advances, 7(35), pp. 21439-21445.

[92] Bremen, S., Meiners, W., and Diatlov, A., 2012, "Selective laser melting," Laser Technik Journal, 9(2), pp. 33-38.
[93] Xiao, B., and Zhang, Y. W., 2007, "Analysis of partial melting in metal powder bed with constant heat flux," Heat Transfer Eng, 28(5), pp. 472-483.
[94] Zeng, K., Pal, D., and Stucker, B., "A review of thermal analysis methods in Laser Sintering and Selective Laser Melting," Proc. Proceedings of Solid Freeform Fabrication Symposium Austin, TX, pp. 796-814.
[95] Roberts, I. A., Wang, C. J., Esterlein, R., Stanford, M., and Mynors, D. J., 2009, "A three-dimensional finite element analysis of the temperature field during laser melting of metal powders in additive layer manufacturing," Int J Mach Tool Manu, 49(12-13), pp. 916-923.
[96] Xiao, B., and Zhang, Y. W., 2007, "Marangoni and buoyancy effects on direct metal laser sintering with a moving laser beam," Numer Heat Tr a-Appl, 51(8), pp. 715-733.
[97] Li, J. F., Li, L., and Stott, F. H., 2004, "A three-dimensional numerical model for a convection-diffusion phase change process during laser melting of ceramic materials," Int J Heat Mass Tran, 47(25), pp. 5523-5539.
[98] Korner, C., Attar, E., and Heinl, P., 2011, "Mesoscopic simulation of selective beam melting processes," J Mater Process Tech, 211(6), pp. 978-987.
[99] Khairallah, S. A., and Anderson, A., 2014, "Mesoscopic simulation model of selective laser melting of stainless steel powder," J Mater Process Tech, 214(11), pp. 2627-2636.
[100] Voller, V. R., Brent, A. D., and Prakash, C., 1989, "The Modeling of Heat, Mass and Solute Transport in Solidification Systems," Int J Heat Mass Tran, 32(9), pp. 1719-1731.
[101] Luo, C., Qiu, J., Yan, Y., Yang, J., Uher, C., and Tang, X., 2018, "Finite element analysis of temperature and stress fields during the selective laser melting process of thermoelectric SnTe," J Mater Process Tech, 261, pp. 74-85.
[102] Voller, V. R., Brent, A., and Prakash, C., 1989, "The modelling of heat, mass and solute transport in solidification systems," Int J Heat Mass Tran, 32(9), pp. 1719-1731.
[103] Xiao, B., and Zhang, Y., 2007, "Marangoni and buoyancy effects on direct metal laser sintering with a moving laser beam," Numerical Heat Transfer, Part A: Applications, 51(8), pp. 715-733.
[104] Dutta, P., Joshi, Y., and Janaswamy, R., 1995, "Thermal Modeling of Gas Tungsten Arc-Welding Process with Nonaxisymmetric Boundary-Conditions," Numer Heat Tr a-Appl, 27(5), pp. 499-518.
[105] Hadley, G. R., 1986, "Thermal-Conductivity of Packed Metal Powders," Int J Heat Mass Tran, 29(6), pp. 909-920.
[106] Patankar, S., 1980, Numerical heat transfer and fluid flow, CRC press.
[107] Van Leer, B., 1974, "Towards the ultimate conservative difference scheme. II. Monotonicity and conservation combined in a second-order scheme," Journal of computational physics, 14(4), pp. 361-370.
[108] Versteeg, H. K., and Malalasekera, W., 2007, An introduction to computational fluid dynamics: the finite volume method, Pearson Education.
[109] Tao, W., 2001, Numerical heat transfer (Second edition), Xi'an Jiaotong University Press.
[110] Akasaka, M., Iida, T., Matsumoto, A., Yamanaka, K., Takanashi, Y., Imai, T., and Hamada, N., 2008, "The thermoelectric properties of bulk crystalline n- and p-type Mg2Si prepared by the vertical Bridgman method," Journal of Applied Physics, 104(1).
[111] Yu, B. H., Chen, D., Tang, Q. B., Wang, C. L., and Shi, D. H., 2010, "Structural, electronic, elastic and thermal properties of Mg2Si," J Phys Chem Solids, 71(5), pp. 758-763.

[112] Glassbrenner, C., and Slack, G. A., 1964, "Thermal conductivity of silicon and germanium from 3 K to the melting point," Physical Review, 134(4A), p. A1058.
[113] Kou, S., and Wang, Y., 1986, "Three-dimensional convection in laser melted pools," Metallurgical transactions A, 17(12), pp. 2265-2270.
[114] Kou, S., and Wang, Y., 1986, "Weld pool convection and its effect," Weld. J, 65(3), pp. 63s-70s.
[115] Frazier, W. E., 2014, "Metal additive manufacturing: a review," Journal of Materials Engineering and performance, 23(6), pp. 1917-1928.
[116] Bajaj, P., Hariharan, A., Kini, A., Kürnsteiner, P., Raabe, D., and Jägle, E. A., 2020, "Steels in additive manufacturing: A review of their microstructure and properties," Materials Science and Engineering: A, 772, p. 138633.
[117] Zhang, C., Chen, F., Huang, Z., Jia, M., Chen, G., Ye, Y., Lin, Y., Liu, W., Chen, B., and Shen, Q., 2019, "Additive manufacturing of functionally graded materials: A review," Materials Science and Engineering: A, 764, p. 138209.
[118] Perigo, E. A., Weidenfeller, B., Kollár, P., and Füzer, J., 2018, "Past, present, and future of soft magnetic composites," Applied Physics Reviews, 5(3), p. 031301.
[119] Xia, Z., Kang, Y., and Wang, Q., 2008, "Developments in the production of grain-oriented electrical steel," Journal of Magnetism and Magnetic Materials, 320(23), pp. 3229-3233.
[120] Association, W. S., 2018, "STEEL STATISTICAL YEARBOOK 2018."
[121] Wrobel, R., and Mecrow, B., "Additive manufacturing in construction of electrical machines–a review," Proc. 2019 IEEE Workshop on Electrical Machines Design, Control and Diagnosis (WEMDCD), IEEE, pp. 15-22.
[122] Goll, D., Schuller, D., Martinek, G., Kunert, T., Schurr, J., Sinz, C., Schubert, T., Bernthaler, T., Riegel, H., and Schneider, G., 2019, "Additive manufacturing of soft magnetic materials and components," Additive Manufacturing, 27, pp. 428-439.
[123] Babuska, T. F., Wilson, M. A., Johnson, K. L., Whetten, S. R., Curry, J. F., Rodelas, J. M., Atkinson, C., Lu, P., Chandross, M., and Krick, B. A., 2019, "Achieving high strength and ductility in traditionally brittle soft magnetic intermetallics via additive manufacturing," Acta Materialia, 180, pp. 149-157.
[124] Oh, W. J., Lee, W. J., Kim, M. S., Jeon, J. B., and Shim, D. S., 2019, "Repairing additive-manufactured 316L stainless steel using direct energy deposition," Optics & Laser Technology, 117, pp. 6-17.
[125] Kim, M.-s., Oh, W.-j., Baek, G.-y., Jo, Y.-k., Lee, K.-y., Park, S.-h., and Shim, D.-s., 2020, "Ultrasonic nanocrystal surface modification of high-speed tool steel (AISI M4) layered via direct energy deposition," J Mater Process Tech, 277, p. 116420.
[126] Singh, D. D., Arjula, S., and Reddy, A. R., 2021, "Functionally Graded Materials Manufactured by Direct Energy Deposition: A review," Materials Today: Proceedings, 47, pp. 2450-2456.
[127] Garibaldi, M., Ashcroft, I., Lemke, J., Simonelli, M., and Hague, R., 2018, "Effect of annealing on the microstructure and magnetic properties of soft magnetic Fe-Si produced via laser additive manufacturing," Scripta Materialia, 142, pp. 121-125.
[128] Dobryanskiy, V., Rabinskiy, L., and Tushavina, O., 2019, "Experimental finding of fracture toughness characteristics and theoretical modeling of crack propagation processes in carbon fiber samples under conditions of additive production," Periodico Tche Quimica, 16(33), pp. 325-336.

[129] Wu, B., Pan, Z., Ding, D., Cuiuri, D., Li, H., Xu, J., and Norrish, J., 2018, "A review of the wire arc additive manufacturing of metals: properties, defects and quality improvement," Journal of Manufacturing Processes, 35, pp. 127-139.
[130] Chen, Y., Zhang, K., Huang, J., Hosseini, S. R. E., and Li, Z., 2016, "Characterization of heat affected zone liquation cracking in laser additive manufacturing of Inconel 718," Materials & Design, 90, pp. 586-594.
[131] Brennan, M., Keist, J., and Palmer, T., 2021, "Defects in Metal Additive Manufacturing Processes," Journal of Materials Engineering and Performance, 30(7), pp. 4808-4818.
[132] Chen, Y., Peng, X., Kong, L., Dong, G., Remani, A., and Leach, R., 2021, "Defect inspection technologies for additive manufacturing," International Journal of Extreme Manufacturing, 3(2), p. 022002.
[133] Lee, Y., and Zhang, W., "Mesoscopic simulation of heat transfer and fluid flow in laser powder bed additive manufacturing," Proc. 2015 International Solid Freeform Fabrication Symposium, University of Texas at Austin.
[134] Qiu, Y.-D., Wu, J.-M., Chen, A.-N., Chen, P., Yang, Y., Liu, R.-Z., Chen, G., Chen, S., Shi, Y.-S., and Li, C.-H., 2020, "Balling phenomenon and cracks in alumina ceramics prepared by direct selective laser melting assisted with pressure treatment," Ceramics International, 46(9), pp. 13854-13861.
[135] Ma, X., Peyton, A., and Zhao, Y., 2006, "Eddy current measurements of electrical conductivity and magnetic permeability of porous metals," Ndt & E International, 39(7), pp. 562-568.
[136] Thijs, L., Kempen, K., Kruth, J.-P., and Van Humbeeck, J., 2013, "Fine-structured aluminium products with controllable texture by selective laser melting of pre-alloyed AlSi10Mg powder," Acta Materialia, 61(5), pp. 1809-1819.
[137] Allwood, D. A., Xiong, G., Faulkner, C., Atkinson, D., Petit, D., and Cowburn, R., 2005, "Magnetic domain-wall logic," science, 309(5741), pp. 1688-1692.
[138] Huber, C., Sepehri-Amin, H., Goertler, M., Groenefeld, M., Teliban, I., Hono, K., and Suess, D., 2019, "Coercivity enhancement of selective laser sintered NdFeB magnets by grain boundary infiltration," Acta Materialia, 172, pp. 66-71.
[139] Bertoli, U. S., Guss, G., Wu, S., Matthews, M. J., and Schoenung, J. M., 2017, "In-situ characterization of laser-powder interaction and cooling rates through high-speed imaging of powder bed fusion additive manufacturing," Materials & Design, 135, pp. 385-396.
[140] Salman, O., Gammer, C., Chaubey, A., Eckert, J., and Scudino, S., 2019, "Effect of heat treatment on microstructure and mechanical properties of 316L steel synthesized by selective laser melting," Materials Science and Engineering: A, 748, pp. 205-212.
[141] Garibaldi, M., Ashcroft, I., Hillier, N., Harmon, S., and Hague, R., 2018, "Relationship between laser energy input, microstructures and magnetic properties of selective laser melted Fe-6.9% wt Si soft magnets," Materials Characterization, 143, pp. 144-151.
[142] Taguchi, G., 1995, "Quality engineering (Taguchi methods) for the development of electronic circuit technology," IEEE Transactions on Reliability, 44(2), pp. 225-229.
[143] Tsai, T.-N., and Liukkonen, M., 2016, "Robust parameter design for the micro-BGA stencil printing process using a fuzzy logic-based Taguchi method," applied soft computing, 48, pp. 124-136.
[144] Dunford, R., Su, Q., and Tamang, E., 2014, "The pareto principle."
[145] Fujishima, M., Oda, Y., Ashida, R., Takezawa, K., and Kondo, M., 2017, "Study on factors for pores and cladding shape in the deposition processes of Inconel 625 by the directed energy

deposition (DED) method," CIRP Journal of Manufacturing Science and Technology, 19, pp. 200-204.
[146] Nam, S., Cho, H., Kim, C., and Kim, Y.-M., 2018, "Effect of process parameters on deposition properties of functionally graded STS 316/Fe manufactured by laser direct metal deposition," Metals, 8(8), p. 607.
[147] Hwang, S. S., Lim, Y. S., Kim, S. W., Kim, D. J., and Kim, H. P., 2013, "Role of grain boundary carbides in cracking behavior of Ni base alloys," Nuclear Engineering and Technology, 45(1), pp. 73-80.
[148] Pham, T. Q., Do, T. T., Kwon, P., and Foster, S. N., "Additive manufacturing of high performance ferromagnetic materials," Proc. 2018 IEEE Energy Conversion Congress and Exposition (ECCE), IEEE, pp. 4303-4308.
[149] Tiismus, H., Kallaste, A., Belahcen, A., Tarraste, M., Vaimann, T., Rassõlkin, A., Asad, B., and Shams Ghahfarokhi, P., 2021, "AC Magnetic Loss Reduction of SLM Processed Fe-Si for Additive Manufacturing of Electrical Machines," Energies, 14(5), p. 1241.
[150] Ouyang, G., Chen, X., Liang, Y., Macziewski, C., and Cui, J., 2019, "Review of Fe-6.5 wt% Si high silicon steel—A promising soft magnetic material for sub-kHz application," Journal of Magnetism and Magnetic Materials, 481, pp. 234-250.